Title

Innovative Methodology and Applications of Diffusion-tensor and Hyperpolarized Carbon-13 Magnetic Resonance Imaging in Pediatric Brain Development

Author

Chen, Yiran

Publication Date

2018

Peer reviewed|Thesis/dissertation

Innovative Methodology and Applications of Diffusion-tensor and Hyperpolarized Carbon-13 Magnetic Resonance Imaging in Pediatric Brain Development

by

Yiran Chen

DISSERTATION

Submitted in partial satisfaction of the requirements for degree of

DOCTOR OF PHILOSOPHY

in

Bioengineering

in the

GRADUATE DIVISION

of the

UNIVERSITY OF CALIFORNIA, SAN FRANCISCO
AND
UNIVERSITY OF CALIFORNIA, BERKELEY

Approved:

DocuSigned by:
FBF5DD86B35B422...

Duan Xu

Chair

DocuSigned by:
DocuSigned by:
61CFDFCC15EF48F...

Peder Larson

Donna Ferriero

Committee Members

Acknowledgements

This dissertation is impossible without many people. First, I was given the opportunity to work at Dr. Duan Xu's lab as a Junior Specialist after college because I expressed interest in magnetic resonance imaging (MRI). Two years later, I became the first graduate student in the same lab. Throughout these years, Dr. Xu has always been an optimistic and enthusiastic personal mentor, team leader and pioneer in pediatric MRI. He has brought about many creative ideas, and we together put them into actions and results. This dissertation will be a snapshot demonstration of his insightfulness in the area of his research expertise. I am also thankful to him for creating a delightful academic environment of our lab that everyone enjoys.

Dr. Peder Larson is the only person in both of my dissertation committee and qualifying exam committee. He has provided many technical advices in both circumstances. I have sit through his Principles of MRI class a few years ago and became a teaching assistant last year, which I have learnt and re-learnt many things through these experiences.

Dr. Donna Ferriero is not only my dissertation committee member, but also the main collaborator for most of my projects. With guidance of her senior expertise in pediatric and neurological research, I was able to conduct my research smoothly with a clear vision and many members from her lab.

Dr. Olga Tymofiyeva is one of the people who I have known for the longest time at University of California San Francisco (UCSF). Besides being a colleague and a friend, she is also the first

unofficial mentor of my research at UCSF. She taught me the fundamentals of MRI from theory to applications, and supported me with a great extent for my first peer-reviewed paper publication, which I struggled for over a year and now part of this dissertation. Her kindness and patience has always been and will continue accompanying me beyond academia.

There are many collaborators who I have worked with closely through my dissertation research. Dr. Alkisti Mikrogeorgiou, Dr. Byongsop Lee (now a doctor at Asan Medical Center, South Korea) and Ann Sheldon from Ferriero's lab in Department of Pediatrics, and Dr. Ilwoo Park (now an Assistant Professor at Chonnam National University Medical School, South Korea) and Dr. Xin Mu from Department of Radiology and Biomedical Imaging have all helped me in various ways of animal surgery and handling during my projects. Especially with Alkisti and Byongsop, we have worked together through many days and nights with uncountable failures and in the end, acceptable results.

There are three people from Department of Radiology and Biomedical Imaging I have to specifically thank to. Dr. Subramaniam Sukumar (now retired) provided supervision, training and support on conducting animal MRI experiments since the very first week of me being at UCSF. Dr. Robert Bok has helped a lot during my experiments, and trained many of my collaborators and me on animal handling. He is also a testimony of showing care and patience for animals while doing research on them. Mark Van Criekinge always keeps the hardware of scanners and polarizers in a good shape and fixes them when someone broke them or they broke themselves.

Dr. Hosung Kim, a former postdoctoral scholar in Dr. Xu's lab and now an Assistant Professor at University of Southern California, taught me almost everything I know in image processing, and continued answering my questions for years after he left the lab. Trevor Flynn always kindly provided me the clinical notes of our pediatric studies whenever I asked from him last minute before any deadline. Dr. Christopher Hess is a close collaborator of our lab and my qualifying exam committee member, and he has provided guidance in many aspects.

I thank Drs. Myriam Chaumeil, Renuka Sriram, Marina Radoul, Chloe Najac, Caroline Guglielmetti, Jessie Lee, Georgios Batsios and Brice Tiret, who shared the scanner and polarizers with me for many years, for being flexible in their scan times so I could finish my experiment with extra time or conduct my experiment at a preferred time. Some of them have also helped me in various ways in experimentation, data analysis and troubleshooting. I would also like to thank Romelyn Delos Santos and Dr. Dave Korenchan for making chemicals for my experiments, and Dr. Shujuan Fan and Hecong Qin for making dissolution solution for me at the perfect timing whenever I ran out of it.

I appreciate all the help from Drs. Cornelius Von Morze, Jeremy Gorden, Adam, Hsin-Yu Chen, Eugene Milshteyn, Peter Shin, Zihan Zhu on ^{13}C experiments and collaborations. I also thank Yicheng Chen for much help on processing pediatric clinical data and Xucheng Zhu for co-TA'ed Peder Larson's class on Principles of MRI. I feel grateful for being a friend of some of the above-mentioned names, as well as Shuyu Tang, Justin Yuan, Elizabeth Phillips, Dr. Peng Cao and many alumni and current students from UCSF/UC Berkeley Joint Program in Bioengineering for their continuous support over these years. Many thanks to administrators

Jenney Che, Cathy Devine, Kim Semien and Ana Maria DeLuca for making everything run smoothly.

Last but not least, I would like to take this opportunity to thank Dr. Sarah Nelson for being my graduate advisor, qualifying exam committee chair and a collaborator who I have worked with almost everyone from her lab, and Drs. Dan Vigneron, John Kurhanewicz and Sabrina Ronen for being senior leaders of the Surbeck Lab and oversaw many of our experiments' planning and conduct. None of these talents and projects will exist without them.

Thank you everyone!

Yiran Chen

December 2018

In remembrance of my cat, Lucipurr, who accompanied me through the darkest time in my life and passed away a month before this dissertation was published. He will always have a place in my heart along with his sister, Cali.

Contributions

Chapter 2 is adapted from the following publication:

Effects of Rejecting Diffusion Directions on Tensor-derived Parameters.

Yiran Chen, Olga Tymofiyeva, Christopher P Hess, and Duan Xu.

NeuroImage 109 (2015): 160-70.

https://www.ncbi.nlm.nih.gov/pubmed/25585018

Chapter 3 is adapted from the following publication:

Pyruvate to Lactate Metabolic Changes During Neurodevelopment Measured Dynamically Using Hyperpolarized ^{13}C Imaging in Juvenile Murine Brain.

Yiran Chen, Hosung Kim, Robert Bok, Subramaniam Sukumar, Xin Mu, R Ann Sheldon, A James Barkovich, Donna M Ferriero, and Duan Xu.

Developmental Neuroscience 38(1) (2016): 34-40.

https://www.ncbi.nlm.nih.gov/pmc/articles/PMC4732911/

Abstract

Innovative Methodology and Applications of Diffusion-tensor and Hyperpolarized ^{13}C Magnetic Resonance Imaging in Pediatric Brain Development

Yiran Chen

Pediatric magnetic resonance imaging (MRI) emerged as an independent research area from adult MRI, due to distinct brain structure and development trajectory, and different responses to brain injuries or diseases in pediatric subjects. This dissertation discussed a few unexplored but important areas in pediatric brain MRI, including diffusion tensor imaging (DTI) and hyperpolarized ^{13}C spectroscopic imaging.

DTI is adversely affected by subject motion, which is a common problem among unsedated pediatric subjects. It is necessary to discard the corrupted images before diffusion parameter estimation. However, the consequences of rejecting those images were not well understood. We investigated the effects of excluding one or more volumes of diffusion weighted images by analyzing the changes in diffusion parameters. Based on the full set of diffusion images, we generated incomplete sets in three different ways: random, uniform and clustered rejections. Different rejection methods resulted in very different variations in DTI parameters, and sometimes the resulting accuracy depended on the relative orientation of the underlying fibers with respect to the excluded directions. In practice, if diffusion data is excluded, it is important to

note the number and location of directions rejected, in order to make a more precise analysis of the results.

Structural changes during early brain development have been studied using conventional MRI methods, but metabolic changes remain unrevealed. Hyperpolarized ^{13}C spectroscopic imaging has recently been used to dynamically image metabolism *in vivo*. This technique provides the capability to investigate metabolic changes in mouse brain development over multiple time points. We used hyperpolarized ^{13}C-1 labeled pyruvate to analyze its conversion into lactate during early brain development in normal and hypoxic-ischemic (HI) injured brains. The produced lactate level decreased linearly with increasing age in normal brains, but no pattern was observed in HI brains. This technique was also able to detect HI injury at a very early stage within a very short amount of time, which was hardly discovered otherwise. It can be a potential marker for HI diagnosis and progression tracking.

TABLE OF CONTENTS

LIST OF FIGURES

LIST OF TABLES

吾生也有涯，而知也无涯。以有涯随无涯，殆已；以而为之者，殆而已矣。

– 庄子 （公元前 369 年 – 前 286 年）

Human life is limited, but knowledge is limitless. To drive the limited in pursuit of the limitless is fatal; and to presume that one really knows is fatal indeed!

– Chuang Tzu (369 BC – 286 BC)

– Translated by Yutang Lin

Chapter 1 : Background

1.1 Background of MRI

The human body can be considered to be made of three main tissue types: fluids – cerebrospinal fluid (CSF), synovial fluid, edema; water-based tissues – muscle, brain, cartilage, kidney; and fat-based tissues – fat, bone marrow [1]. Each of these is shown as different contrast in conventional MR proton imaging, which depends on the concentration and physical properties of hydrogen atoms. The most commonly used for imaging are: spin-lattice relaxation time (T1) and spin-spin relaxation time (T2) that will be depicted as different image contrast by varying acquisition parameters such as repetition time (TR), echo time (TE) and flip angle (α) in a gradient echo (GE) or spin echo (SE) sequence.

A neonatal brain displays a reversed image contrast as compared to an adult brain (Figure 1.1), due to different water content in the grey and white matters during brain development.

Besides standard T1- and T2-weighted images, there are many other types of images contrast by different designs of the pulse sequence such as changing excitation pulses, gradients, TR and TE. Among these special types of image contrasts, diffusion-weighted imaging (DWI) has been the most widely practiced image contrast in both adult and pediatric MR in clinical and research settings.

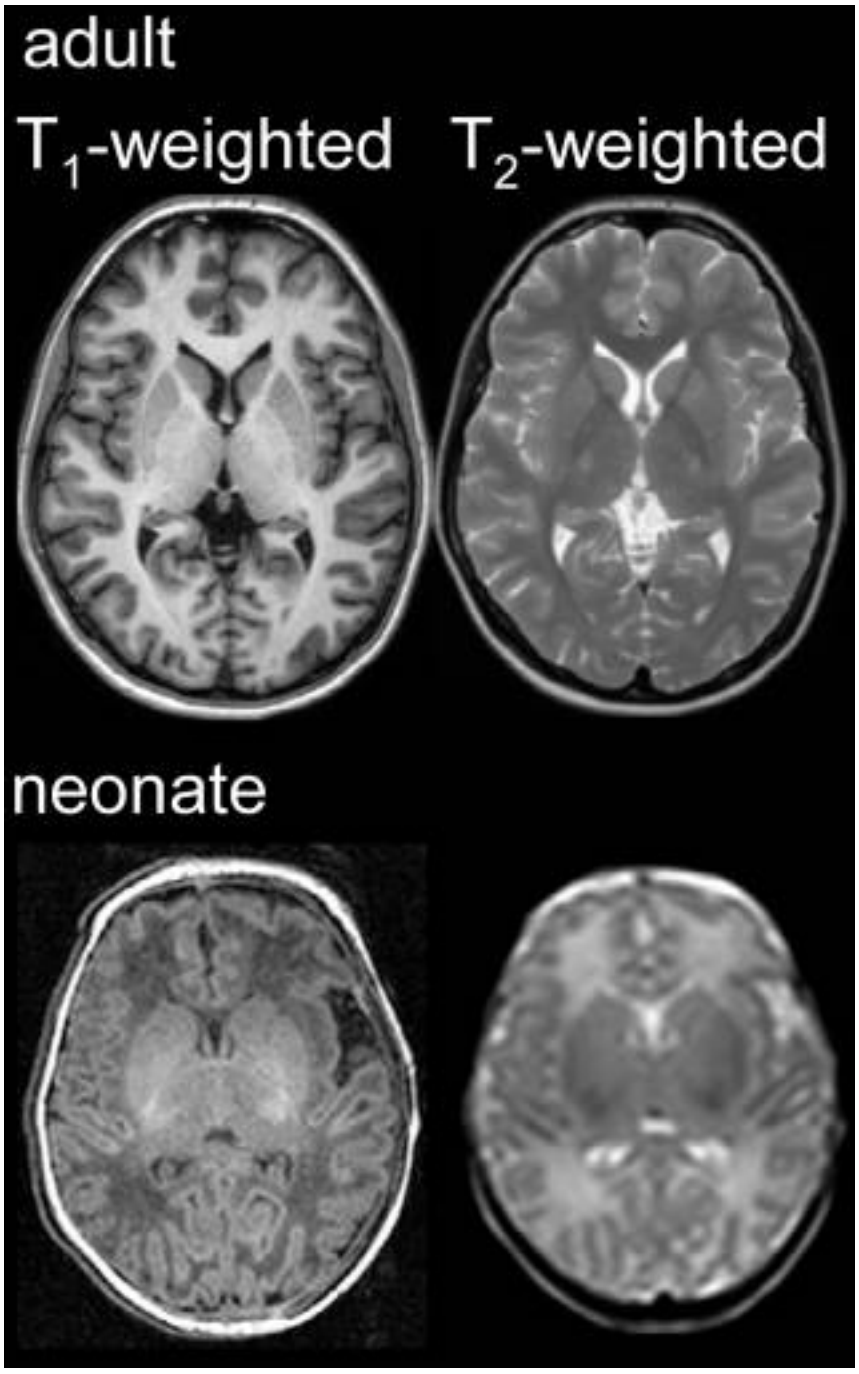

Figure 1.1: Comparison of a neonatal brain and an adult brain.

Note that the image contrast in both T1- and T2-weighted images is altered between the two groups [2].

1.2 Diffusion-weighted imaging

Diffusion encoding was first introduced by Stejskal and Tanner [3] as applying a pair of diffusion gradients along the same axis both before and after the 180° refocusing pulse in a T2-weighted spin-echo sequence (Figure 1.2). Different image contrast is created by free water diffusion along the same axis of the applied diffusion gradient, thus differentiating tissue types with different water content and properties.

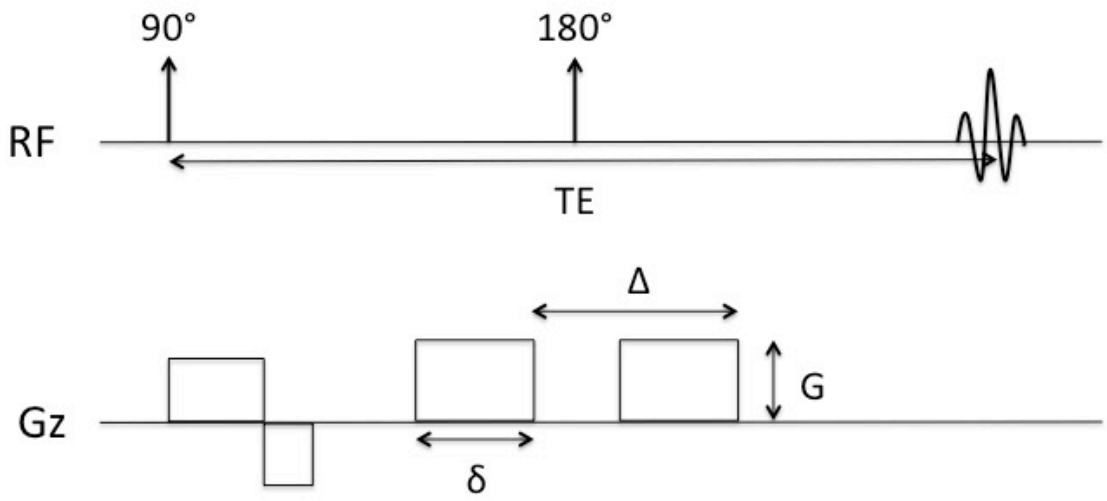

Figure 1.2: A conventional spin-echo diffusion sequence.

The diffusion-weighted signal can be described as:

$$S = S_0 e^{-ADC \cdot b}$$

where S_0 is the signal intensity without diffusion gradients, ADC is apparent diffusion coefficient, and b, or b-value, is described as:

$$b = \gamma^2 \int_0^{\Delta} \left[\int_0^{\delta} \vec{G}(t')dt' \right]^2 dt = \gamma^2 G^2 \delta^2 (\Delta - \frac{\delta}{3})$$

where γ is the gyromagnetic ratio, G is the amplitude of the diffusion gradient, δ is the duration of the diffusion gradient, and Δ is the temporal spacing between the diffusion gradients.

Moseley et al. first applied DWI on cerebral ischemic cats and discovered that DWI was able to detect brain injury at a much earlier stage (45 min after onset) than T2-weighted images (2-3 hour postocclusion). This was regarded a milestone of the applications of DWI and further advanced the implementation of DWI as a standard imaging protocol for clinical diagnosis of neurological injuries or diseases.

A few mathematical models have been developed from DWI for injury detection and microstructure analysis. The most commonly used is diffusion tensor imaging (DTI). As we know that DWI contrast is generated by free water diffusion along the same axis of the applied diffusion gradient, while structures such as membrane and myelin hinder the free water diffusion and force directionality of water movement, then different orientations of the structure with respect to the diffusion gradient will create different image contrasts. Thus, by applying diffusion gradients along distinct directions, we are able to obtain difference image contrasts of the same structure. Moreover, the more anisotropic the structure is, the more prominent the difference between each DW image will be. DTI is build upon this concept. It requires at least 6 non-colinear diffusion-encoding gradients, usually evenly distributed on an electrostatic sphere. The diffusion tensor, D, which is a representation of the scale and orientation of the diffusion ellipsoid associated with the underlying microstructure of a voxel, can be evaluated as:

$$\frac{S}{S_0} = e^{-\sum_{i=x,y,z}\sum_{j=x,y,z} b_{i,j}D_{i,j}}$$

where $b_{i,j} = \gamma^2 G_i G_j \left[\delta^2(\Delta - \frac{\delta}{3})\right]$.

This orientation of the structure is represented by the diffusion tensor D, and a number of tensor parameters can be estimated from D. By diagonalizing D,

$$R \cdot D \cdot R^T = \begin{bmatrix} \lambda_1 & 0 & 0 \\ 0 & \lambda_2 & 0 \\ 0 & 0 & \lambda_3 \end{bmatrix}$$

we get matrix R, which has each of its columns as an eigenvector (V_1, V_2, V_3) of the system, and its corresponding eigenvalues, λ_1 , λ_2 and λ_3 , in descending order of magnitude. The eigenvectors represent the orientation of the diffusion ellipsoid in 3 orthogonal axes, and the eigenvalues represents the lengths of each of the eigenvectors, respectively. The eigenvector associated with λ_1 is the primary eigenvector (V_1), which indicates the greatest water diffusion direction.

λ_1 is defined as axial diffusivity (AD) - the diffusivity along the direction of V_1, and the mean of λ_2 and λ_3 is radial diffusivity (RD) - the diffusivity on the transverse plane orthogonal to V_1. The mean of the 3 eigenvalues is mean diffusivity (MD). The franctional anisotropy (FA) is a normalized value from the 3 eigenvalues as:

$$FA = \frac{\sqrt{(\lambda_1 - \lambda_2)^2 + (\lambda_2 - \lambda_3)^2 + (\lambda_3 - \lambda_1)^2}}{\sqrt{2(\lambda_1^2 + \lambda_2^2 + \lambda_3^2)}}$$

which measures the degree of directionality of diffusivity.

The primary eigenvector implies the main orientation of the microstructure. By following its orientation, we can perform tractography to reveal fiber connectivity. This can be done as a whole brain to express the global connectivity or as an individual region or between two regions

to express local connectivity. Any brain abnormality that alters the fiber path from the normal connection may be related to the associated functional imparity.

With the development of other non-Gaussian diffusion models that are able to resolve crossing fibers, higher angular resolution with increasing number of diffusion directions are needed. While it leads to higher SNR as well as improved fiber orientation model, it comes at a cost of longer scan time. The added scan time often proves to be a challenge for specific groups of patients such as newborns. Often, sedation is not consented by the patients' parents, leading to motion corrupted images. The corrupted diffusion-weighted images will need to be excluded as removing the entire volume in the diffusion-encoding direction. This results variations in DTI parameters and its effect is discussed in Chapter 2.

Diffusion protocols, in general, are 2D sequences due to the fact that 3D sequences take much longer time than 2D ones. DTI scans has long acquisition time as total scan time is proportional to the number of diffusion-encoding directions. However, mouse brains have very small size (an adult brain has approximately 7mm x 10mm x 13mm in each dimension), a 2D sequence may fail to capture some important but small structures. Thus, 3D sequence is more desired than a 2D sequence to achieve higher resolution. In order to perform DTI scans on a subject *in vivo* with limited scan time, a fast imaging sequence is required. On clinical scanners of 3T and 1.5T, echo-planar imaging (EPI) is commonly applied for DTI scans. However, most of the rodent studies are conducted at much higher field strength, varying from 7T to 14T, in order to achieve higher SNR. The tradeoff is excessive susceptibility artifacts at high field, resulting uncorrectable EPI images.

A GRASE sequence is able to compensate the long scan time from a 3D sequence and the distortions from multi-echoes by combining gradient and spin echoes. An example of a GRASE sequence is as follows:

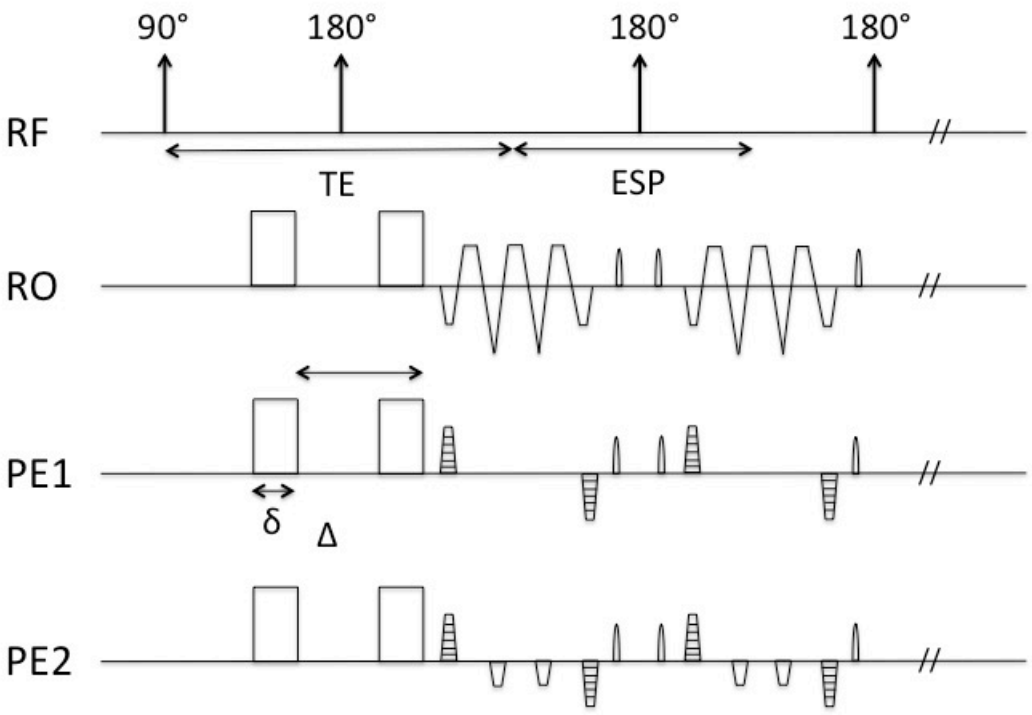

Figure 1.3: An example of 3D GRASE sequence.

Since GRASE has multiple spin echoes and multiple gradient echoes between the spin echoes, it will produce both T2 and off-resonance effects. The standard phase encode ordering, which interleaving each echo along one phase encode direction, has both T2 and off-resonance effects in that phase encode direction (Figure 1.4). This may potentially increase ringing or ghosting artifacts produced by oscillating signal amplitude changes. A separate off-resonance and T2 effects (SORT) phase encode ordering can be applied to reduce such artifacts [4]. It separates the

gradient echoes from different spin echoes into different phase encode lines in a phase encode direction (Figure 1.5). By doing this, the T2 and off-resonance effects will be distributed into different phase encode directions.

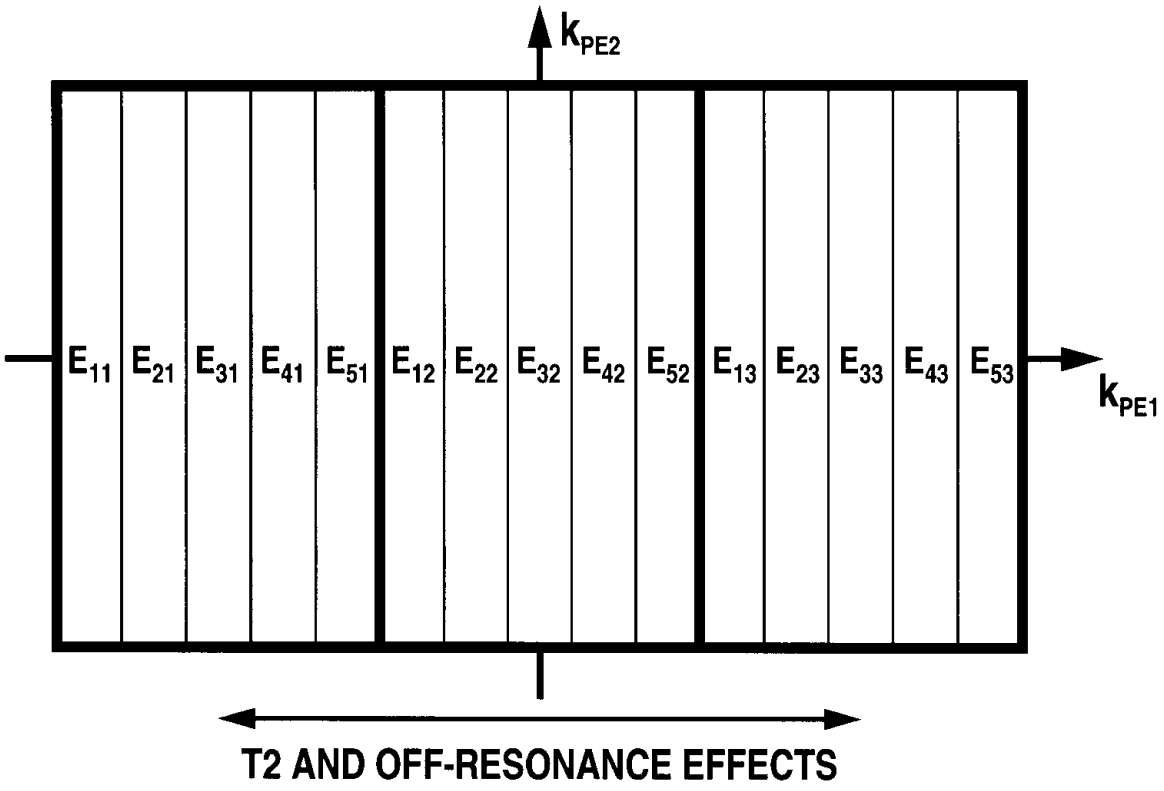

Figure 1.4: A standard phase encode ordering.

It has both T2 and off-resonance effects in that phase encode direction [4].

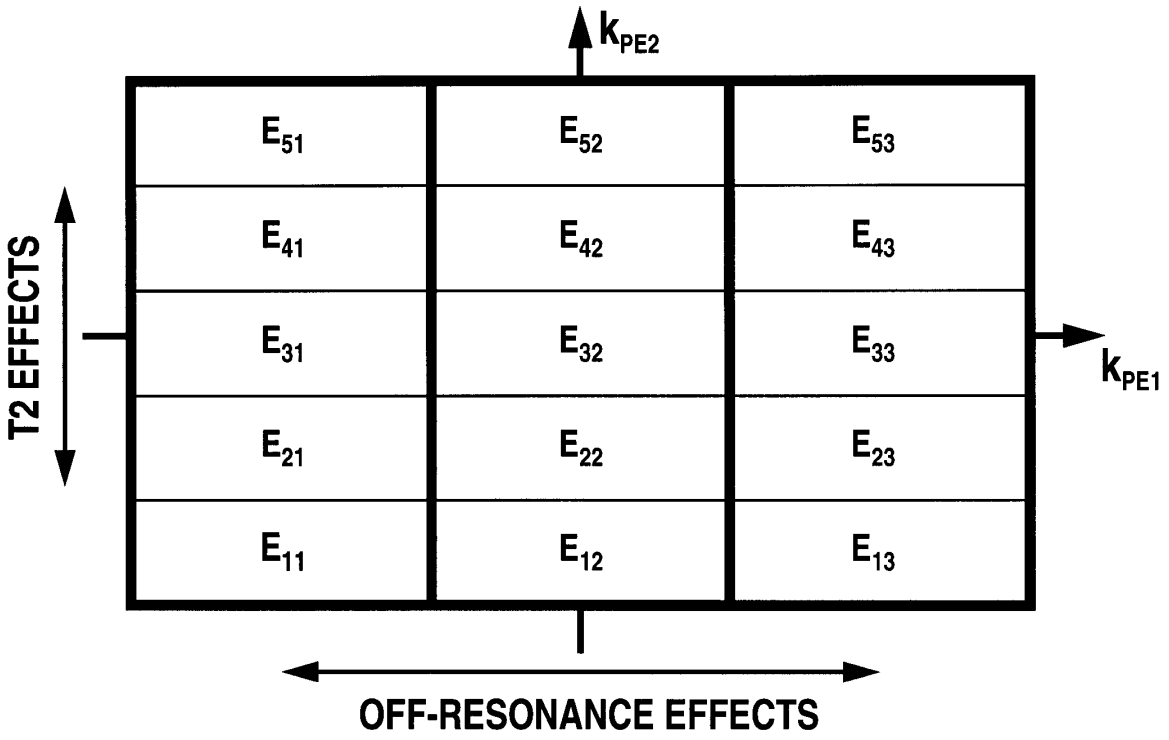

Figure 1.5: A SORT phase encode ordering.

It has T2 and off-resonance effects distributed into different phase encode directions [4].

1.3 MRI applications of normal murine brain development

There are a few advantages of MRI studies using murine models. First, higher field strength can be used, which leads to higher SNR. Second, since scan time is not a major restriction for murine studies, so higher resolution can be achieve for a closer look at the underlying microstructures. Third, human disease or injury models can be modeled to murine to investigate their progression and treatment response using MRI. A large part of this dissertation will focus on MRI applications on murine early brain development, both normal and injured (hypoxic-ischemia).

A few studies have made thorough investigations on normal murine brain development from *ex vivo* MRI. Calabrese *et al.* [5] established first magnetic resonance histology (MRH) atlas of the developing rat brain (Figure 1.6). 5 male rats were imaged at each time point from postnatal day 0 (P0) to P80 with decreasing temporal frequency. They were able to achieve isotropic spatial resolution of 25 μm for 3D T1-weighted images and 50 μm for 6-direction DTI in all cases. They analyzed changes of 26 sub-cortical structures and were able to show different developmental trajectories of these structures.

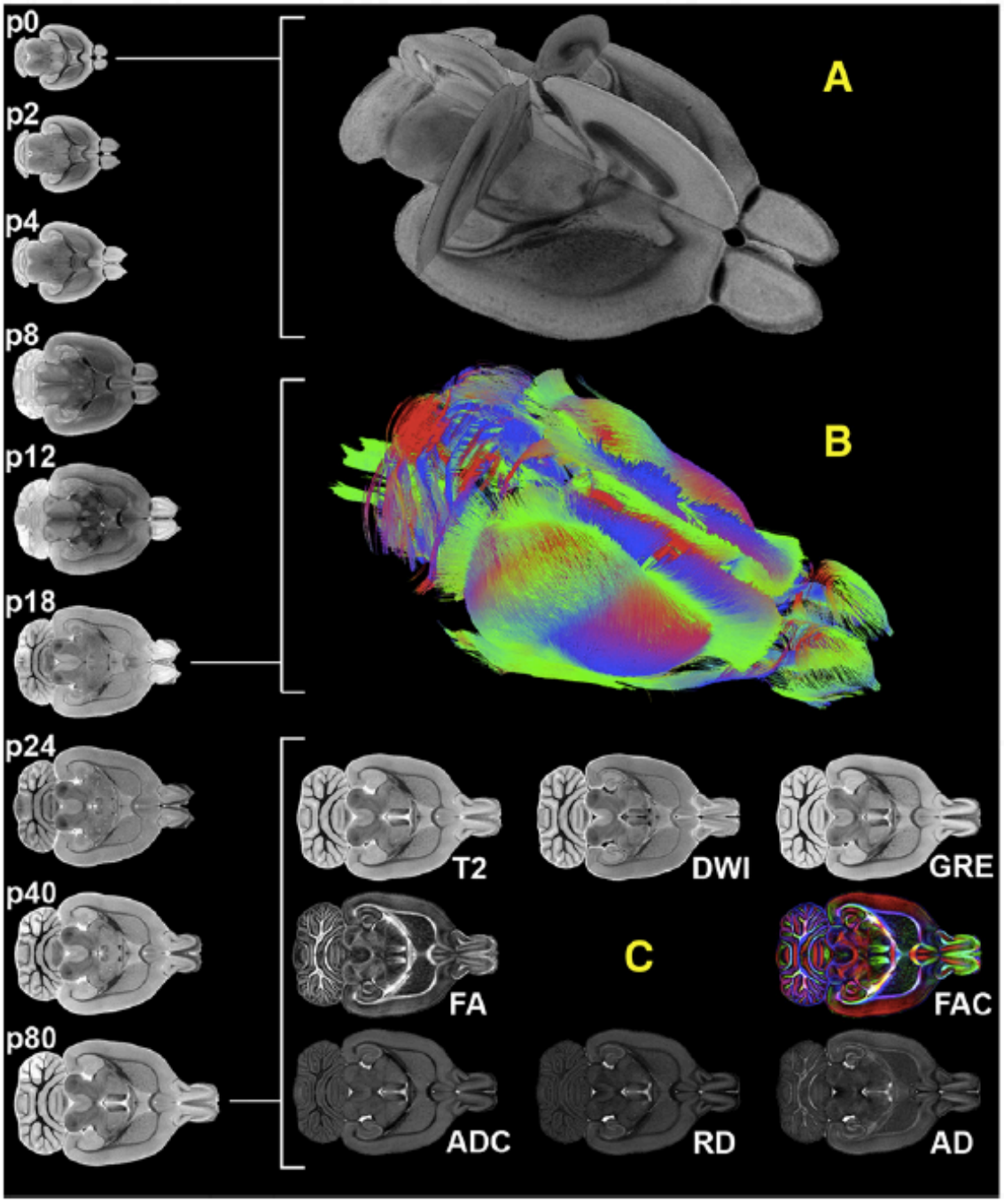

Figure 1.6: A high-resolution developing mouse brain atlas.

It contains multiple time-points from P0 to P80 with T2-weighted and DTI images [5].

Chuang *et al.* [6] conducted a study of mice from embryonic day 12 (E12) to P80 with different subject number at each time point. Their 6-direction 3D DTI scans had resolution ranged from 80 μm isotropic of embryonic samples to 125 μm isotropic of adult brains. Unlike the above-mentioned study, which performed volumetric analysis on T-1weighted images, this study used a T2-weighted image with same FOV and resolution as the diffusion acquisition for volumetric analysis of 8 major white matter structures with addition to whole brain, neocortex, cerebellum and hippocampus. One observation from these two studies is that rats generally have a longer development trajectory than mouse, as rats have most of its structures reach maximum volume after P40 and some are still developing at P80, while most of structures of mice reach their volume plateau around P20 (Figure 1.7). It is important to take this difference in account for future murine brain development studies because sometimes researchers regard the results from either of these species as a general observation for murine.

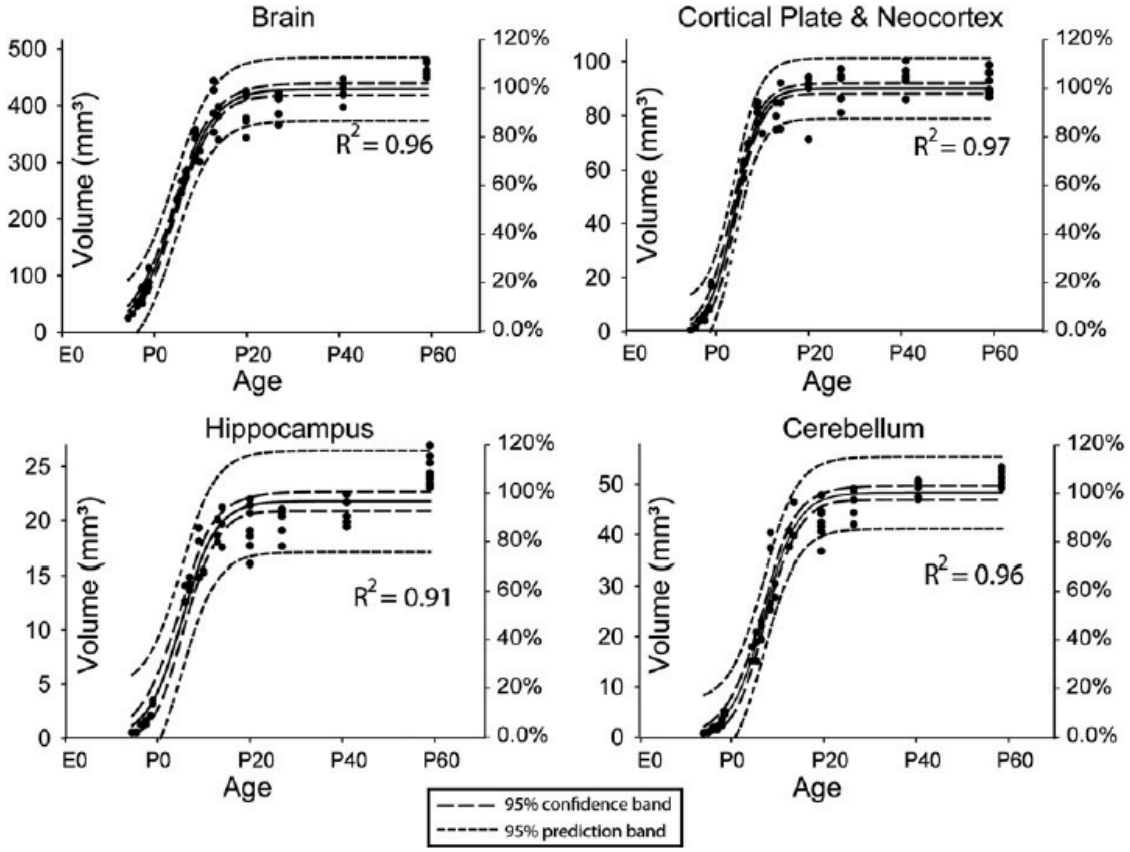

Figure 1.7: Volume analysis of the whole brain and its substructures during early brain development of mice.

Global and local structures reached peak volume around P20 [6].

With the development of 3D GRASE, Wu et al were able to perform *in vivo* mouse DTI experiments. An isotropic resolution of 125 μm on 12-direction diffusion was obtained within 1.5 to 2.5 hours depending on the brain size. Compare with the previous 6-direction DTI in 24 hours, this study has accomplished huge improvement in diffusion resolution and scan time. This has enabled potential future studies on longitudinal investigation of local structures due to its high resolution and short acquisition time *in vivo*.

Another group [7] has developed spatial-temporal mouse atlas on everyday from P1 to P11. Image contrast has always been a challenge for neonatal brain scans because many structures are still undeveloped or under development and subtle or mild myelination has made the difficulty to separate the structures. In this study, their manganese-enhanced T1-weighted imaging has greatly improved image contrast in neonatal brains, and been able to identify and quantify more structures and nuclei in cerebrum and cerebellum compared to previous murine MRI studies (Figure 1.8).

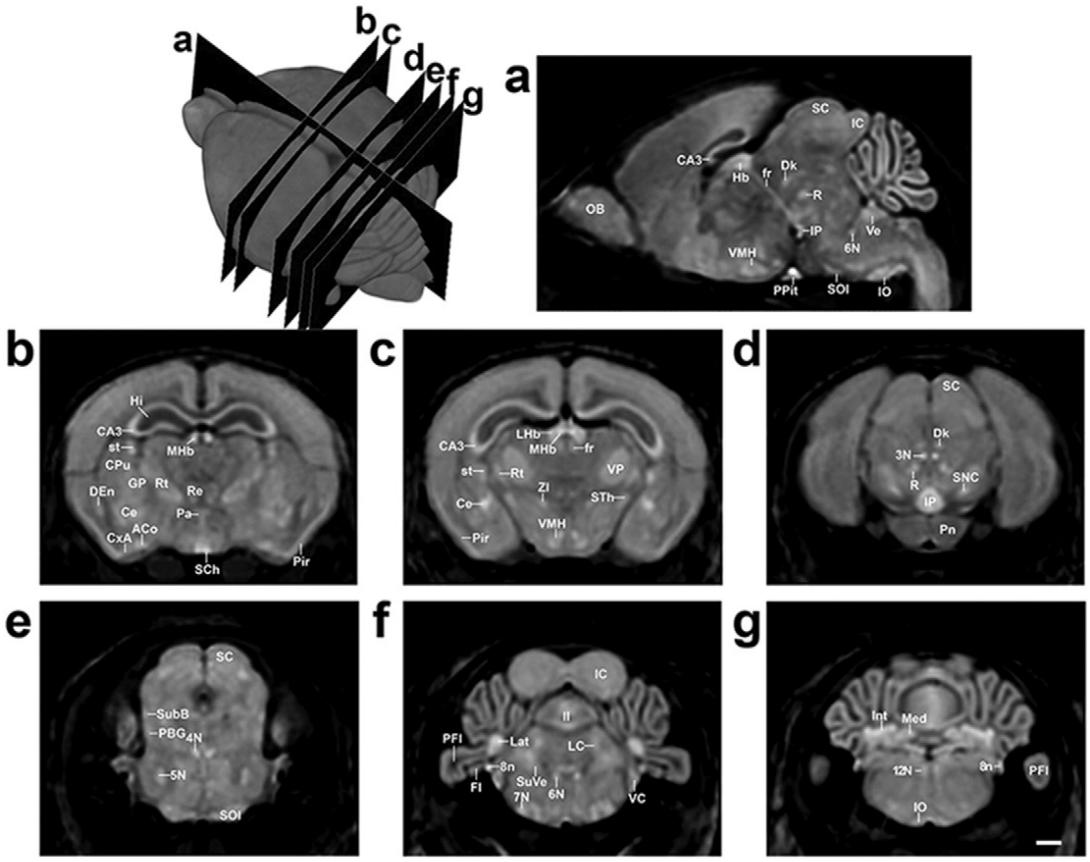

12N	hypoglossal nucleus	LHb	lateral habenular nucleus
II	lobule 2 of the cerebellar vermis	Med	medial cerebellar nucleus
3N	oculomotor nucleus	MHb	medial habenular nucleus
4N	trochlear nucleus	OB	olfactory bulb
5N	motor trigeminal nucleus	Pa	paraventricular nucleus of the hypothalamus
6N	abducens nucleus	PBG	parabigeminal nucleus
7N	facial nucleus	PFl	paraflocculus
8n	vestibulocochlear nerve	Pir	piriform cortex
ACo	anterior cortical amigdaloid nucleus	Pn	pontine nuclei
CA3	field ca3 of the hippocampus	R	red nucleus
Ce	central amygdaloid nucleus	Re	reuniens thalamic nucleus
CPu	caudate putamen (striatum)	Rt	reticular nucleus
CxA	cortex-amygdala transition zone	SC	superior colliculus
DEn	dorsal endopiriform nucleus	SCh	suprachiasmatic nucleus
Dk	nucleus of darkschewitsch	SNC	substantia nigra
Fl	flocculus	SOl	superior olive lateral
fr	fasciculus retroflexus	st	stria terminalis
GP	globus pallidus	STh	subthalamic nucleus
Hb	habenular	SubB	subbrachial nucleus
Hi	hippocampus	SuVe	superior vestibular nucleus
IC	internal capsule	VC	ventral cochlear
Int	interposed cerebellar nucleus	Ve	vestibular nuclei
IO	inferior olivary nucleus	VMH	ventral medial nucleus of the hypothalamus
IP	interpeduncular nucleus	VP	ventroposterior nucleus of thalamus
Lat	lateral (dentate) cerebellar nucleus	ZI	zona incerta
LC	locus coeruleus		

Figure 1.8: Manganese-enhanced T1-weighted image of developing mouse brain.

It depicted much better contrast than previous studies without manganese-enhancement. Many substructures were able to be identified with manganese-enhancement [7].

1.4 MRI applications of hypoxic-ischemic mouse brains

The validity of T2- and DW-weighted images as markers for HI injury detection has been justified by various studies based on histology results. Albensi *el al.* [8] demonstrated high correlation between lesion extent of hyperintensity on T2-weighted images measured 72 hours post-HI and lesioned area on histology. Wang *el al.* [9] showed evidence of correlation between lesion size based on ADC map 1-2 hour post-HI and final irreversible infarct volume based on histology.

One greatest advantage of MRI is its noninvasiveness, which provides the feasibility of studying multiple time points on the same subject for investigation of the longitudinal injury progression. Aden *el al.* [10] have shown T2-weighted and T2 changes at various time points from 3 hours to 5 days post HI. Hyperintensity on both T2-weighted and T2 images was observed as global injury of almost the entire ipsilateral hemisphere at 3 hours to more localized injury at 5 days (Figure 1.9).

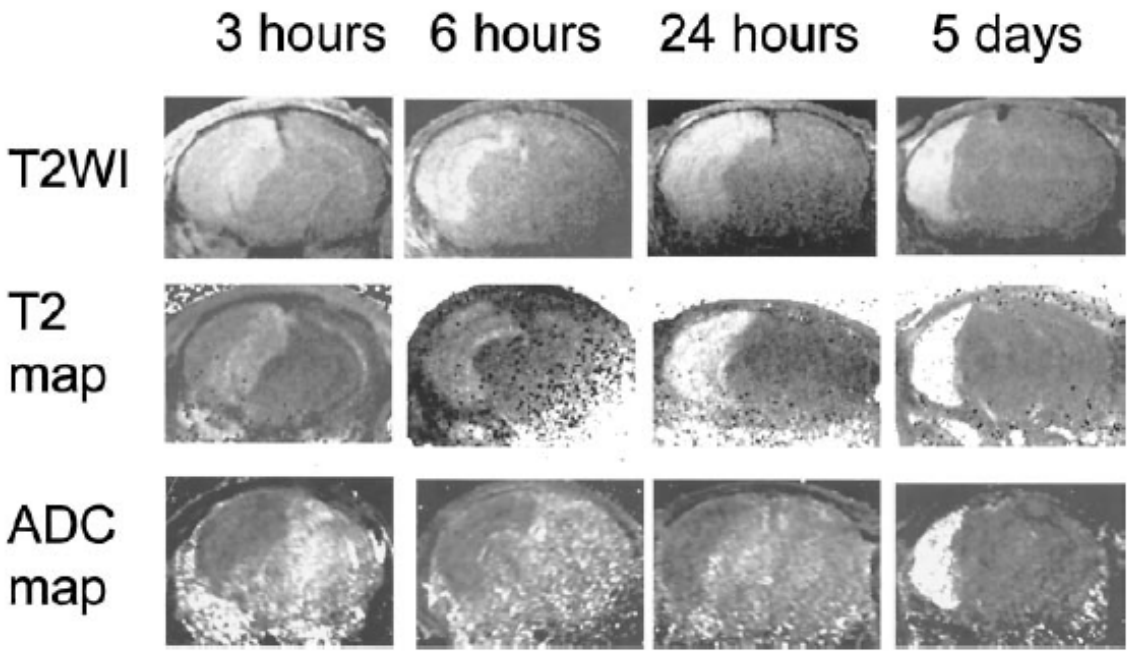

Figure 1.9: Injury progression from 3 hours to 5 days post HI on T2-weighted, T2 and ADC maps.

The contrast of T2 map starts to reverse 6 hours post HI, and the contrast of ADC starts to reverse 24 hours post HI [10].

Tuor *el al.* [11] conducted MRI of rats in a chamber after right carotid artery incision and recovery, while the chamber was infused with humidified 8% oxygen and 0.1-0.5% isoflurane for 2 hours from the start of MRI. They showed T2-weighted hyperintensity was observed from 45 minutes of HI (Figure 1.10). They also demonstrated an injury recovery right after HI (shown as normal intensity on T2-weighted images) and then hyperintensity again from 23 min post HI (Figure 1.11). Their analysis about areas of injury in specific regions indicated an increase in areas of hyperintensity during HI, a decline with reperfusion, and a subsequent increase over different times depending on the region.

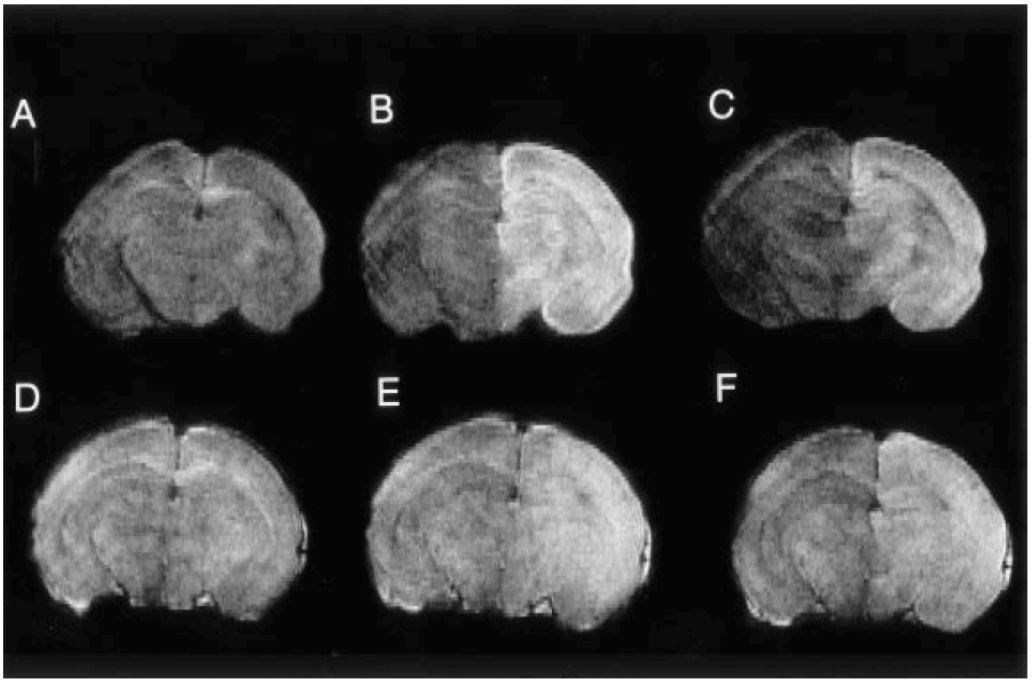

Figure 1.10: Diffusion-weighted images after the start of hypoxia on a P7 rat.

Diffusion-weighted images at 33 min (A), 60 min (B), and 85 min (C), and T2-weighted images at 20 min (D), 47 min (E), and 72 min (F) after the start of hypoxia [11].

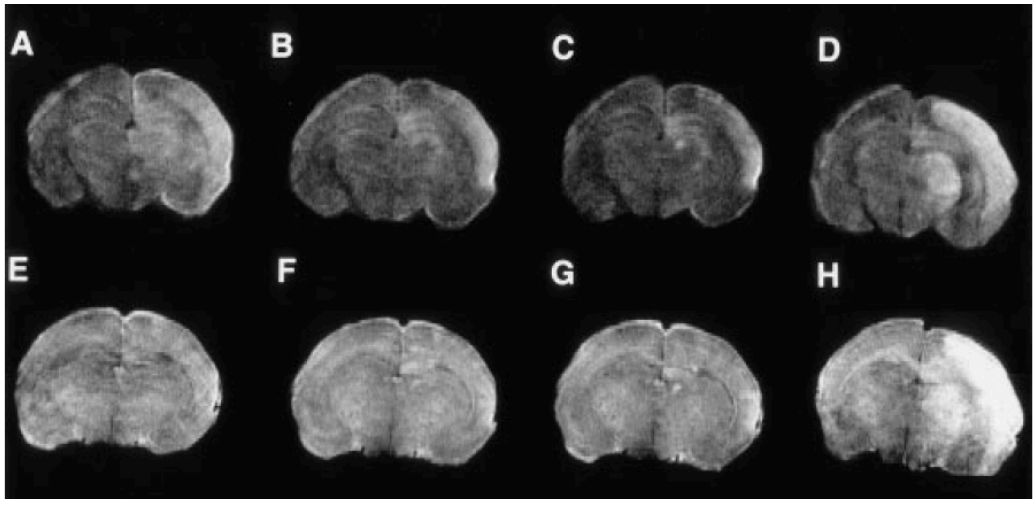

Figure 1.11: Diffusion-weighted images post HI of a P7 rat.

Diffusion-weighted images at 12 min (A), 33 min (B), 66 min (C), and 21 h (D), and T2-weighted images at 23 min (E), 48 min (F), 76 min (G), and 21 h (H) post HI [11].

Cortex, hippocampus and striatum are commonly recognized as the major areas of injury. Studies have also looked for more regional information on the injury. Qiao *el al.* [12] has distinguished the size and localization of injury based on the injury level. They concluded that white matter damage prevailed in mild injury from 45 min hypoxia, while moderate injury from 90 min hypoxia produced comparable damages in both white and grey matters.

Due to advancement of oscillating gradient diffusion MRI and 3D GRASE, better contrast and higher resolution can be achieved to measure small regional changes. Aggarwal *et al.* [13] presented layer-specific contrasts of hippocampus, and found significant lower ADC in the pyramidal (Py) and granule (GrDG) layers in response to HI (Figure 1.12).

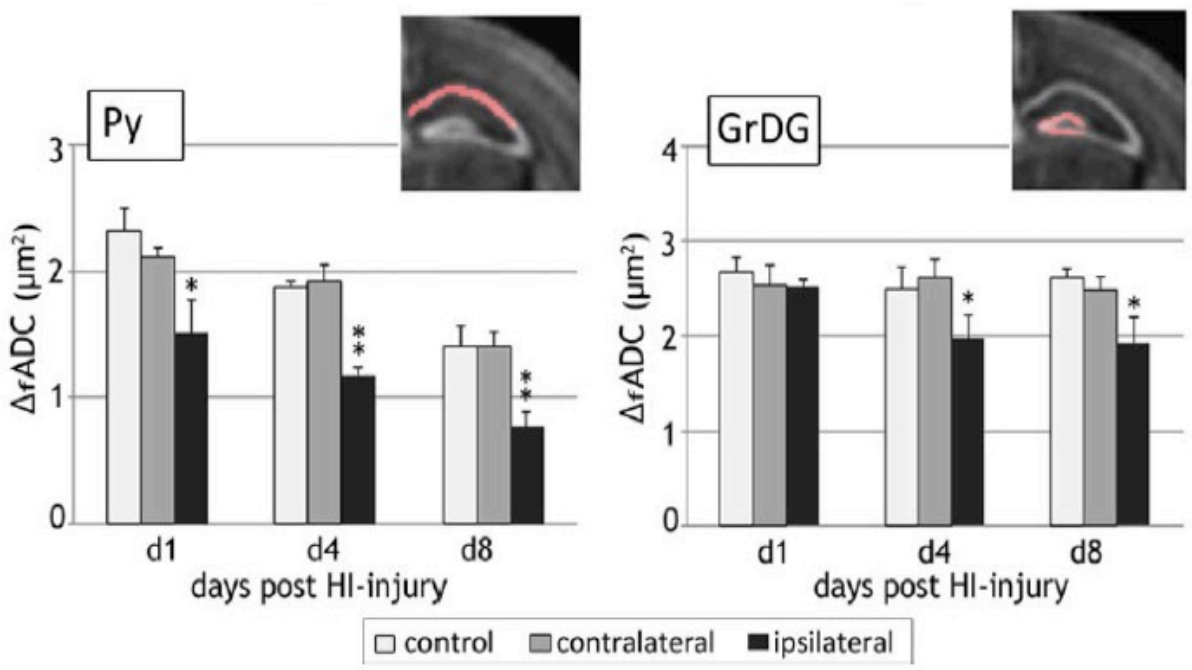

Figure 1.12: High-resolution 3D MRI showed hippocampal substructural changes in response to HI.

ADC was lower in ipsilateral Py and GrDG layers of hippocampus, which were drawn manually from high-resolution 3D T2-weighted MRI [13].

1.5 Development of dynamic nuclear polarization (DNP) and its applications *in vivo*

^{1}H Magnetic Resonance Spectroscopy (MRS) offers the ability to examine metabolic properties during normal brain maturation [14-16] and HI injury [17-19] but it only provides steady state information of metabolites due to relatively low metabolic concentrations and the long acquisition time. ^{13}C spectroscopy provides yet another perspective, allowing investigation of metabolic exchange and labeled neurotransmitters such as glutamate, GABA and aspartate in the developing murine brain [20-22]. Sensitivity of ^{13}C is low because its natural abundance is only about 1% in living organisms, so experiments are done with enriched metabolic compounds. Even with enriched ^{13}C, most of the ^{13}C MRI studies require a long scan time, which most common in cultured cells and extracted tissues [23-26], restricting the feasibility of longitudinal experiments to study long-term responses after the injury during brain development. *in vivo* studies require infusion of metabolites for minutes or even hours [27, 28], which makes it very difficult for neonatal mice with small blood volumes. The long scan time also means that measurements are only indicative of stable metabolic conversions, instead of gauging rapidly changing dynamic conversion after injury or treatment.

In 2003, Ardenkjær-Larsen *et al.* [29] introduced a new method to dynamically quantify metabolism using hyperpolarized ^{13}C, which enabled an entirely different avenue to study metabolism *in vivo*, in real time. DNP has been proven to increase ^{13}C NMR signal more than 10,000 fold, allowing investigation of ^{13}C metabolic exchanges *in vivo* [30]. It requires a free radical (unpaired electron) to be added to the sample and the high electron spin polarization is transferred to the nuclear spins by microwave radiation in solid state. After the nuclear spins of

the sample are hyperpolarized under a 3.35 Tesla magnet at 1.2 Kevin, a pressurized, high temperature solution is injected into the sample to make a PH-neural solution, to be collected and ready to inject into *in vivo* animals or *in vitro* cells, while preserving its nuclear polarization.

Golman *et al.* [31] first demonstrated the feasibility of DNP on *in vivo* rabbits. Once a hyperpolarized substrate is injected into a living mammal, real-time ^{13}C metabolic imaging is performed to study metabolism by following the substrate as it participates in a biochemical process. However, the hyperpolarization of the nuclear spins return to thermal equilibrium after a very short time at room temperature. Therefore, a metabolite must be carefully chosen in order to visualize the metabolic pathway within this time period. Hyperpolarized ^{13}C-1 labeled pyruvate has been used to track *in vivo* metabolism in animals [32, 33] and human [34, 35]due to its rapid delivery and uptake by the cells in various organs, and its quick conversion into lactate, alanine and/or carbon dioxide through various metabolic pathways (Figure 1.13).

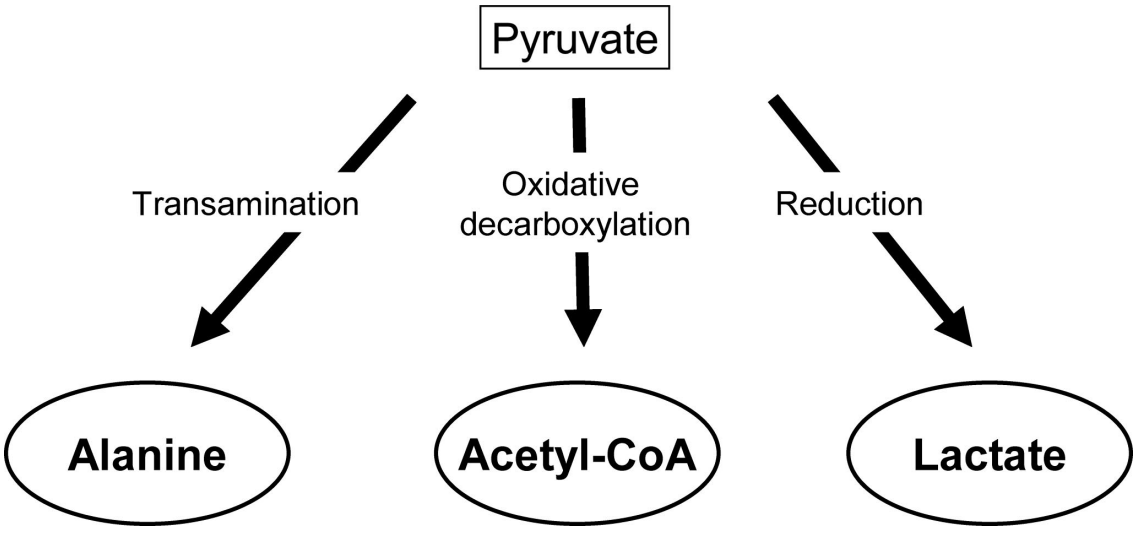

Figure 1.13: Simplified overview of the main metabolic pathways of pyruvate.
Alanine, acetyl-CoA and lactate are produced by different pathways from pyruvate. [32].

Golman *et al.* [32] applied dynamic imaging with very short (~ 8 second) temporal resolution hyperpolarized ^{13}C-1 labeled pyruvate's real-time conversion into different substrates in rats (Figure 1.14 and Figure 1.15).

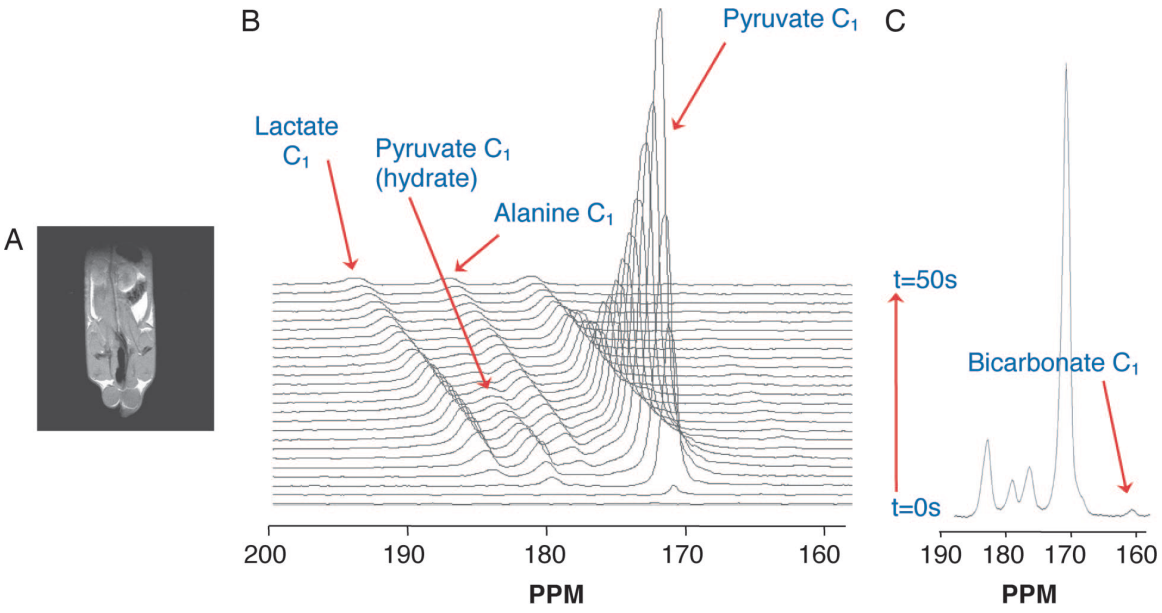

Figure 1.14: Dynamic spectra of pyruvate metabolic pathways of a rat detected by MRI.

Spectra with 3-second time interval after the injection of ^{13}C-1 labeled pyruvate (B) from the lower part of a rat (A). (C) The formation of bicarbonate can be seen when adding all spectra [32].

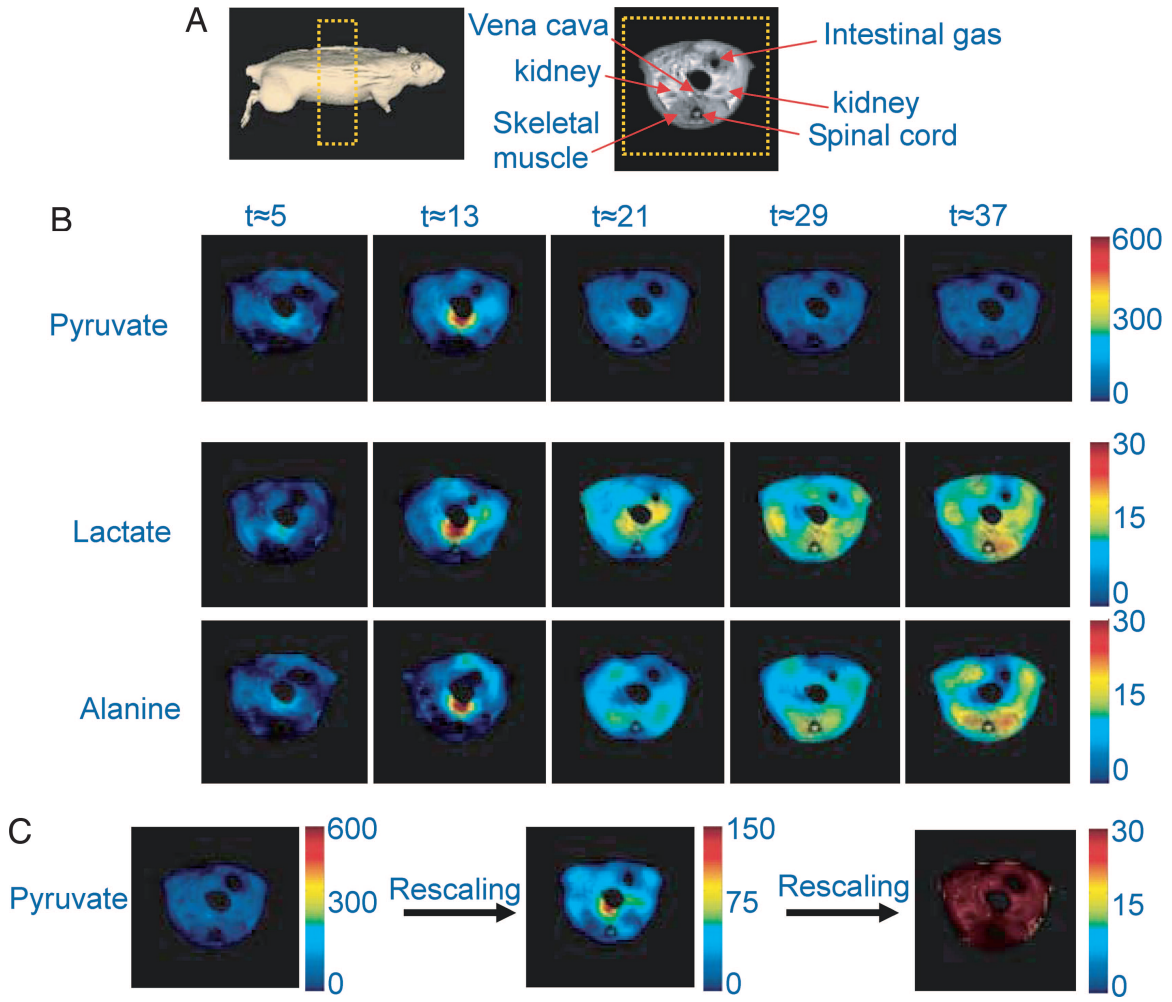

Figure 1.15: Dynamic intensity maps of pyruvate and its substrates.

The time course of the build-up of lactate and alanine in the imaged slice of the rat [32].

The innovation of hyperpolarized ^{13}C has advanced its applications on cancer diagnosis, due to its high sensitivity compared to traditional MR methods. Park *et al.* [33] showed clear distinctions on hyperpolarized ^{13}C images on tumor progression before and after treatment between the control and treatment groups, while conventional T1-post-Gd MRI fail to recognize the difference.

Most of the current hyperpolarized ^{13}C applications are on cancer diagnosis and all have showed promising results on detecting metabolic change in cancer tissues. This dissertation will focus on a new area of application, which is metabolic change during early brain maturation in normal mice in Chapter 3 and in mice with hypoxic ischemia in Chapter 4.

Chapter 2 : Effects of rejecting diffusion directions on tensor-derived parameters

2.1 Introduction

As discussed in Chapter 1.2, diffusion tensor imaging (DTI) is a powerful non-invasive tool to inspect brain microstructure and abnormalities and has been widely used in neonatal applications. The resultant scalar parameters such as fractional anisotropy (FA), mean diffusivity (MD), axial diffusivity (AD), radial diffusivity (RD) are used in the evaluation of brain injury [36, 37], tumors [38], neurodegenerative and white matter diseases [39, 40] in general. Primary eigenvectors (V1), derived from the tensor model, commonly serve as the basis for fiber tractography, which uses these orientation estimates to reconstruct streamlines that are assumed to represent the underlying white matter architecture [41, 42].

In order to achieve the most accurate estimate of the diffusion tensor, many studies have investigated various diffusion weighting direction schemes. Jones, Horsfield [43] proposed the minimization of potential energy of electrostatic repulsion by points on the sphere, and Skare, Hedehus [44] analyzed the dependence of noise on the condition number of the transforming matrix to the approach of using minimum condition number. The optimal number of encoding directions has also been discussed extensively. Papadakis, Murrills [45] evaluated variations of signal-to-noise ratio (SNR) and suggested that minimum of 18 to 21 uniform diffusion directions were needed for robust tensor estimation. However, Hasan, Parker [46] represented that no

significant advantage could be achieved by using more than six encoding directions as long as they were icosahedral, and later Batchelor, Atkinson [47] demonstrated that the icosahedral schemes was rotationally invariant so that noise was independent of fiber orientation or the relative orientation of the tensor with respect to the laboratory frame.

The quality of the diffusion-weighted images can be affected by artifacts introduced by subject motion, respiration or cardiac pulsation. While such artifacts can be diminished by applying "navigator echoes" [48] or cardiac gating [49, 50], these techniques are generally not employed due to added complexity in the acquisition and a longer scan time. In the absence of these techniques, and especially in the severe cases such as non-sedated pediatric subjects or subjects with tremor, rejection of selected diffusion weighted images corrupted by motion is often preformed as a post-processing step before estimating the tensor. The rejection can be done by discarding the entire "volumes" (certain diffusion directions) of diffusion-weighted images [51, 52], or by automatic exclusion of outliers during the tensor estimation [53]. However, the consequence of rejecting diffusion-weighted images has not yet been carefully considered. In this chapter, we investigated the effect of discarding one or more sets of diffusion weighted images on the final results by analyzing the changes in the parameters such as FA, MD, AD, RD and V1. Both accuracy and precision of these parameters were evaluated for various diffusion rejection schemes as described in Methods section.

2.2 Methods

The study was approved by the Committee on Human Research (CHR) of the University of California, San Francisco. Written informed consent was obtained from all participants.

Six healthy adults (right-handed, aged between 24 and 31, all female) were scanned on a 3T GE MR scanner using a spin echo (SE) echo planar imaging (EPI) DTI sequence with TR/TE=17 s/90 ms, FOV=25.6 cm×25.6 cm, 128×128 matrix, slice thickness of 2 mm, 30 directions using Jones30 scheme as shown in Table 2.1 [43] with b=1000 s/mm^2. Sixty-six contiguous slices were acquired to cover the entire brain. One b0 volume was acquired. The total scan time was about 9 minutes.

Table 2.1: Jones30 gradient scheme

Index	Gx	Gy	Gz
1	0	1	0
2	0.986	0.166	0
3	0.664	-0.11	0.74
4	-0.419	0.901	-0.11
5	-0.601	-0.169	0.781
6	-0.386	-0.815	0.433
7	0.366	0.656	0.66
8	0.8	0.582	0.143
9	0.259	0.9	0.35

Index	Gx	Gy	Gz
10	-0.698	0.693	0.178
11	-0.924	0.357	-0.14
12	-0.488	0.543	-0.683
13	-0.396	-0.525	0.753
14	0.689	-0.639	0.341
15	-0.013	-0.33	-0.944
16	-0.783	-0.524	0.335
17	-0.065	0.609	-0.791
18	-0.233	0.22	-0.947
19	-0.91	-0.004	-0.415
20	0.627	-0.511	-0.589
21	0.737	0.414	0.535
22	0.139	-0.679	-0.721
23	-0.296	0.884	0.362
24	0.432	0.262	0.863
25	0.185	0.088	-0.979
26	-0.907	0.294	0.302
27	-0.089	0.887	-0.453
28	-0.443	0.257	0.859
29	0.867	0.086	-0.491
30	0.504	0.863	-0.025

Each diffusion volume was co-registered with the b0 volume using the FSL eddy-correct tool[54] and structures outside the brain were removed using BET tool [55]. Diffusion tensor parameters were estimated using dtifit function from FSL. Three rejection schemes were applied to the fully acquired set of 30 directions: random rejection, uniform rejection and clustered rejection, which are described in detail below.

2.2.1 Random rejection

Rejections of 1 to 24 randomly selected directions from the total of the 30 directions were performed. For each rejection, FA, MD, AD, RD and V1 maps were generated and compared with reference maps generated from all 30 volumes. The angle α between the primary eigenvectors of the remaining data and the reference data at each point was calculated using:

$$\alpha = \cos^{-1}(\mathrm{V1}_{\mathrm{rej}} \cdot \mathrm{V1}_{\mathrm{ref}})$$

where $\mathrm{V1}_{\mathrm{rej}}$ represents the primary eigenvector of the subsampled dataset resulting after the rejection was applied and $\mathrm{V1}_{\mathrm{ref}}$ is the primary eigenvector of the reference dataset. The calculated α was between -90° and 90°. As V1 represents the orientation and not the direction of the largest eigenvalue, angles were constrained to be non-negative. A map of α was computed voxel by voxel for each number of rejected directions.

At each level of data reduction (ranging from 1 to 24 rejected directions), 100 different sub-sampled data sets were generated by eliminating data corresponding to different directions picked at random. The mean and standard deviation of FA ($\mathrm{FA}_{\mathrm{mean}}$, $\mathrm{FA}_{\mathrm{std}}$), MD ($\mathrm{MD}_{\mathrm{mean}}$,

MD_{std}), AD (AD_{mean}, AD_{std}) and RD (RD_{mean}, RD_{std}) were calculated for each voxel. In order to visualize the change in V1, the cone of uncertainty in each voxel was generated for each number of rejections[56], and the angle of the cone was taken at the 95% confidence level of α over the 100 iterations.

2.2.2 Uniform rejection

The Jones30 diffusion scheme is based on minimum potential energy of electrostatic repulsion by points on the sphere, which results uniformly distributed points on the sphere[43]. Uniform rejection describes a data reduction that will result in the remaining points to be uniformly arranged on the sphere. Here we investigated 15, 20 and 24 rejections, resulting in 15, 10 and 6 remaining directions as proposed by Landman, Farrell [57].

2.2.3 Clustered rejection

It has been demonstrated in the results that the remaining vectors evenly distributed on a sphere is the optimal rejection scheme (see Results). In contradistinction to this effect, we were also interested in the outcomes if all of the rejected directions are close to each other and concentrated in a particular angular region. Here we performed rejections of diffusion encoding directions close to one of the main axes of the MRI scanner space.

For each of the x, y and z axes, which represent the left-right (LR), anterior-posterior (AP) and superior-inferior (SI) directions respectively, we rejected 1 to 24 directions closest to the axis.

For each number of rejections, we calculated FA and α maps. Since the rejections are orientation dependent, but α only shows the degree of change in V1, it does not specify in which direction the change is. Therefore, we employed φ and θ to explore V1 change in the x-y plane and towards the z-axis, where φ is the angle difference between $V1_{rej}$ and $V1_{ref}$ in the x-y plane and θ is the angle difference between $V1_{rej}$ and $V1_{ref}$ towards the z-axis.

2.2.4 Comparison between protocols with different acquisition parameters

The accuracy and precision of DTI parameters are affected by the SNR, and the SNR depends on the diffusion acquisition parameters such as the number of b0 volumes involved in tensor estimation, b-value, and the number of diffusion directions. In order to evaluate the influence of different acquisition parameters on the effects of rejecting diffusion directions, we performed the following comparisons on FA and V1 for random rejections: (1) comparison between one b0 volume, two b0 volumes and four b0 volumes with b=1000 s/mm^2 and 30 directions, where four b0 volumes was expected to yield the best SNR theoretically by the optimal ratio of number of diffusion directions to the number of b0 volumes as about 7 to 1 [43]; (2) comparison between b=600 s/mm^2, b=1000 s/mm^2 and b=2000 s/mm^2 with one b0 volume and 30 directions, and we expected a higher b-value would result in a lower SNR; (3) comparison between 15 directions, 30 directions and 55 directions based on the equally distribution of points on a sphere by electrostatic repulsion [43] with one b0 volume and b=1000 s/mm^2, where more directions would result in a higher angular resolution, and consequently, a higher SNR. All the other acquisition parameters were kept the same: TR/TE=17 s/90 ms (except TE=91.4 ms for b=2000 s/mm^2),

FOV=25.6 cm×25.6 cm, 128×128 matrix, slice thickness of 2 mm with sixty-six contiguous slices.

2.2.5 ROI analysis

Region of interest (ROI) analysis was performed to evaluate the effect of rejecting diffusion directions. In order to compare the effects of random rejections and uniform rejections on areas of different FA values, four ROIs were chosen on the reference FA map in the genu of corpus callosum (GENU), splenium of corpus callosum (SPL), posterior limb of the internal capsule (PLIC), and the optic radiation (OR), representing white matter regions with high, medium and low FA, respectively (Figure 2.1a). Gray matter regions in caudate nucleus (CN) (Figure 2.1b) and putamen (PU) (Figure 2.1a), and one cerebrospinal fluid region in the lateral ventricles (LV) (Figure 2.1b) were chosen as well. Each region was visually homogeneous with a fixed volume of $28mm \times 8mm \times 4mm$. As shown in Figure 2.1a, GENU and SPL had high FA values in the range of 0.85, PLIC had medium FA values around 0.6, OR had low FA values around 0.4, and PU had very low FA values around 0.2. For each number of rejections, mean FA and mean α of these three ROIs after random and uniform rejections were compared with the reference images.

Two additional regions, anterior limb of the internal capsule (ALIC) and descending corticospinal pathways within the corona radiata (CR), were drawn to analyze the effects of the clustered rejections (Figure 2.1c and 2.1d). In conjunction with GENU, these ROIs cover bundles of white matter fibers orientated primarily along three orthogonal imaging directions: LR, AP and SI.

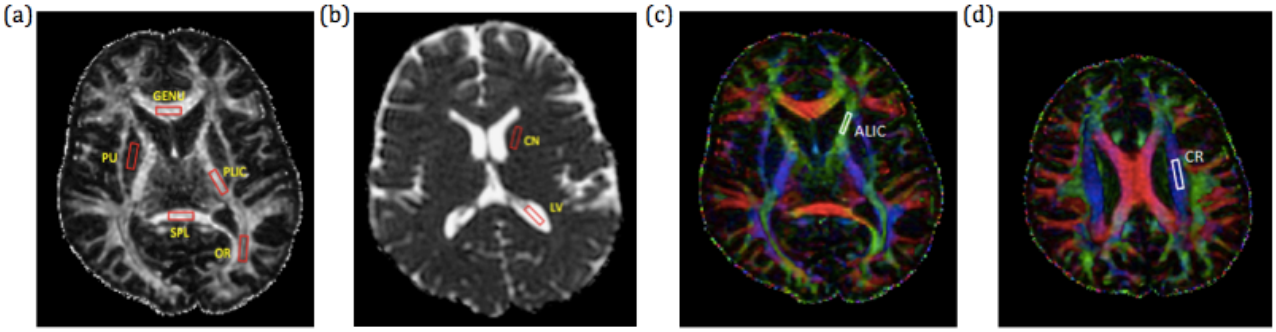

Figure 2.1: FA and color FA map of one subject's brain with ROIs drawn for FA and V1 analysis.

Red represents left-right (LR) orientation of the primary eigenvector (V1), green represents anterior-posterior (AP) orientation, and blue represents superior-inferior (SI) orientation. (a) Genu (GENU) and splenium (SPL) of corpus callosum have FA around 0.85, posterior limb of internal capsule (PLIC) has FA around 0.6, optic radiation (OR) has FA around 0.4, and putamen (PU) has FA around 0.2. (b) Caudate nucleus (CN) and lateral ventricle (LV) in MD map. (c) Anterior limb of internal capsule (ALIC) is in AP part of internal capsule. (d) Descending corticospinal projections within corona radiata (CR) in the motor tract that runs along the SI direction.

Mean and standard deviation of FA, MD, AD, RD and α for each ROI were computed among the six subjects.

2.3 Results

2.3.1 Random rejections and uniform rejections

All six adults showed similar results. As the number of randomly rejected directions increased, the overestimation of both FA and V1 increased (Figure 2.2). Lower FA regions were affected

more than the higher FA regions (Figure 2.2). However, very little change was observed on both FA and V1 for uniform rejections, except the low FA regions (Figure 2.3).

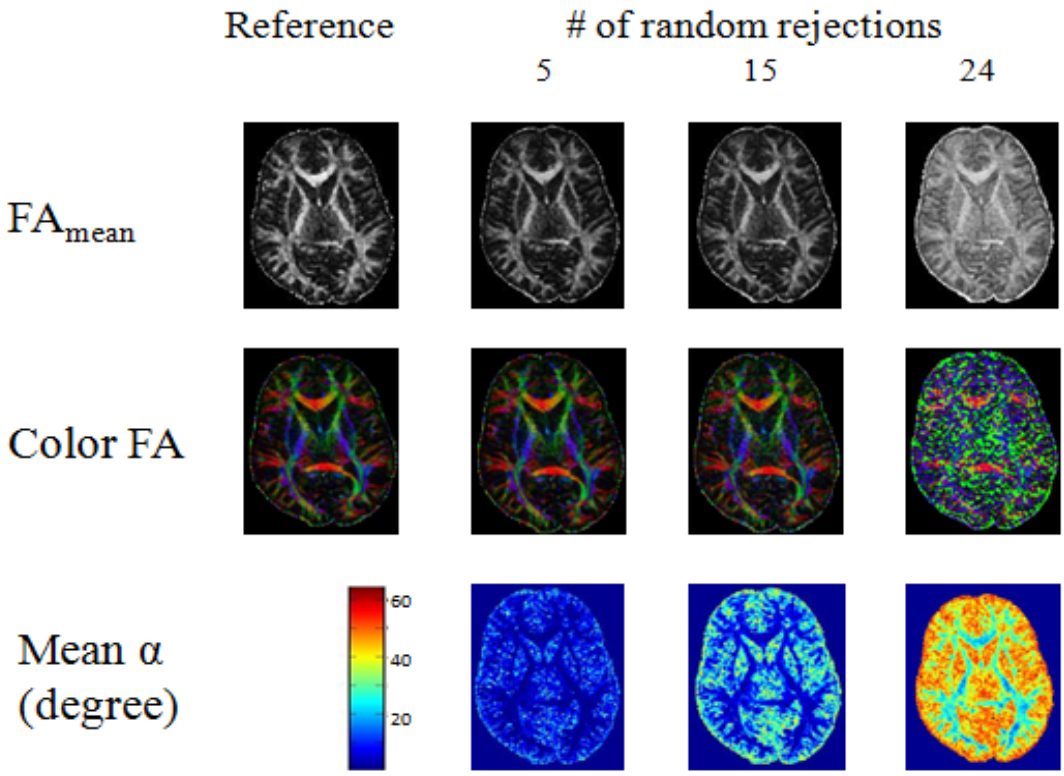

Figure 2.2: FA, color FA and α maps of the same subject as in Figure 2.1 after random rejections.

Comparison between the reference and incomplete data after 5, 15 and 24 random rejections with the reference for one of the subjects. FA_{mean} is the mean FA over 100 iterations. Color FA shows the color-coded FA map in one of the 100 iterations. Mean α is the mean angle change in V1 over 100 iterations.

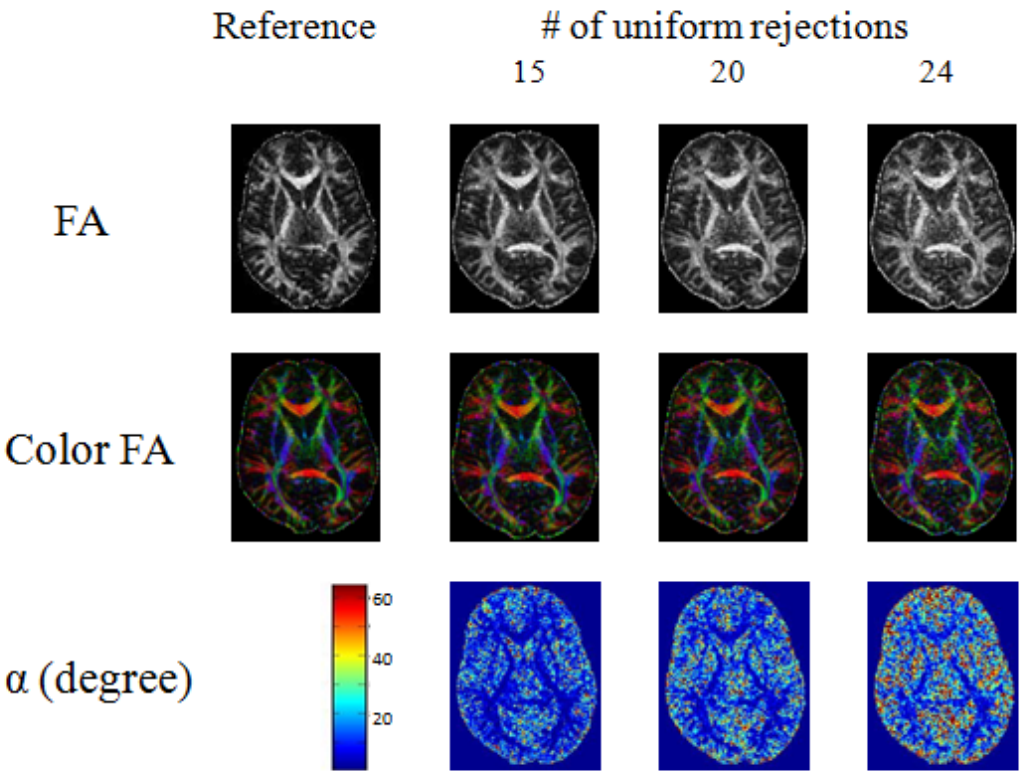

Figure 2.3: FA, color FA and α maps of the same subject as in Figure 2.1 after uniform rejections.

Comparison between the reference and incomplete data after 15, 20 and 24 uniform rejections with the reference for one of the subjects.

The comparison of the effects of random rejections and uniform rejections are shown in Figure 2.4 and Figure 2.5. For random rejections, not only the mean values of FA, AD and RD became more deviated from the reference values, their standard deviations also increased when the number of rejections became larger. More dramatic changes were observed in low FA regions compared to high FA regions. In general, FA and AD increased with higher number of rejections, and RD decreased with higher number of rejections. However, the mean value of MD remained unchanged regardless of the number of rejections. Its standard deviation increased with

greater number of rejections. In contrary, uniform rejections caused very insignificant changes of those parameters, and the changes were again, larger in low FA regions than in high FA regions and increased with the number of rejections.

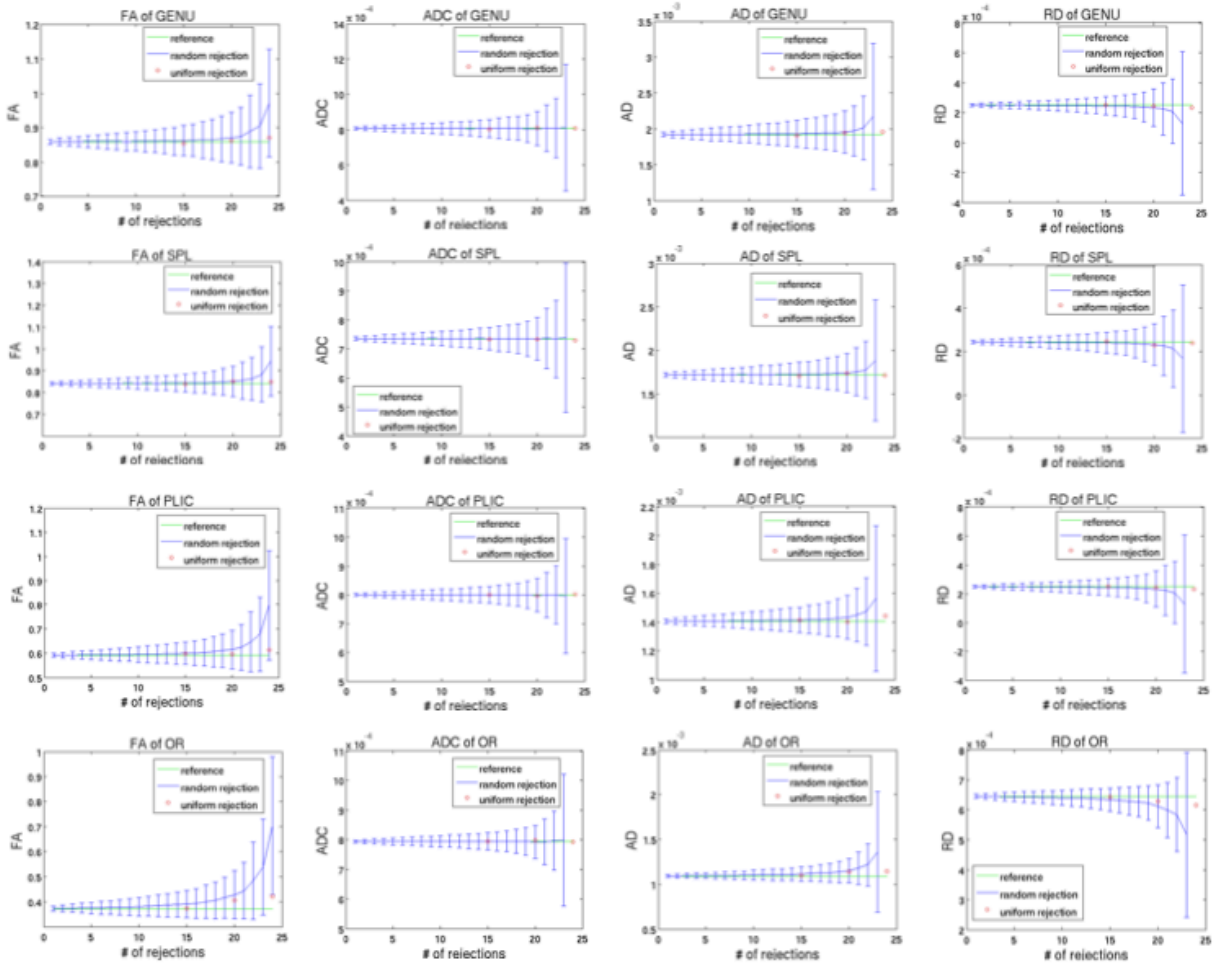

Figure 2.4: Comparison of diffusion parameters between random rejections and uniform rejections for white matter regions.

Comparison of FA, MD, AD and RD between random rejections and uniform rejections for GENU, SPL, PLIC and OR. The mean and standard deviation of random rejections were calculated from 6 subjects for each ROI.

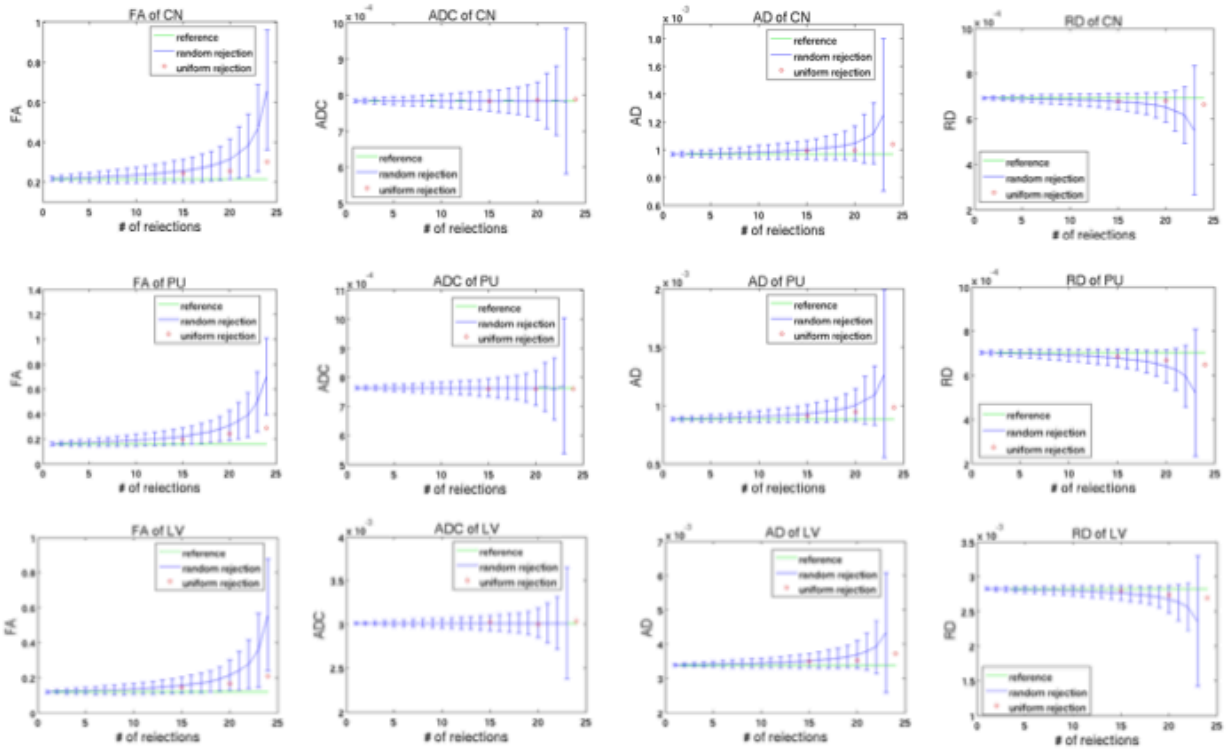

Figure 2.5: Comparison of diffusion parameters between random rejections and uniform rejections for grey matter regions.

Comparison of FA, MD, AD and RD between random rejections and uniform rejections for CN and PU, and a cerebrospinal fluid region, LV. The mean and standard deviation of random rejections were calculated from 6 subjects for each ROI.

From the cones of uncertainty of GENU, PLIC and OR shown in Figure 2.6, one could easily observe the growing overestimation of V1 with increasing number of rejections. This effect was more dominant in low FA regions than high FA regions. Especially in OR (with FA around 0.4), one voxel showed severely ill-defined V1 even with 5 random rejections, and while 20 random rejections were performed, the changes of many voxels were depicted as almost or absolutely flat cones.

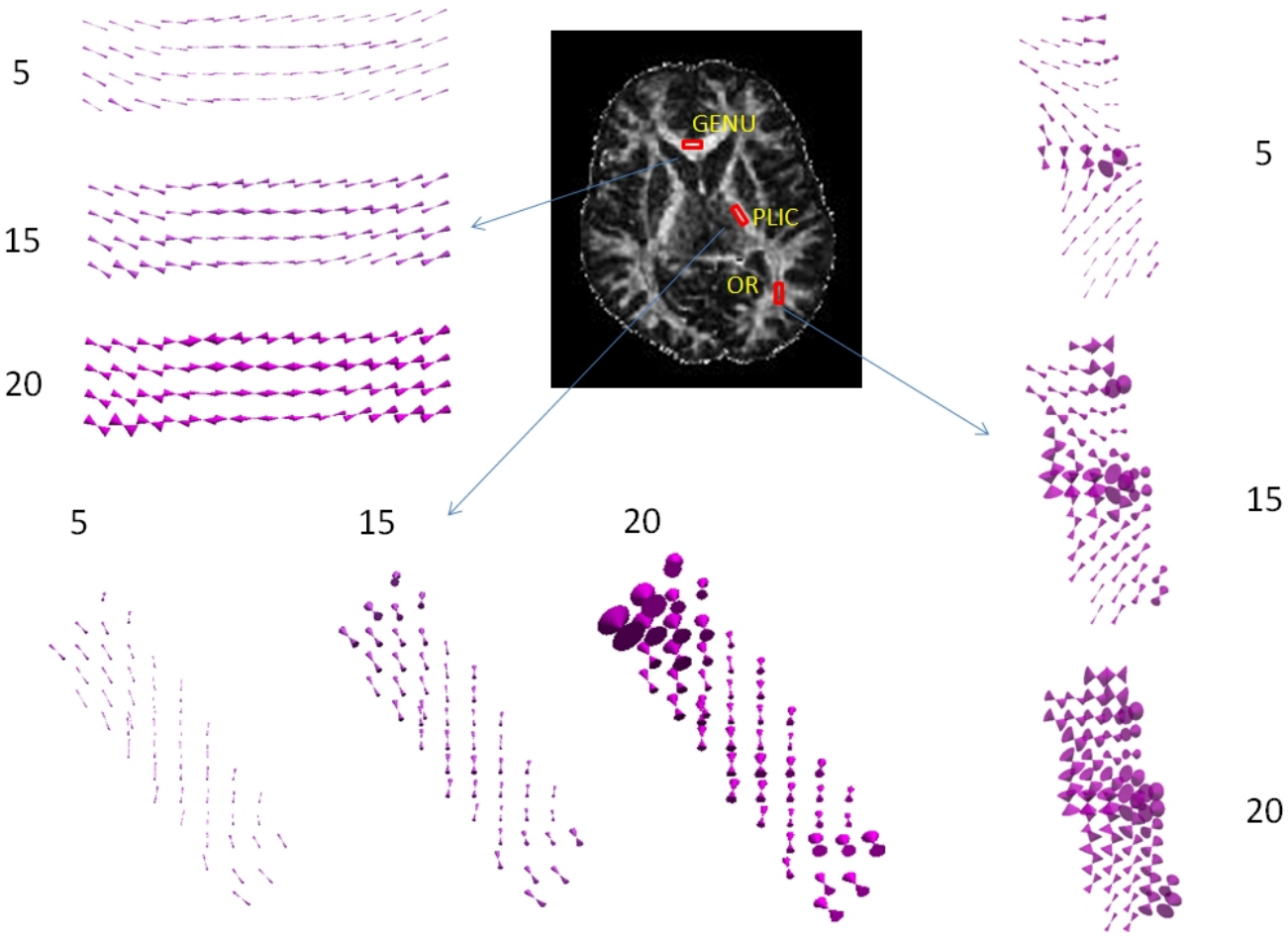

Figure 2.6: Cones of uncertainty for GENU, PLIC and OR with 5, 15 and 20 number of random rejections for the same subject as in Figure 2.1.

2.3.2 Clustered rejections

The results of clustered rejections showed the largest changes in FA and V1, comparable to the worst cases of random rejections. The comparison between random rejections and clustered rejections is presented in Figure 2.7, showing that the changes of both FA and V1 in the case of clustered rejections strongly deviated from the mean of random rejections, and even more from the reference.

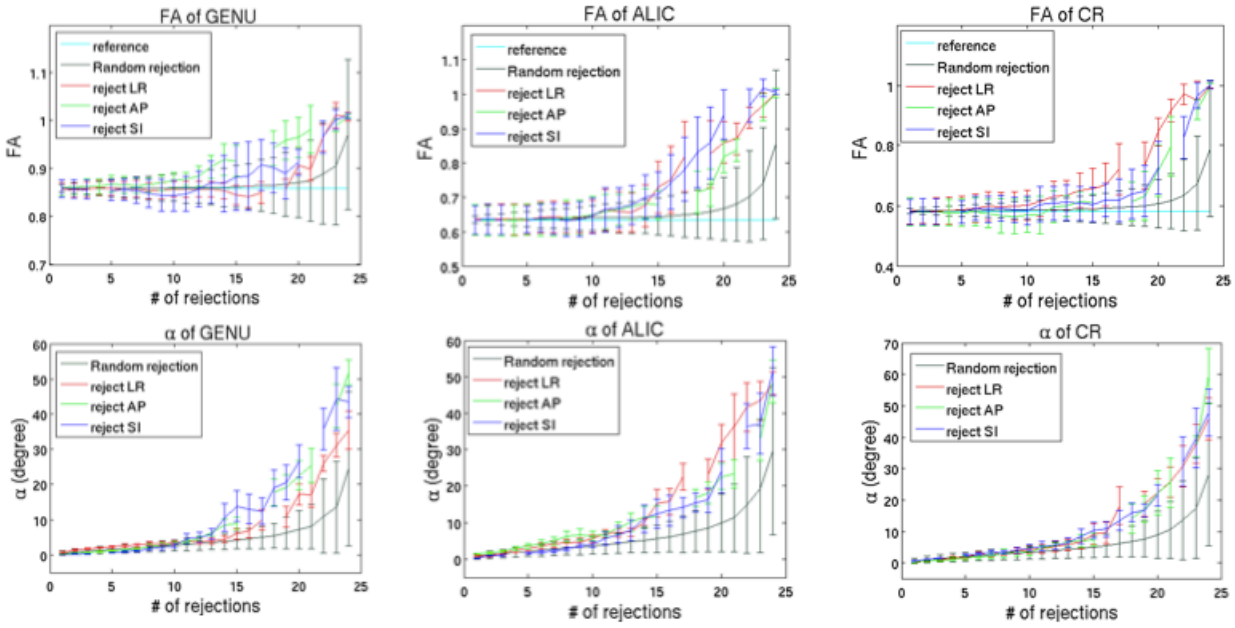

Figure 2.7: Comparison of FA and α between random rejections and clustered rejections for GENU, ALIC and CR.

The mean and standard deviation are calculated from 6 subjects for each ROI.

However, not all clustered rejections resulted in significant changes in AD and RD. As one can see from Figure 2.8, when the number of rejections was below 20, rejecting LR cluster did not cause a significant difference in AD and RD for GENU, though other clustered rejections still caused great overestimation of AD and RD for all the ROIs.

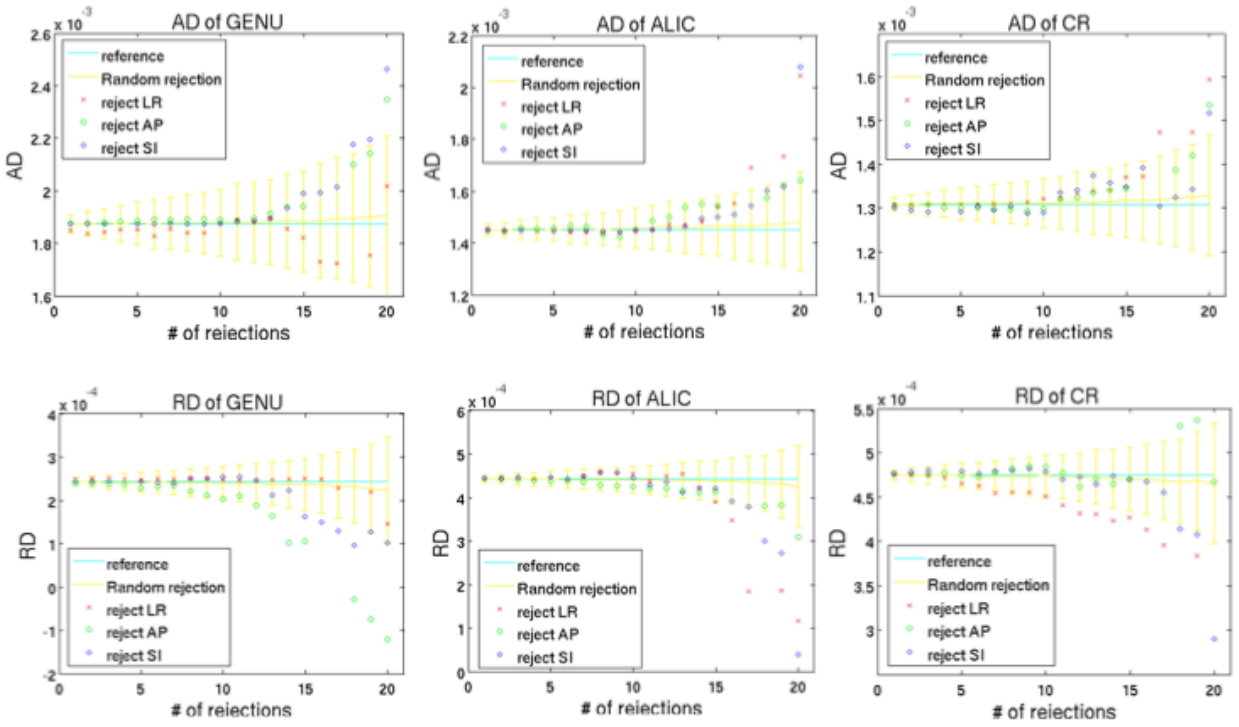

Figure 2.8: Comparison of AD and RD between random rejections and clustered rejections for GENU, ALIC and CR.

For each ROI, random rejections depict the mean and standard deviation from 6 subjects, and clustered rejections depict the mean from 6 subjects.

As it had been suggested that too many rejections might completely alter the tensor orientation (see Discussion) so that it becomes meaningless to evaluate the parameters (see Discussion), thus we only showed the results of φ and θ for up to 12 rejections near each of the axes for GENU, ALIC and CR in Figure 2.9. GENU and ALIC contain fibers predominantly oriented in LR and AP, respectively. Rejecting SI directions showed very small θ (less than 4 degree) but largest φ (Figure 2.9). Moreover, rejecting LR and AP showed about the same changes of θ and φ for GENU and ALIC. Although, all three clustered rejections had similar effect on the angle changes in CR (Figure 2.7), the changes of θ (from 0 to 25 degree) were much greater compared to GENU (from 0 to 5 degree) and ALIC (from 0 to 12 degree) (Figure 2.9), which means that

clustered rejections deviated the resultant fiber orientations away from z-axis more in SI-oriented fibers than other fibers.

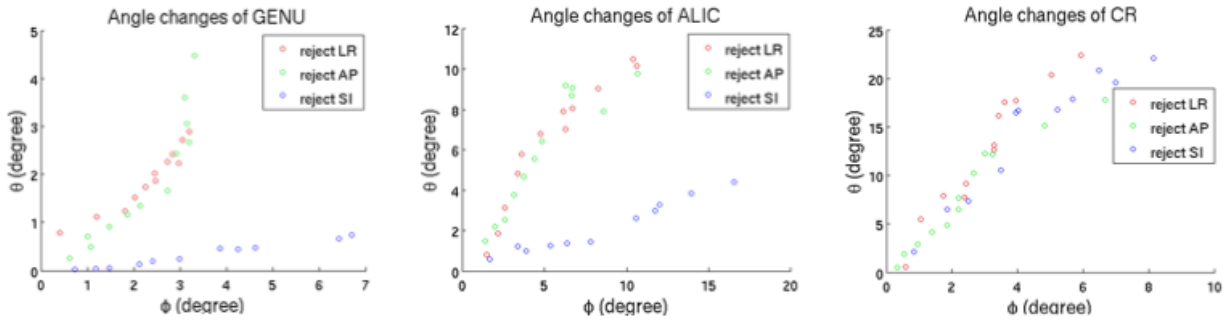

Figure 2.9: φ and θ changes for V1 of GENU, ALIC and CR from 1 to 12 clustered rejections near each axis.

The angle changes are calculated from the mean of the 6 subjects.

2.3.3 Comparison between protocols with different acquisition parameters

The comparison of changes in FA and V1 showed very similar results for different number of b0 volumes (Figure 2.10).

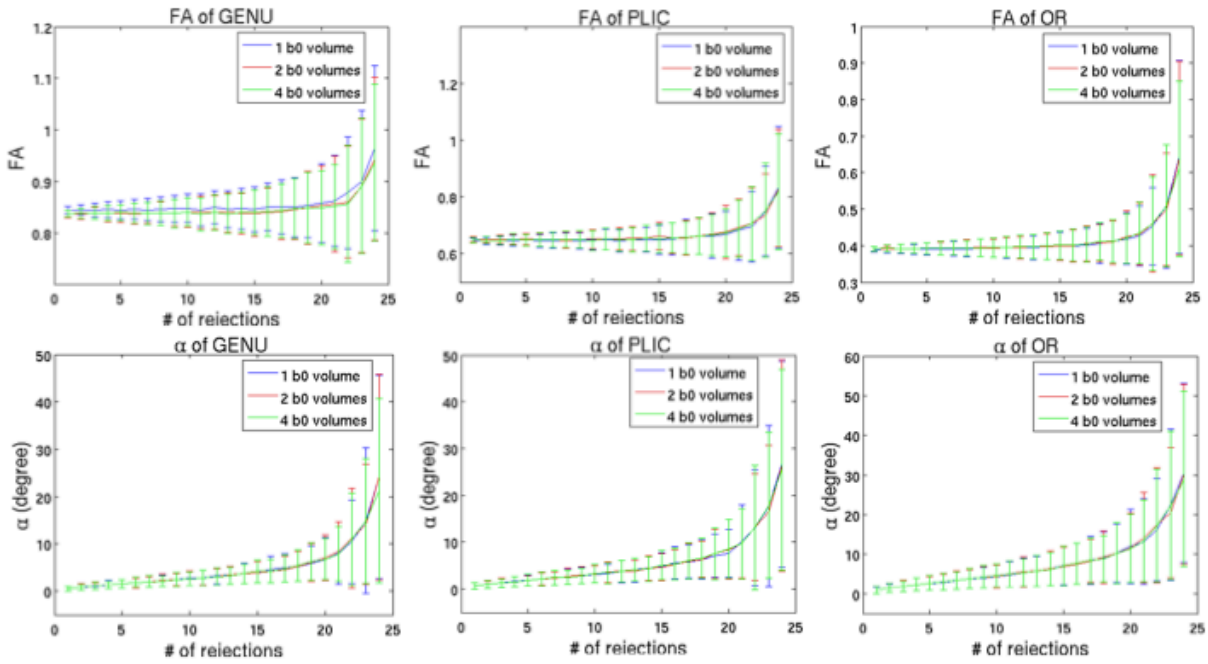

Figure 2.10: Comparison between one, two, and four b0 volumes with b=1000 s/mm^2 and 30 directions.

From Figure 2.11, we observed that the mean values of FA differed for different b-values, though the differences were small. Not much difference in standard deviations of FA was observed. Different b-values did not result in any significant difference in the change in V1.

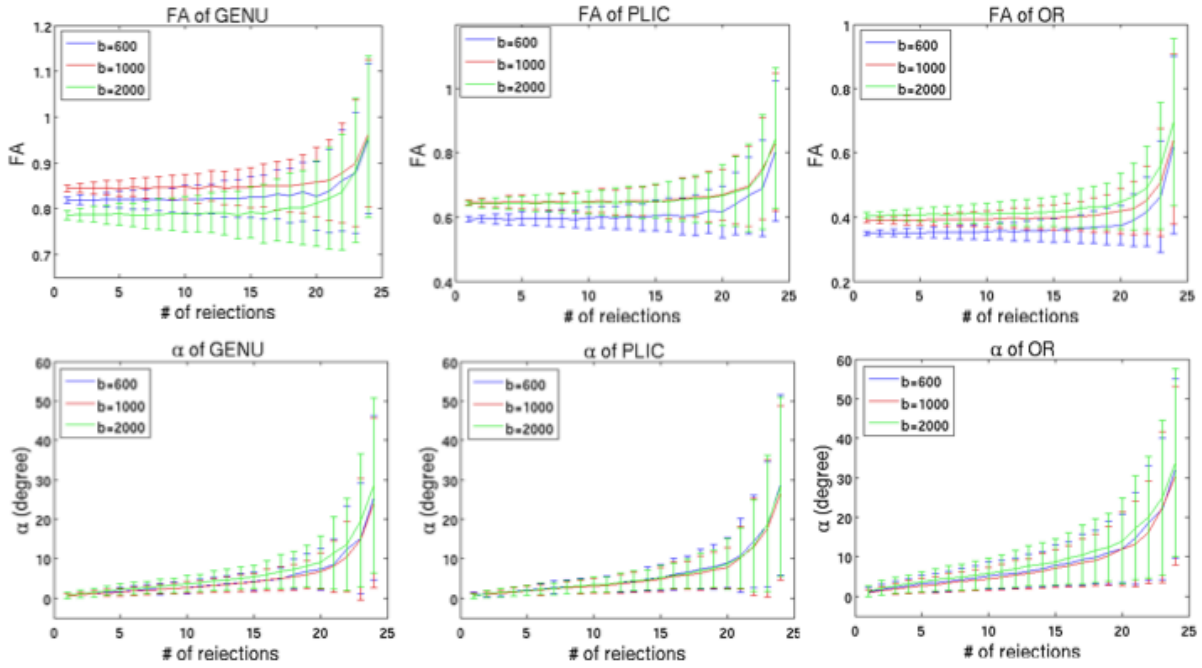

Figure 2.11: Comparison between b=600 s/mm^2, b=1000 s/mm^2 and b=2000 s/mm^2 with one b0 volume and 30 directions.

Figure 2.12 demonstrates that the total number of the acquired diffusion directions had a great influence on FA and V1. The more directions were acquired, the more consistent the values of FA and V1 would be, at the same number of rejections. The values of FA and V1 became very variable with the increasing number of rejections for the 15-direction case; on the other hand, very little change was observed in FA and V1 for the 55-direction case, even up to 24 rejections. If one looks at the changes in FA and V1 in terms of the number of the remaining directions instead of the number of the rejected directions, the results demonstrated consistency. Thus, for example, the results for the 15-directions case are systematically shifted 15 directions to the left compared to the 30-directions case (Figure 2.12).

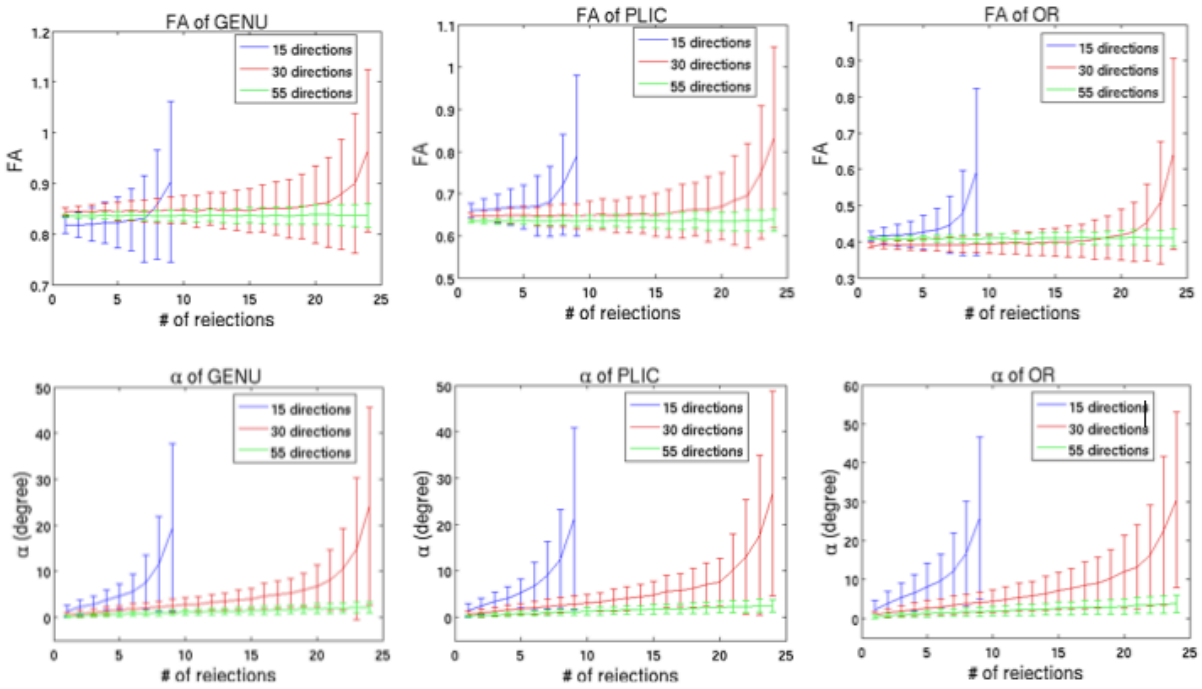

Figure 2.12: Comparison between 15 directions, 30 directions and 55 directions based on the equally distribution of points on a sphere by electrostatic repulsion with one b0 volume and b=1000 s/mm^2.

2.4 Discussion

It is important to understand the consequences of rejecting diffusion images for a more consistent analysis of tissue properties, such as water diffusivity, anisotropy and connectivity. In this chapter, we investigated the effects of discarding one or more diffusion directions on FA, MD, AD, RD and V1.

There are several approaches to rejection of diffusion data. One can review images directly and reject the volumes with corrupted images. This is manually intensive but results in accurate rejection. Another way is an automated rejection by voxel-wise analysis [52]. When a certain

number of pixels deviate from the corresponding mean pixel value for all diffusion directions by three standard deviations, the direction might be excluded from the tensor calculation. This threshold for the number of pixels deviating from the mean was set empirically, and depended upon the head size. Robust estimation of tensors by outlier rejection (RESTORE) has been proposed to reject the outliers during tensor estimation [53]. Instead of rejecting the entire volume, this technique only rejects the outliers among all diffusion directions in each voxel. Thus, each voxel may end up with different diffusion directions included in the tensor estimation.

Our results demonstrated that an accurate estimation of the mean diffusivity could be consistently obtained with relatively small number of diffusion remaining directions.

From the results of random rejections (Figure 2.4 & Figure 2.5), one could easily observe that the overestimations of FA, AD and RD got larger with increasing number of rejections. This is mainly due to the decreased signal-to-noise ratio (SNR) resulting from a smaller number of diffusion directions included in the tensor estimation. Therefore the mean FA, AD and RD was more deviated from the reference values and the uncertainties in FA, AD and RD (as seen from standard deviations) were greater with less remaining diffusion directions (Figure 2.4 & Figure 2.5). Since the mean value of MD remains consistent with the reference and the standard deviation was very small, one could possible infer that the change in MD was very insignificant, especially when the number of rejections was below 15.

The changes in FA, MD, AD and RD were also consistently correlated with each other. Generally increasing AD and decreasing RD with greater number of rejections (Figure 2.4 & Figure 2.5) would result an overall unchanged in MD. Furthermore, increasing AD and decreasing RD would cause the tensor to be more elongated, or more anisotropic, which corresponds to greater FA, and this coincided with our results as well.

In the case of uniform data reductions, changes in FA were only observed in low FA regions (Figure 2.3). This effect is not specific to the uniform rejection scheme and was also observed in lower FA regions for random rejections, as one can see from the comparison among GENU, PLIC and OR (Figure 2.4). Since the lower FA regions are more isotropic than the higher FA regions, the tensors can be depicted as more round-shaped in lower FA regions (the three eigenvalues are similar to each other). Any change in the estimation of a round-shaped tensor will result in a stronger influence on the orientation than of an oval-shaped tensor, because the eigenvectors of a round-shaped tensor can be easily interchanged [58].

In contradistinction to the uniform rejection, the results of the clustered rejection were strongly overestimated. This demonstrates that more uniformly distributed rejections lead to smaller overestimations of the tensor-derived parameters. Conversely, the closer they are to each other (clustered), the larger the overestimations. Based on the results of the clustered rejections, one could suggest that the angle changes in V1 depend on the orientation of the rejected diffusion directions with respect to the orientation of the underlying white matter fiber (Figure 2.9). This further demonstrates the importance of uniformly distributed diffusion directions to the accuracy of tensor estimation, which also confirms with previous reports [47, 59].

Among the general trend with strongly overestimated results for clustered rejections, an exemption one could observe from Figure 2.8 was that rejecting LR directions did not cause a significant change in AD and RD of GENU when the number of rejections is less than 20. As GENU is oriented in LR, one might interpret it as follows: rejecting directions that were parallel to the underlying fibers in the ROI would result little change in AD and RD. However, our results of clustered rejections for ALIC and CR did not show the same effect, except that rejecting an SI cluster (which was parallel to CR) had less effect on AD of CR than other clusters. This might be due to the fact that ALIC and CR had lower FA than GENU, and SNR plays greater influence on lower FA regions than higher ones, which makes changes in the former less predictable or stable. In addition, the alignment of the underlying fibers can be more variable in those regions. Applying gradient parallel to the orientation of highly anisotropic regions would result very little alteration in the overall direction of water molecules' flow. This explains why rejecting directions that were parallel to the underlying fibers in GENU would result little change in AD and RD, but it was not the case for other less anisotropic regions.

Whereas the scalar values of FA are often regarded as a marker for white matter integrity, V1 is usually used for tractography. Any change in those values would alter the results of investigation of the brain characteristics. It would complicate the interpretation of changes in FA values since they may increase or decrease unpredictably after diffusion direction rejection. Any shift in the orientation of V1 may completely redirect the streamline pathways, which would make the final result of tractography meaningless. Hence, when diffusion rejections are required before tensor

estimation, it is important to access the number of rejections and where on the sphere the rejected diffusion directions were located, in order to account for the accuracy of the evaluation.

One thing noticeable in Figure 2.4 is that for uniform rejections, very little change in FA, AD and RD was observed, even with only 6 remaining directions in low FA region. Therefore, it is recommended to access the locations of the corrupted directions before proceeding to tensor estimation. If they are distributed relatively uniformly, rejecting those directions may not increase uncertainty in parameter estimation; if a few directions are grouped in one location, one may consider rejecting more directions to make the remaining ones more uniform, thus maintaining the accuracy of the tensor-derived parameters. However, reducing the number of diffusion directions will decrease SNR in the reconstructed diffusion tensor images, and consequently, affect the accuracy of the parameters. Such trade-off should be considered depending on SNR of the acquired diffusion weighted images. From our results with reasonable clinical scan parameters, in case of evaluating scalar values such as FA and diffusivities, rejecting until only six uniformly distributed directions remaining still provided relatively valid results. As one can see from Figure 2.4, if the number of rejections is less than 10, it is not necessary to reject more directions to achieve six uniform directions. While the number of rejections is more than 10, unless the remaining directions are approximately uniform, we suggest rejecting until six uniform directions remaining in order to make a more precise measurement. However, in the extreme case that a few directions are close to each other so that it is impossible to achieve uniform distribution, one may consider to exclude the whole data set for further analysis since the results from such highly corrupted data will be quite inaccurate.

We have also investigated the influence of diffusion acquisition parameters on the effects of diffusion rejections. The number of b0 volumes did not cause any significant difference in the changes of FA and V1 (Figure 2.10). Thus, in order to shorten the total scan time to avoid any additional motion, one b0 volume is suggested in clinical settings for patients with uncontrolled motions (unless additional b0 volumes are deliberately used for the purposes of motion correction). Higher b-values reduce the SNR and we expected the changes of FA and V1 to be more sensitive to rejections. Our results showed that different b-values caused differences in the mean FA, but not in the mean V1 changes (Figure 2.11). Whereas the accuracy of FA depended on the b-value, the standard deviations of FA were not significantly different, which indicates that the precision of FA after rejection was similar for different b-values. Figure 2.12 demonstrates that the accuracy and precision of FA and V1 are dependent on the number of the remaining diffusion directions, which is the difference between the number of the acquired and rejected directions. This is consistent with the previously proposed theoretical framework [60], as the more diffusion directions remain, the higher is the SNR (proportional to the square root of the number of diffusion directions). However, if more directions are initially acquired, there are more possibilities to reject corrupted directions and still maintain the overall equal distribution of the remaining directions, which would lead to more stable estimations of the tensor-derived parameters. On the other hand, since more motion is expected if the subject is in the scanner for a longer time, it might not very efficient to acquired more than 30 diffusion weighted images and then reject more directions afterwards. To summarize our results, the changes of tensor-derived parameters were predominantly defined by the number of remaining diffusion directions and by their location, both, with respect to a uniform distribution on a unit sphere and the underlying tissue orientation.

In this work, we only evaluated the effects of rejecting diffusion directions on the second-order diffusions tensor, which is the most commonly used simplified model in diffusion imaging. DTI assumes Gaussian diffusion of water, which is not a realistic assumption in human tissues. It only represents the averaged result per voxel, and any intra-voxel information cannot be retrieved. Other techniques such as q-ball imaging [61], spherical deconvolution [62], generalized diffusion tensor [63], and diffusion spectrum imaging [64], can potentially resolve sub-voxel information such as crossing fibers. New parameters have been proposed along with these higher-order models to describe anisotropy and fiber orientation, such as fractional multi fiber index [65], and fiber orientation distribution function [66, 67], respectively. Effects of rejecting diffusion directions on these parameters might be different from the second-order tensor parameters, especially in low FA regions. Low FA regions can result either from an isotropic underlying microstructure or from numerous crossing fibers. Since DTI cannot differentiate these two types of low FA regions, rejecting diffusion directions will show similar consequences in both cases. However, if higher-order models are used to reveal more sophisticated tensor glyphs, rejecting diffusion directions might only affect some of the components but not alter the overall anisotropy or directionality. Thus, if any other methods are applied beyond DTI, a more complex analysis should be considered to evaluate the effects of rejecting diffusion directions.

Chapter 3 : Pyruvate to lactate metabolic changes during neurodevelopment measured dynamically using hyperpolarized ^{13}C imaging in juvenile murine brain

3.1 Introduction

Most of MRI studies of normal brain maturation use conventional methods such as T1- and T2-weighted and DTI to assess morphological and microstructural changes, and subsequently, their inference on anatomical growth and functional segregation. These methods have been widely applied for over a decade in brain development studies, but little has been shown on dynamic metabolic changes during development. From this chapter onwards, we are going to demonstrate the aforementioned technique of DNP (Chapter 1.5) as an emerging method to study metabolic pathway dynamically *in vivo* during normal and hypoxic-ischemic injured brain development.

In this chapter, we applied DNP using ^{13}C-1 labeled pyruvate to investigate the changes in pyruvate to lactate conversion over the course of mouse brain maturation, and combined this with T2-weighted MRI to obtain voxel-based volume changes in relation to maturation in mouse brain.

3.2 Methods

3.2.1 Experimental procedure

Eight normal mice were scanned starting on postnatal day 18 and repeated every 10 days. A few time points were delayed due to technical issues. Mice were anesthetized with 1.5% isoflurane and 1 L/min oxygen during scans. A catheter was inserted into the tail vein for proceeding injection of hyperpolarized pyruvate. During the experiment, 0.3mL of mixed saline and heparin was injected into the mouse every 15 minutes to prevent blood clot. All experiments were conducted on a vertical 14.1T (Agilent) 600WB NMR spectrometer with 55mm 1000mT/m gradients. A 38mm diameter ^{1}H and ^{13}C dual-tuned coil was used, where ^{1}H frequency was for main field shimming and T2-weighted anatomical imaging, and ^{13}C coil was used for hyperpolarized ^{13}C spectroscopic imaging.

48μL of C1 labeled ^{13}C pyruvate was polarized using an Oxford Hypersense^{TM} DNP instrument at 3.5T under 1.5K for an hour. Before injecting into the mouse, the hyperpolarized ^{13}C-1 pyruvate was mixed with 4.5mL of NaOH buffer, which resulted a 160mM pyruvate solution with pH~7.5. The dissolution mixture was then injected into the tail vein through a catheter over a span of 12 seconds. The total volume injected was 300 μL with 150 μL into the mouse and 150 μL left in the catheter.

3.2.2 Data acquisition

^{13}C spectroscopic imaging. Data were acquired on a 24mm×24mm×5mm slice centered on the brain, with 2D chemical-shift imaging. Center-out k-space trajectory was used with 7x7 phase encoding (zero-filled to 8x8). 128 spectral points were acquired with 2500 Hz bandwidth. The acquisition was started simultaneously with the pyruvate injection and repeated every 4s (3s acquisition time with 1s delay between each repetition) for a total of 60s (or 15 repetitions) with constant flip angle of 10°.

T2-weighted anatomical imaging. A 2D fast spin echo (FSE) sequence was applied for anatomical imaging with TR/TE=1.3s/12ms, and 8 echo train length with 12 ms echo spacing. The field of view was 30mmx30mm with 256 frequency and phase encodes, resulting in a 0.12mmx0.12mm in-plane resolution. The slice thickness was 1mm, and 10 slices were acquired without gap, covering most of the brain. The total scan time was 11 minutes.

3.2.3 Data processing

^{13}C spectroscopic imaging. A 5Hz Lorentzian apodization was applied to each free-induction decay before Fourier transforming the data. After Fourier transformation, each voxel could be referred to a 15-time-point spectrum (Figure 3.1a). The peak height of pyruvate and lactate at each time point for each voxel were measured. Then we chose the six voxels matching the location from the T2-weighted anatomical image (Figure 3.1b), and averaged signal intensities among the six voxels for pyruvate and lactate separately. The pyruvate signal intensity depended

on the polarization level, which varied between experiments, and consequently, the lactate signal intensity was affected, due to a linear relationship between pyruvate and lactate [68]. In order to compare lactate signal at different ages, we normalized the data by dividing lactate signal by the total carbon signal in the slab at each time point. We recorded the 5 highest intensities of normalized lactate in each scan for every mouse.

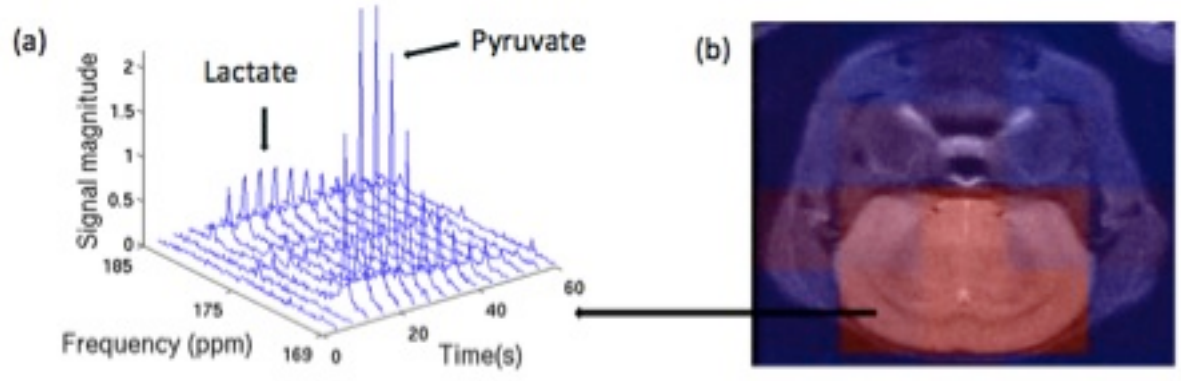

Figure 3.1: Dynamic spectra of pyruvate metabolic pathway and its overlay on T2-weighted image of a mouse brain.

The 15-time-point dynamic spectrum (a) is depicted for a voxel. The six voxels matched with the brain (b) were chosen for ^{13}C analysis.

T2-weighted anatomical imaging. To investigate brain volume changes through maturation, we used linear co-registration between the brains of two consecutive scans (i.e., 1st to 2nd, 2nd to 3rd, and so on) for each individual mouse (Figure 3.2). To achieve this, we first manually masked the brain mask of the 1st scan from non-brain tissues and parts including other organs of the head, the feet and water tubes running under the mouse to keep its body temperature. Then we linearly registered the 2nd scan to the 1st brain mask. This process subsequently created a brain mask of the 2nd scan by transforming the mask of the 1st scan. In the same manner, we registered the 3rd scan to the 2nd scan to create the brain mask of the 3rd scan, and so on. Multiplication of the three

scaling parameters (in x, y, and z-axes) in the transformation matrix measured brain volume changes.

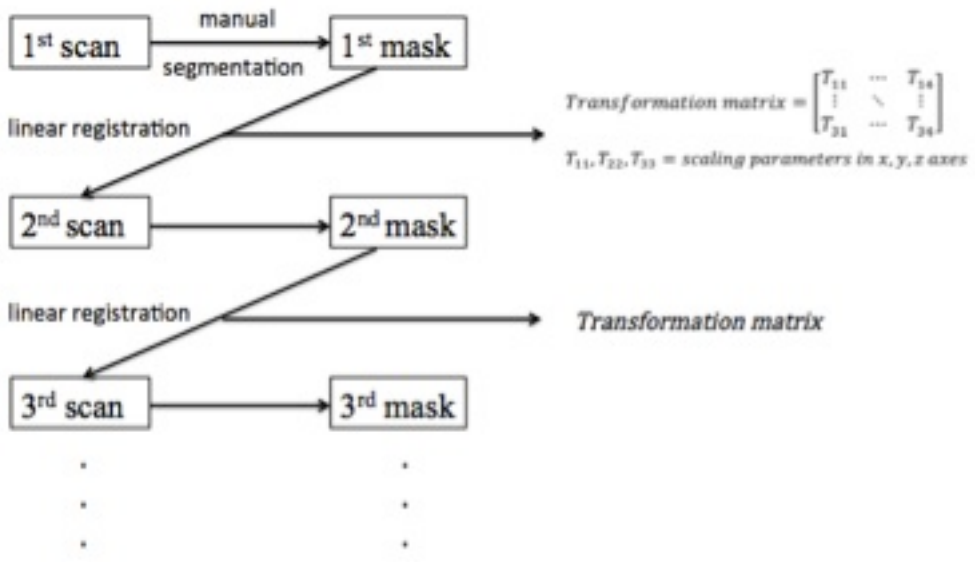

Figure 3.2: Linear registration scheme between subsequent scans within each subject.

The multiplication of the 3 scaling parameters T_1, T_2 and T_3 from the resultant transformation matrix was used for volume change calculation.

3.2.4 Kinetic modeling

The hyperpolarized ^{13}C-pyruvate was converted into lactate rapidly in the brain, allowing us to investigate real-time change of this metabolic process. To quantify the rate of this change, we applied the kinetic model from Zierhut et al [69] to fit the pyruvate and lactate signal over time. We averaged the peak height of pyruvate and lactate separately from the six voxels in the brain for each time point, and then we could obtain a curve of signal build up and decay for pyruvate and lactate individually (Figure 3.3).

The model was first fit into the pyruvate curve:

$$M_{pyr}(t) = \begin{cases} \frac{rate_{inj}}{k_{pyr}}\left(1 - e^{-k_{pyr}(t-t_{arrival})}\right), & t_{arrival} \le t < t_{end} \\ M_{pyr}(t_{end})e^{-k_{pyr}(t-t_{end})}, & t \ge t_{end} \end{cases}$$

where $M_{pyr}(t)$ is the pyruvate signal at time t, and t_{end} is the time when pyruvate signal reaches the highest value. The parameters estimated from the fitting are: $rate_{inj}$, the rate of pyruvate injection; k_{pyr}, the rate of pyruvate signal decay, which is $\frac{1}{T_{1\,pyr}}$, where $T_{1\,pyr}$ is the T1 constant of hyperpolarized pyruvate at 14T field strength; and $t_{arrival}$, the time when pyruvate arrives in the brain. Then we used these estimated parameters to fit into the lactate curve:

$$M_{lac}(t)$$

$$= \begin{cases} \frac{k_{pl}rate_{inj}}{k_{pyr} - k_{lac}}\left(\frac{1 - e^{-k_{lac}(t-t_{arrival})}}{k_{lac}}\right) - \frac{1 - e^{-k_{pyr}(t-t_{arrival})}}{k_{pyr}}, & t_{arrival} \le t < t_{end} \\ \frac{M_{pyr}(t_{end})k_{pl}}{k_{pyr} - k_{lac}}\left(e^{-k_{lac}(t-t_{end})} - e^{-k_{pyr}(t-t_{end})}\right) + M_{lac}(t_{end})e^{-k_{lac}(t-t_{end})}, & t \ge t_{end} \end{cases}$$

where $M_{lac}(t)$ is the lactate signal at time t. We could estimate k_{lac}, the rate of lactate decay, and k_{pl}, the conversion rate from pyruvate to lactate from this fitted model. The conversion rate, k_{pl}, is another parameter besides normalized lactate level to imply metabolic rate in maturation.

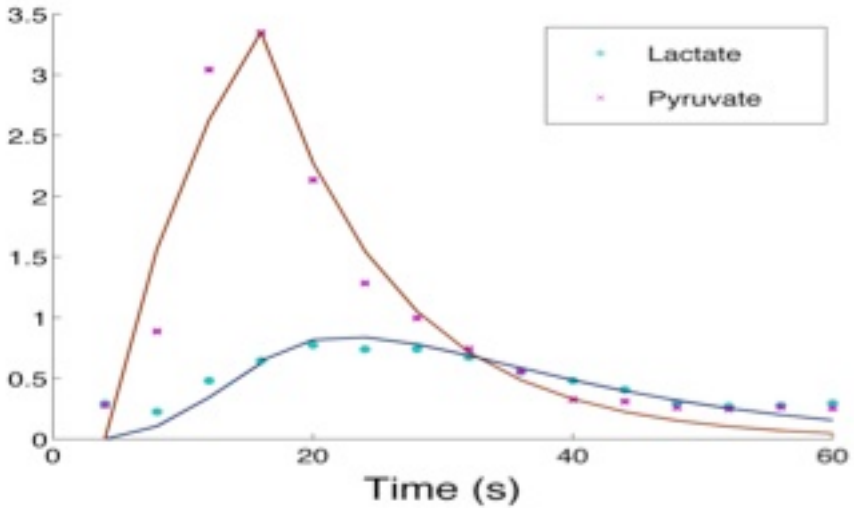

Figure 3.3: Dynamic data of pyruvate and lactate and kinetic model fitting.

Dynamic data of the averaged peak height of pyruvate (x) and lactate (*) from six voxels in the brain. Kinetic models were fitted to pyruvate (−) and lactate (−).

3.2.5 Statistical analysis

To examine the association between age and the lactate level, pyruvate to lactate conversion rate or brain volume, we used a mixed effect linear model on the 5 highest intensities of normalized lactate, the pyruvate to lactate conversion rate, and the volume scaling separately using SurfStat (http://www.math.mcgill.ca/keith/surfstat/) [70]. This model permitted multiple measurements per subject while controlling for between-subject variation, thus increasing statistical power. We tested linear and nonlinear polynomial fitting.

In addition, we recorded body weight for each experiment, because body weight can also be an empirical indicator of maturation besides brain volume. The body weight was measured before experiment since the injection of hyperpolarized pyruvate would change the total body weight.

3.3 Results

By plotting the normalized lactate level versus age for each individual mouse, we observed significant decrease in normalized lactate signal with increasing age using a mixed effect model on the normalized lactate intensities (t=-3.84; p=0.001) (Figure 3.4).

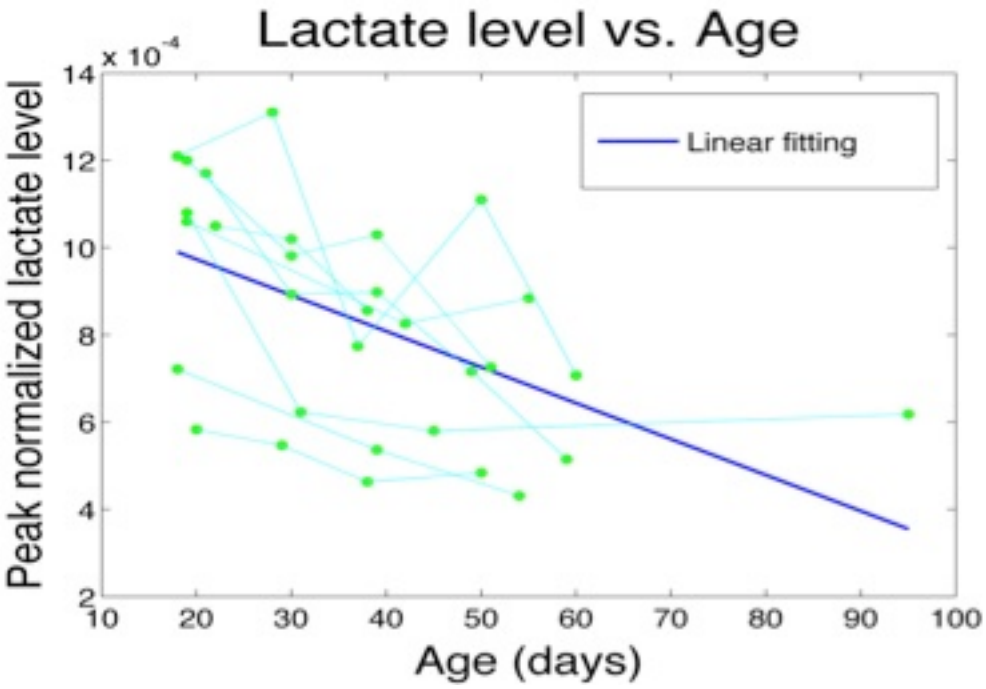

Figure 3.4: Linear fitting of the mixed effect model to the peak normalized lactate level against age.

We plotted the estimated pyruvate to lactate conversion rate, k_{pl}, against age for each individual mouse (Figure 3.5). Linear fitting resulted in the highest significance when we evaluated the mixed effect model on k_{pl}. Similar to lactate level, k_{pl} also decreased with increasing age (t=-2.11; p=0.044).

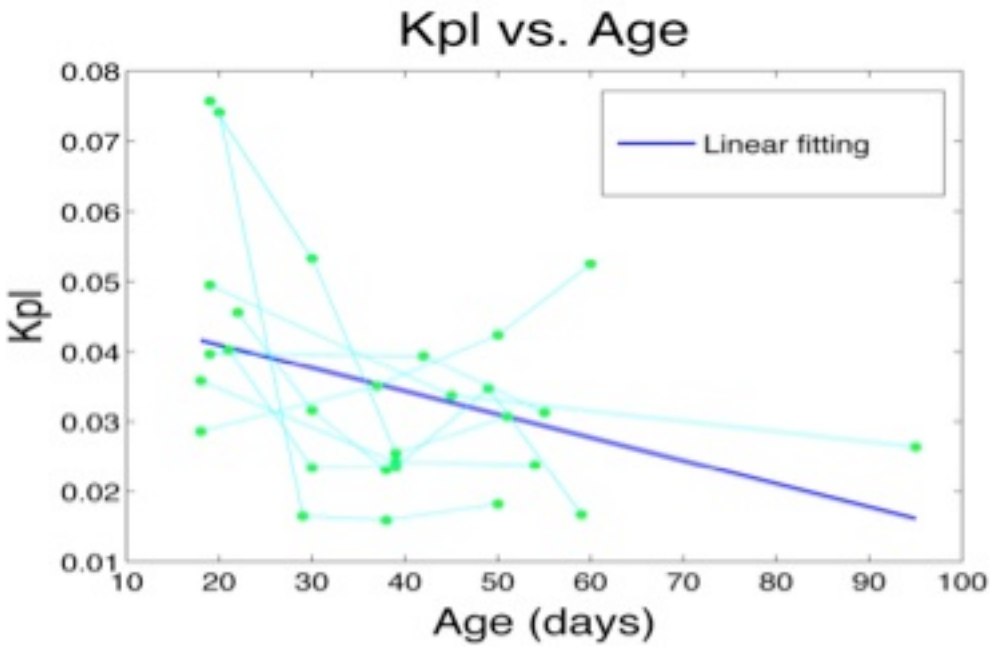

Figure 3.5: Linear fitting of the mixed effect model to the pyruvate to lactate conversion rate, K_{pl}, against age.

Analysis of linear regression on brain volume changes (i.e., multiplication of 3D scaling factors) showed no relationship between volume and age ($t=0.82$; $p>0.4$). However, total body weight increased with age (Figure 3.6) even though the global brain volume did not change after P18. Body weight almost doubled from P18 to P30, and the rate of weight growth slowed down after P30 (Figure 3.6). It follows an exponential growth ($t=5.07$; $p=0.000025$).

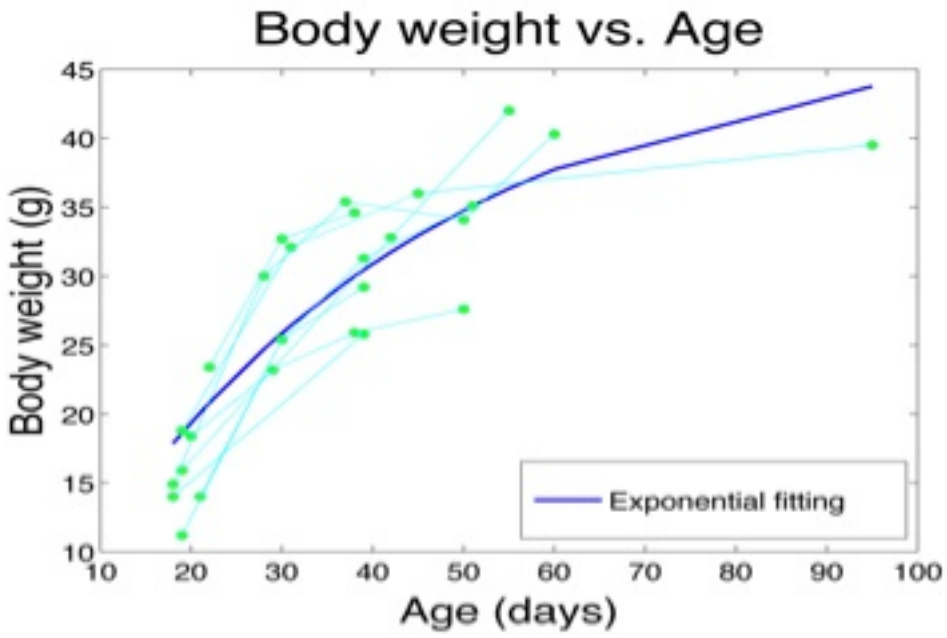

Figure 3.6: The plot of body weight against age for each individual subject, with general exponential fitting.

3.4 Discussion

Our ^{13}C metabolic imaging results demonstrated that pyruvate to lactate conversion was higher at younger age, and decreased linearly with increasing age. At a young age, brain and body consume more energy for brain development and body growth. Lactate can be used as an energy fuel for brain activation [71-79], and thus, its production is higher at younger age to support neuronal and other functional needs. It has been shown in cultured cells that both neurons and astrocytes utilize lactate as a source of energy and a precursor of lipids [80] and these results further were supported by ^{13}C MR studies [24-26]. Moreover, the utilization of lactate by oligodendrocytes is three times higher than that by neurons and astrocytes [81]. The combination of these published findings suggests that lactate is greatly used for lipogenesis during myelin synthesis and may support a further explanation that long-lasting microstructural changes can

occur in relation to brain maturation even at the stage where macroscopic volume growth stops, which is demonstrated in our results.

In this work, the analysis of total body weight showed that the mouse continued to grow after P18 and the rate of growth slowed down after P30. Our volumetric analysis based on T2-weighted images, on the other hand, did not show a significant change of overall brain volume after P18. This is consistent with findings of a previous high-resolution ex vivo T2-weighted MRI study that global and local volumes of mouse brain remained constant in size after P18 [82]. This may imply that the mouse brain reaches its maximum volume earlier than the whole body does. Another study has, however, shown that the lipid composition of myelin and microsomal fractions of mouse brain appeared to greatly increase from P14 to P24 and continued growing until P47 [83]. Protein composition of mouse brain myelin also continues to increase until P300, with the highest rate of increase between P20-P25 and decreasing rate of increase afterwards [84]. Although there is cross-subject variation in determining maturation stage [85], these published findings together with our result suggest that the microstructural growth of the mouse brain may continue even after adolescence although its total volume did not change.

In addition to total lactate level, pyruvate to lactate conversion rate is another parameter to measure the degree of metabolic change during brain development. The higher the conversion rate, the faster the metabolism takes place, and consequently, more lactate is produced within a limited amount of time. The maximum reaction rate of pyruvate, V_{max}, is a more accurate and commonly recognized parameter to measure the rate of metabolism than the pyruvate to lactate conversion rate. If we can vary the concentration of pyruvate, we will get different k_{pl} from

different pyruvate concentration. Based on the different conversion rates and pyruvate concentrations, we can apply Michaelis-Menten kinetics model to estimate the maximum reaction rate of pyruvate, V_{max}: $K_{pl} = \frac{V_{max}[pyr]}{K_m+[pyr]}$, where $[pyr]$ is the concentration of pyruvate and K_m is the Michaelis constant which refers to the concentration of pyruvate at half V_{max}. However, the main obstacle of achieving this is that the mouse is too small to receive multiple shots of pyruvate within one experiment at young age. This can be improved by reducing the dead volume of saline and heparin in the catheter. We are working on a technical solution to divert the dead volume before injection through a custom-built cog system for this purpose. With minimal dead volume, we will be able to perform multiple experiments at a younger age when brain volume is still growing and access the correlation between metabolic rate and brain growth.

A notable strength of the current work lies in the longitudinal in vivo MRI imaging, yielding multiple measurements per individual. Our analysis was based on the global measurement of brain metabolism and volume. Although regional metabolism may be important to understand pattern of brain development, low resolution in the hyperpolarized ^{13}C acquisitions is a major technical challenge, limiting the ability for regional analyses. The hyperpolarized substrate returns to polarization at thermal equilibrium very quickly after taken out of the polarizer. Moreover, T1 of hyperpolarized substrate is shorter at the higher field strength of our 14T animal scanner as compared to lower fields such as 1.5T or 3T. Nevertheless, we achieved a very important advance in obtaining a dynamic spectroscopic image, where the acquisition was repeated every 4 seconds for a total of 60 seconds. The image spatial resolution of 3mm x 3mm was the highest we could achieve within 4 seconds by current technique. There is a tradeoff between temporal resolution and spatial resolution. With future improvement in the MRI pulse

sequence, we will be able to reach comparable ^{13}C spectroscopic image resolution with anatomical image resolution, enabling the analysis of brain local changes in metabolism and volume from a young age to P18 and later ages.

Our work demonstrates the effectiveness of hyperpolarized ^{13}C MRI to examine the dynamic metabolic changes of pyruvate to lactate conversion during brain maturation, suggesting other substrates can be used in the same manner to explore dynamic changes of other metabolic pathways. In our kinetic modeling, we neglected the oxidation from lactate to pyruvate by assuming its rate was negligible. Sometimes it is important to consider the lactate to pyruvate conversion rate, especially at very young age or with brain abnormalities such as hypoxia or hypoglycemia, in which lactate is utilized as substitute for glucose as energy source [86]. In the future, we plan to evaluate this by injecting hyperpolarized lactate into the mouse to estimate its conversion rate to pyruvate [87]. This can also be measured by using Metabolic Activity Decomposition Stimulated-echo Acquisition Mode (MAD-STEAM), which results a more robust and accurate modeling fitting with both conversion rates of pyruvate to lactate and lactate to pyruvate simultaneously [88, 89].

Overall, our longitudinal study using hyperpolarized ^{13}C MR spectroscopic imaging is the first to show in vivo dynamic changes of pyruvate to lactate conversion in the brain during normal brain maturation. The results from normal brain studies can serve as a baseline for future metabolic studies of injured developing brain such as hypoxic ischemic encephalopathy.

Chapter 4 : A metabolic study of hypoxic ischemia during mouse brain development using hyperpolarized ^{13}C

4.1 Introduction

As we introduced in Chapter 1, the majority of the MRI studies on HI animals were based on structural images, such as T1-weighted, T2-weighted and diffusion tensor imaging[10, 11, 90]. The hypothesis of energy failure has been broadly recognized as the main causal event of HI. Few MR studies have focused on the metabolic properties of HI using ^{1}H or ^{31}P spectroscopy[17-19]. Since we have demonstrated the feasibility of DNP to study metabolic changes during normal brain development in the previous chapter, we would like to further explore its application to study injury detection and progression during brain development. In this chapter, we applied DNP using ^{13}C-1 labeled pyruvate to investigate the changes in pyruvate to lactate conversion in HI mice across brain maturation *in vivo*, in order to establish a biomarker to detect HI at a very early stage and examine long-term metabolic exchanges during early brain development.

4.2 Methods

4.2.1 Hypoxic ischemia

P10 male and female CD1 mice were subjected to HI injury as previously described in the Rice-Vannucci model[91]. All procedures were approved by the Institutional Animal Care and Use Committee at the University of California San Francisco, in accordance with National Institutes of Health guidelines for the Care and Use of Laboratory Animals. Ligation of the left common carotid artery was performed as the follows: animals were anesthetized with 3.5% isoflurane. A midline neck incision was done in order to separate and permanently ligate the left common carotid artery via electrical coagulation. After the procedure pups were allowed 1 hour recovery with the dam. Global hypoxia was induced by placing the pups in chambers submerged in a water bath at 37°C into which a hypoxic atmosphere of 10% O2 / 90% N2 was introduced via inlet and outlet tubing controlled by a flow meter. After 60 minutes, pups were returned to the dam.

4.2.2 MRI experiment procedure

A total of 13 mice received HI. They were scanned at P10 (2-5 hours post HI), P17 and P31. Some dates were slightly shifted or missing due to scanner availability, technical issues or animal mortality. A total of 6 sham mice were also scanned at the same time points. These time points were chosen based on previous literature comparing human and murine brain maturation

stages, where P10 on mice is equivalent to human newborn, P17 on mice is equivalent to human adolescence, and P31 on mice is equivalent to human adult [6, 85].

Mice were anesthetized with 1.5% isoflurane and 1 L/min oxygen during scans. A catheter was inserted into the tail vein for proceeding injection of hyperpolarized pyruvate. During the experiment, 0.3mL of mixed saline and heparin was injected into the mouse every 15 minutes to prevent blood clots. All experiments were conducted on a vertical 14.1T (Agilent) 600WB NMR spectrometer with 55mm 1000mT/m gradients. A 38mm diameter ^{1}H and ^{13}C dual-tuned coil was used, where ^{1}H frequency was for main field shimming and T2-weighted anatomical imaging, and ^{13}C coil was used for hyperpolarized ^{13}C spectroscopic imaging.

48μL of C1 labeled ^{13}C pyruvate was polarized using an Oxford Hypersense^{TM} DNP instrument at 3.5T under 1.5K for an hour. Before injecting into the mouse, the hyperpolarized ^{13}C-1 pyruvate was mixed with 4.5mL of NaOH buffer, which resulted a 160mM pyruvate solution with pH~7.5. The dissolution mixture was then injected into the tail vein through a catheter over a span of 12 seconds. The total volume injected was 300 μL with 150 μL into the mouse and 150 μL left in the catheter.

4.2.3 Data acquisition

^{13}C spectroscopic imaging

Data were acquired on a 24mm×24mm×5mm slice centered on the brain, with 2D chemical-shift imaging. Center-out k-space trajectory was used with 8x8 phase encoding. 128 spectral points

were acquired with 2500 Hz bandwidth. From our previous hyperpolarized ^{13}C-1 pyruvate study on young mouse brains with the same experimental procedure in Chapter 3, pyruvate signal reaches its peak at around 12 to 16 seconds after the beginning of injection[92]. In this work, our acquisition was started 10 seconds after the pyruvate injection so the first time point coincides with when pyruvate is at its highest level. The acquisition was repeated every 5s (4s acquisition time with 1s delay between each repetition) for a total of 75s (or 15 repetitions) with constant flip angle of 10°.

T2-weighted anatomical imaging

A 2D fast spin echo (FSE) sequence was applied for anatomical imaging with TR/TE=1.3s/12ms, and 8 echo train length with 12 ms echo spacing. The field of view was 30mmx30mm with 256 frequency and phase encodes, resulting in a 0.12mmx0.12mm in-plane resolution. The slice thickness was 1mm, and 10 slices were acquired without gap, covering most of the brain. The total scan time was 11 minutes.

4.2.4 HI injury level score

We scored HI injury for each subject at P17 based on the T2-weighted images. Some subjects were missing scans at either P10 or P31 due to technical problems or animal expiration, but all subjects were scanned at P17. The injury at P10, which was depicted as hypointensity, extended almost to the entire ipsilateral hemisphere and had very little contrast or localization (Figure 1); therefore, it was difficult to score. The injury pattern at P31 was similar to the injury at P17.

Our scores were based on the 3 major injury areas: cortex, hippocampus and deep gray matter nuclei. Each area was scored rostral to caudal by progressively increasing numerical scores, which denoted either lack of injury, mild, moderate or severe damage. More specifically, each area was scored from 0-3 based on the following: 0 for no injury observed, 1 for mild focal hyperintensity, 2 for moderate larger hyperintensity that expanded to adjacent areas and 3 for cystic infarction. The total score was the sum of the 3 areas and ranged from 0 to 9.

4.2.5 Data processing and analysis

Voxel shift was performed on the 2D grid to locate one voxel on the left hemisphere and one voxel on the right hemisphere (Figure 4.1). The area under the peak of pyruvate and lactate was recorded for each of the 15 time points for the construction of the dynamic curves (Figure 4.2).

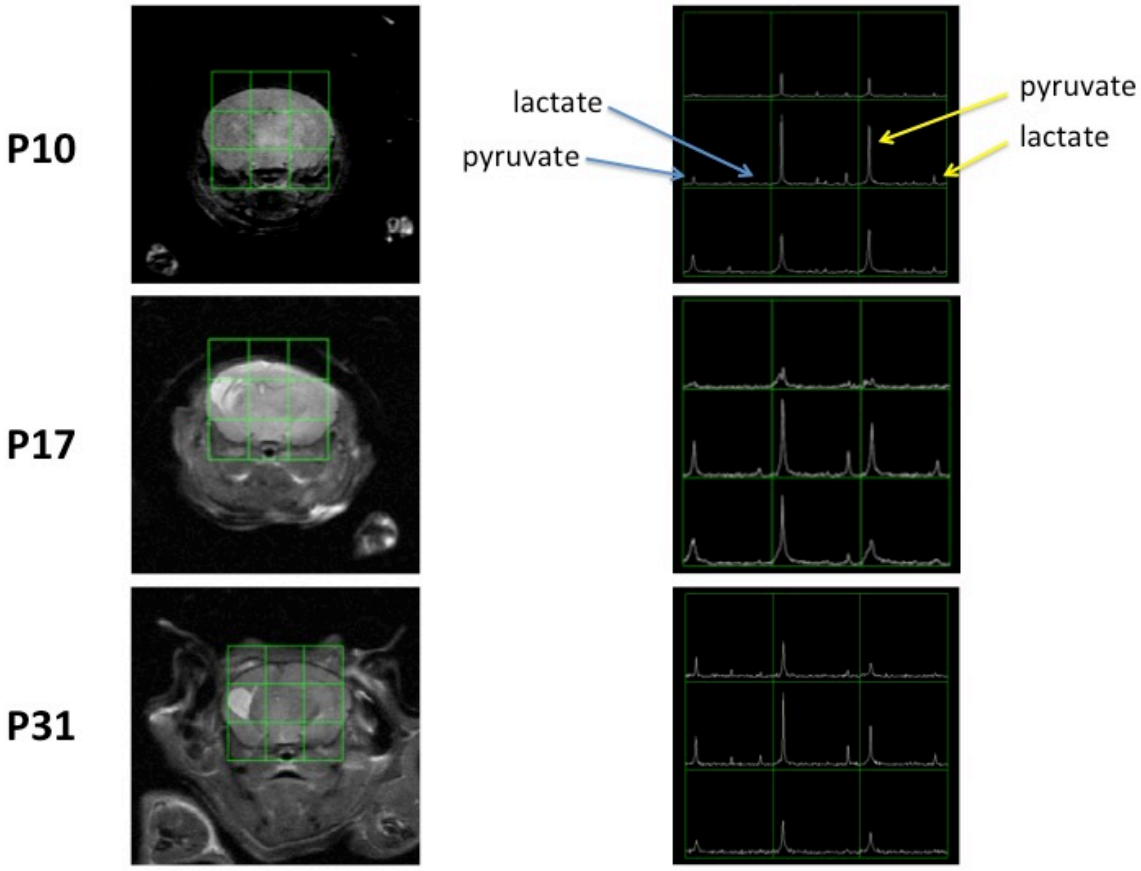

Figure 4.1: T2-weighted images overlaid with ^{13}C spectroscopic imaging with matching orientation at P10, P17 and P31 of a representative subject.

A slight hypointensity on the T2 weighted image and a significant reduction of pyruvate delivery in the spectra (blue arrowhead) can be observed few hours after HI at P10. The reduction persists throughout P17 and P31 but is less pronounced.

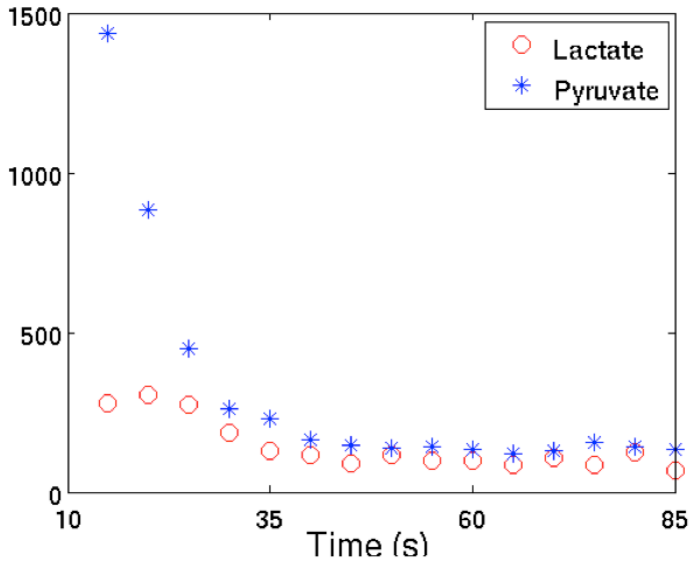

Figure 4.2: Pyruvate and lactate signals from the start of acquisition (10 second) to the end of acquisition (85 second) with 5-second interval.

Pyruvate signal depicts decay over time. Lactate signal has a slight build-up due to its conversion from pyruvate, and then decay.

Pyruvate delivery

The area under the pyruvate curve and the lactate curve were taken from a voxel on each of the hemispheres. The pyruvate signal intensity depended on the polarization level, which varied between experiments. In order to examine the effect of HI on pyruvate delivery into the brain, we compared the absolute pyruvate level between the two voxels chosen on each of the hemispheres. The pyruvate signal difference between two hemispheres was calculated as $Diff_{pyr} = \frac{Pyr_R - Pyr_L}{Pyr_R + Pyr_L}$, where Pyr_R is the area under the pyruvate curve for the right hemisphere and Pyr_L is calculated the same for the left hemisphere. We conducted student t-test for comparing $Diff_{pyr}$ between HI and Sham groups at each age.

Lactate to pyruvate ratio

The lactate signal intensity was affected by the amount of pyruvate delivery, due to a linear relationship between pyruvate and lactate[68]. Therefore, in order to observe changes of lactate conversion due to HI, we compare the lactate to pyruvate ratio between the two voxels chosen on each of the hemispheres. The difference in lactate to pyruvate ratio were calculated as $Diff_{ratio} = \frac{Ratio_R - Ratio_L}{Ratio_R + Ratio_L}$, where $Ratio_R$ is the ratio of the area under the lactate curve to the area under the pyruvate curve for the right hemisphere and $Ratio_L$ is calculated the same for the left hemisphere. We conducted student t-test for comparing $Diff_{ratio}$ between HI and Sham groups at each age.

Normalized lactate level in the brain

In our previous work on utilizing hyperpolarized ^{13}C-1 pyruvate on normal brain maturation in Chapter 3, we have found that the metabolic conversion from pyruvate to lactate slows down as the brain ages from P18 [92]. In this chapter, we have an additional time point at P10. This allows us to examine the metabolic conversion changes from newborn (P10) to adolescence (P17), and from adolescence to adult (P31). In order to have comparable results as the previous chapter, we use the same analysis by choosing the 3 voxels inside the brain and get the normalized lactate level, which is the average lactate signal in the 3 voxels divided by the total ^{13}C signal. We plotted the normalized lactate level against age for each subject to examine its longitudinal change.

We combined the HI subjects with mild injuries (scores = 0 to 2) with the sham operated subjects to quantify the longitudinal change of normalized lactate level in the brain. The reason of

combining these two groups will be explained in the Results. We conducted mixed effect linear model on normalized lactate level vs. age from P10 to P17 and from P17 to P31 separately using SurfStat, which permitted multiple measurements per subject while controlling for between-subject variation (http://www.math.mcgill.ca/keith/surfstat/) [70].

4.3 Results

Figure 4.1 shows the T2-weighted image and spectra after voxel shift for a representative HI subject at each age. One can observe a slight hypointensity on T2-weighted image and a significant reduction of pyruvate delivery in the spectra on the injured hemisphere a few hours after HI at P10. At P17 and P31, there is hyperintensity in the injured hemisphere. There is slightly less pyruvate delivery on the injured side than the contralateral side, but the difference is not obvious and needs further clarification.

HI injury level score

The HI injury level scores of all the subjects are shown in Table 4.1. Our subjects were either not, mildly injured (score = 0 to 2) or severely injured (score = 6 to 9).

Table 4.1: HI injury scores for each subject at P17

Mouse #	Cortex	Hippocampus	Deep gray	Total
1	3	3	0	6
2	0	0	0	0
3	0	2	0	2
4	3	3	1	7
5	3	2	2	7
6	3	2	2	7
7	3	3	3	9
8	0	1	0	1
9	0	0	0	0
10	0	0	0	0
11	3	3	3	9
12	3	2	1	6
13	3	3	3	9

Pyruvate delivery

Figure 4.3(a) shows the plot of $Diff_{pyr}$ against age for each subject. All HI subjects have positive values of $Diff_{pyr}$ at P10, which can be interpreted as less pyruvate delivered to the left hemisphere (ipsilateral) than the right hemisphere (contralateral). The difference between the two hemispheres shrinks at P17 as $Diff_{pyr}$ values approach zero. There is almost no difference between the two hemispheres at P31 since $Diff_{pyr}$ values are nearly nullified. However, no differences are observed in the Sham group, as all subjects have all $Diff_{pyr}$ values around zero

at each age. Figure 4.3(b) shows the Student t-test results between HI and sham groups at each age, with $p<0.01$ at P10, $p<0.05$ at P17 and no statistical significance at P31.

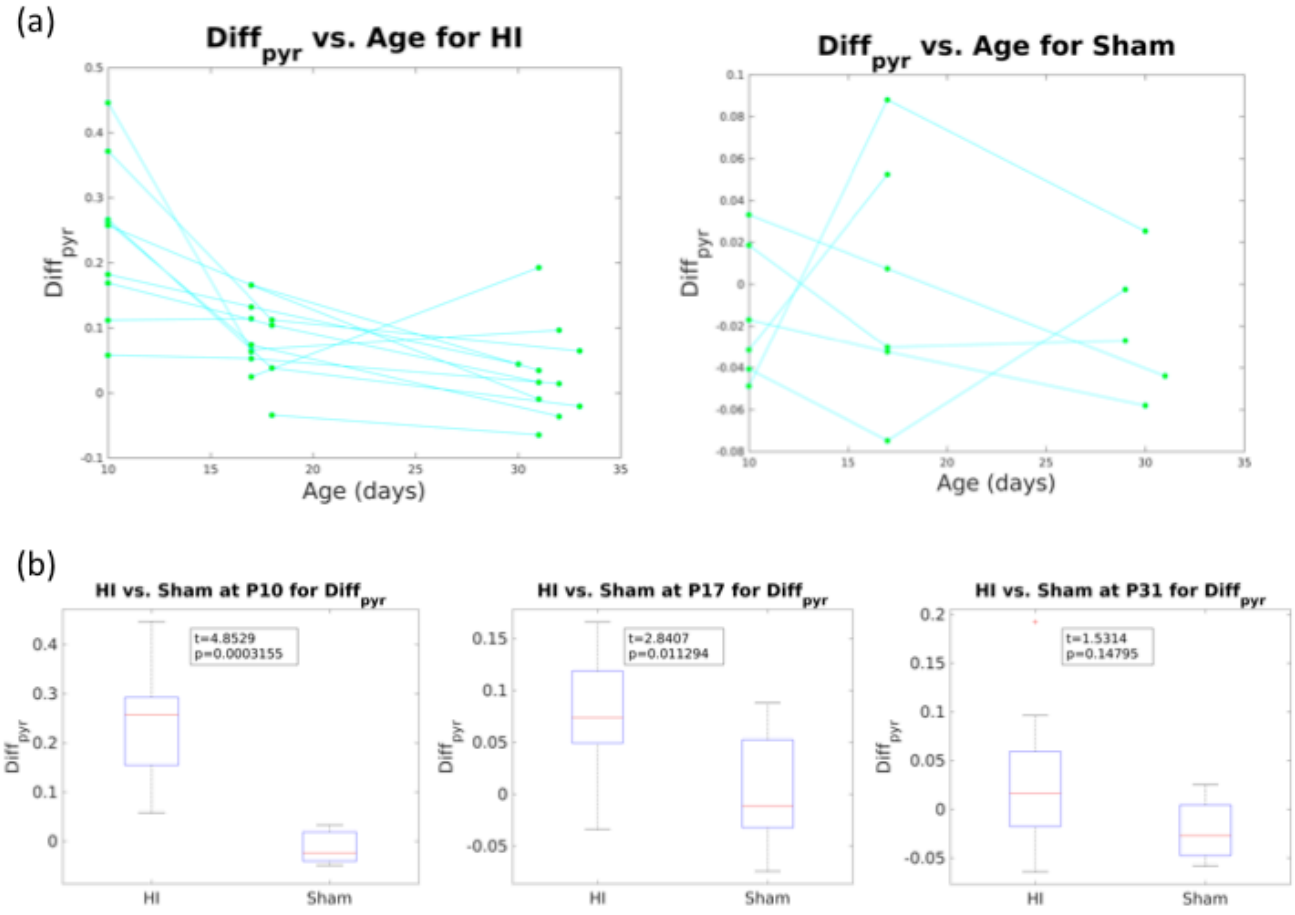

Figure 4.3: Comparison of $Diff_{pyr}$ between HI and sham at different ages.

(a) $Diff_{pyr}$ plotted again age for each subject in HI (n = 13) and sham (n = 6) groups.
(b) Student's t-test for $Diff_{pyr}$ between HI and sham groups at each age time point.

Lactate to pyruvate ratio

Although the left hemisphere has a lower pyruvate level, its lactate to pyruvate ratio is higher at P10 (Figure 4.4a) for most of the subjects, as indicated by negative $Diff_{ratio}$ values. Again, this difference between two hemispheres shrinks and diminishes as the brain matures to P17 and P31. There is no difference shown on the sham group in terms of lactate to pyruvate ratio. To further confirm our observation, Figure 4.4(b) shows the Student t-test results with $p<0.01$ at P10, $p<0.05$ at P17 and no statistical significance at P31 between HI and Sham groups.

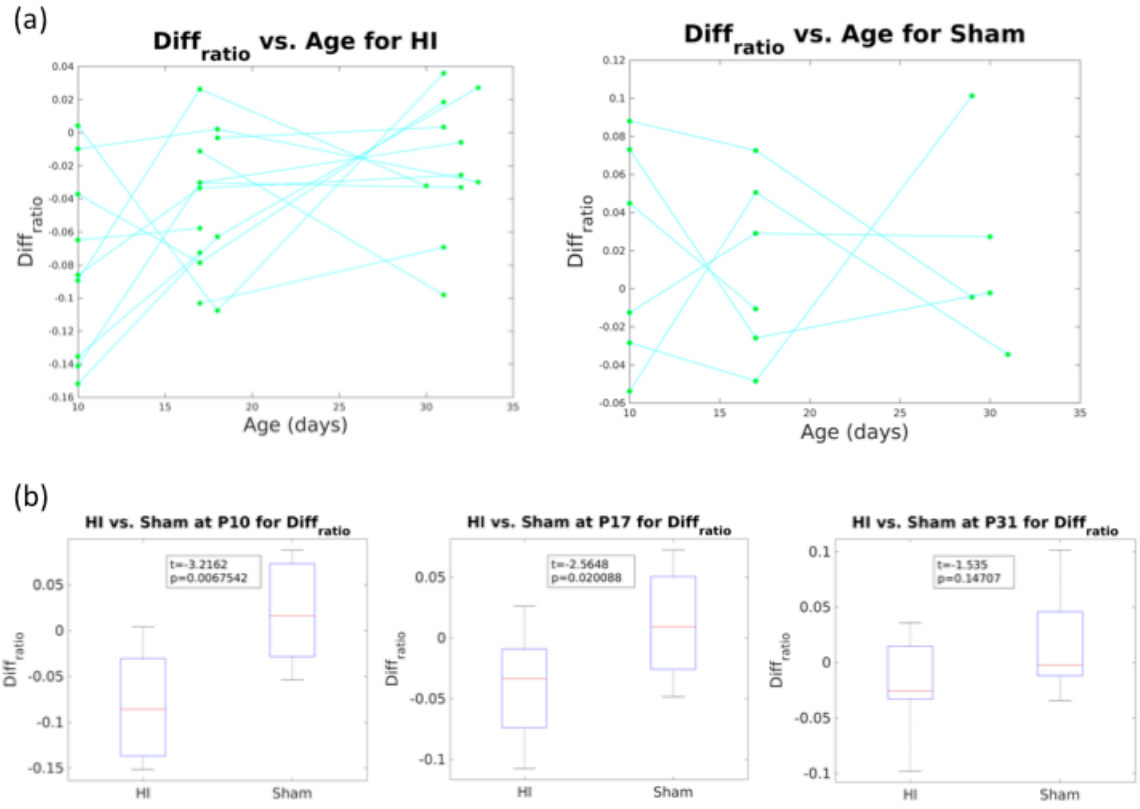

Figure 4.4: Comparison of $Diff_{ratio}$ between HI and sham at different ages.

(a) $Diff_{ratio}$ plotted again age for each subject in HI (n = 13) and sham (n = 6) groups.
(b) Student's t-test for $Diff_{ratio}$ between HI and sham groups at each age time point.

Normalized lactate level in the brain

Figure 4.5 shows the plot of normalized lactate level against age for each subject. A general pattern for sham subjects can be discerned as the normalized lactate increases from P10 to P17 and decreases from P17 to P31. However, this pattern is not consistent in the HI group. Figure 4.6 shows the same plot as Figure 4.5 but colored the HI subjects into 2 subgroups based on their HI injury level scores. The subjects with mild injury (score = 0 to 2) depict the same normalized lactate level change across age as the sham subjects, while most of the other subjects with severe injury (score = 6 to 9) do not preserve the same pattern.

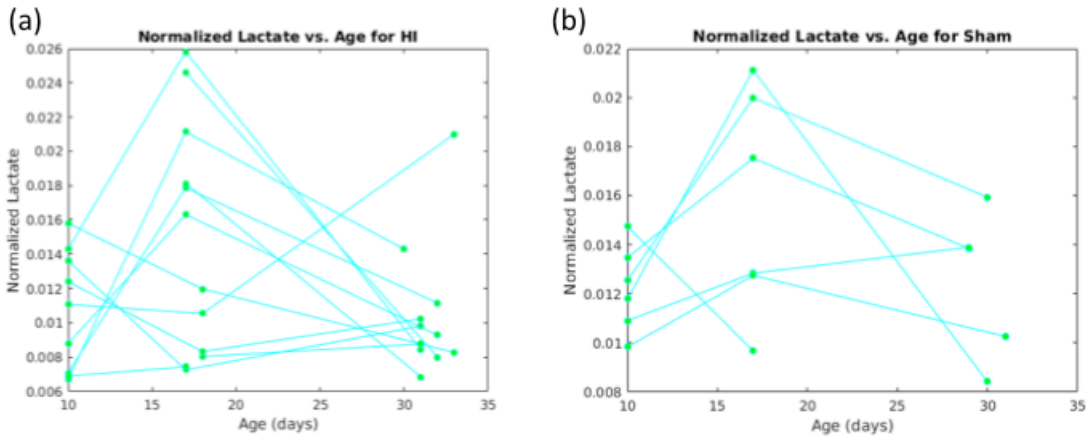

Figure 4.5: Comparison of normalized lactate level again age between HI and sham.

Normalized lactate level again age for each subject in (a) HI (n = 13) and (b) sham (n = 6) groups.

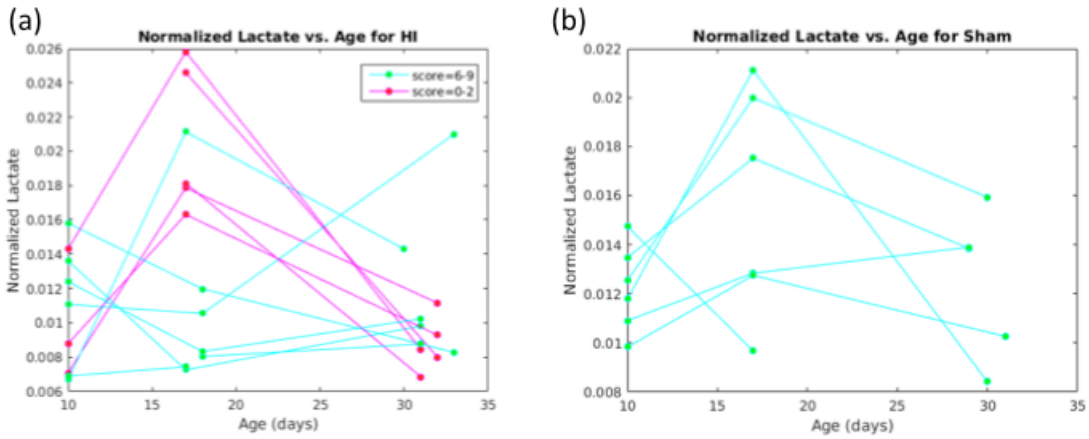

Figure 4.6: Comparison of normalized lactate level again age between HI and sham. Subjects with injury score between 0 and 2 are highlighted.

(a) Normalized lactate level again age for each subject in HI group with subgroups separated by injury scores (score=0-2: n=8; score=6-9: n=5). (b) Normalized lactate level again age for each subject in sham group.

Thus, HI subjects with mild injuries were combined with sham subjects to quantify longitudinal change of normalized lactate level. A mixed effect linear model was employed separately from P10 to P17 and from P17 to P31, and an increase in normalized lactate from P10 to P17 ($t=3.02$; $p<0.01$) and a decrease from P17 to P31 ($t=-5.16$; $p<0.01$) were observed (Figure 4.7).

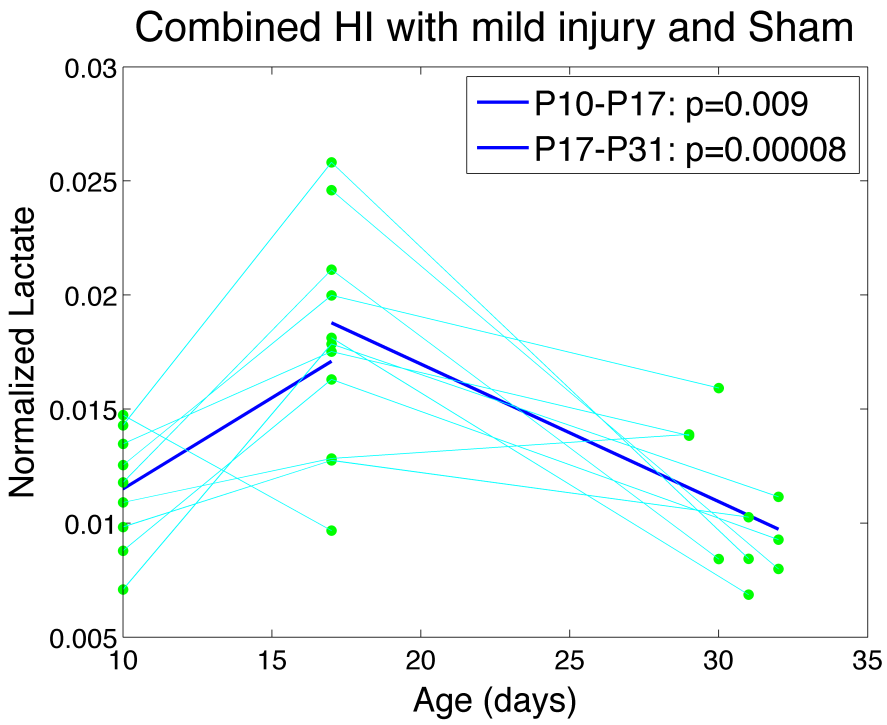

Figure 4.7: Normalized lactate level again age of sham subjects and HI subjects with mild injury.

HI subjects with mild injury (score = 0 to 2) combined with sham subjects (n = 11). A mixed-effect linear model was fitted separately from P10 to P17 and from P17 to P31.

4.4 Discussion

From the injury scores in Table 1 and T2-weighted images in Figure 1, we could only observe non-localized injury on the ipsilateral hemisphere 2 to 5 hours after HI surgery, which was depicted as hypointensity throughout the entire hemisphere. Previous MRI murine studies have shown evidence of intensity on T2-weighted images on the ipsilateral hemisphere 3 to 24 hours post HI, which was interpreted as cystic infarction in the hyperintensity area[10]. At P17 and P31, the injury becomes localized and shown as hyperintensity spreading in parts or all of the cortex, hippocampus and deep gray regions. Since the injury shown at P10 has different contrast

from that at P17 and P31, we can infer that cystic infarction has not yet developed at the area at P10, but rather inflammation. It has been documented that the inflammation by neutrophil accumulation in brain blood vessels peaks at 4 to 8 hours after reperfusion in neonatal HI rats[93], and that it can lead to further brain injury and cell death.

From both visual observation as shown in Figure 1 and statistical analysis in Figure 4.3(b) it is apparent that there is prominent reduction of pyruvate delivery to the ipsilateral hemisphere at P10. The lack of blood flow from vascular damage right after HI hinders the pyruvate delivery to the ipsilateral hemisphere. However, the lactate to pyruvate ratio is higher on the ipsilateral voxel, suggesting higher conversion to lactate as a source of energy. Oxygen supply is also deprived due to the constricted blood flow into the ipsilateral hemisphere, ultimately resulting to less availability of glucose to be oxidized for energy. Thus, aerobic glycolysis must be compensated with anaerobic for energy production. Our results support this assumption, as lactate is the end product of anaerobic glycolysis.

The difference between ipsilateral and contralateral hemisphere in pyruvate delivery and lactate to pyruvate ratio decreases during brain maturation, with smaller difference at P17. The brain usually returns to the normal aerobic metabolism about 1 h after HI. The high lactate to pyruvate ratio at P10 is derived from the aftermath of anaerobic glycolysis. Thus, at that point (~2 to 5 hours after HI), the brain could still be depending on anaerobic metabolism if the damage is too much for the restored aerobic glycolysis to function properly at the damage site. At P17, there is tissue loss due to irreversible infarction, and what remains should be functional with aerobic and

minimal anaerobic glycolysis, and therefore, less difference in lactate to pyruvate ratio between the hemispheres.

Even though the T2-weighted images show ipsilateral cystic infarction at P31, there is no statistical significance in $Diff_{pyr}$ and $Diff_{ratio}$ between HI and Sham group. This may suggest that the non-injured regions on the ipsilateral hemisphere compensate for the injured regions in blood flow and energy consumption, and result in negating any differences in pyruvate delivery and lactate to pyruvate ratio from the contralateral hemisphere.

One limitation of this work is that the voxel size was 3 x 3 x 5 mm^3 that we were only able to place one voxel on each hemisphere, which means that the ipsilateral measurement also included normative brain tissue. Low spatial resolution has been a technical challenge in hyperpolarized ^{13}C studies, especially dynamic measurements with short acquisition time (4 second TR). Moreover, T1 of hyperpolarized substrate is shorter at the higher field strength of our 14T animal scanner as compared to lower fields such as 1.5T or 3T. Therefore, there is a tradeoff between spatial resolution and temporal resolution. With future advancements in acquisition techniques, higher spatial resolution may be achievable. With smaller voxels, we will become able to distinguish localized injury from its surrounding non-injured area and make more comprehensive interpretation on ^{13}C substrates uptake and conversion.

Our previous chapter of utilizing hyperpolarized ^{13}C on normal brain maturation starting from P18 [92]. In this chapter, we had one more time point, P10, so it covers the maturation stages from newborn to adolescence and to adult in human equivalence. Although the HI group does

not show the same general trend of lactate production as the sham group in Figure 4.5, when the HI mice were divided into two distinct subgroups based on the injury score as shown in Figure 6(a), it became clear that the HI subgroup with mild injury (score = 0 to 2) exhibits the same trend as the sham group. When these two groups are combined as shown in Figure 4.7, there is a statistically significant decrease from P17 to P31 in this group. This is consistent with our previous findings of a decreasing pyruvate to lactate conversion starting at P18. Furthermore, Figure 4.7 shows a statistically significant increase in lactate production from P10 to P17, which might suggest increased utilization of lactate as a source of energy. A previous *in situ* study has shown that the expression of the monocarboxylate transporter (MCT1 and MCT2) mRNAs, upon which lactate delivery and utilization in the brain depends, starts increasing from P0, peaks at P15, decreases at P30 and stabilizes after that[71]. Both this finding and our work agree on the lactate utilization in normal brain maturation, which increases from neonatal to adolescence and drops after weaning. The HI subgroup with high injury scores (6 to 9) does not show a general increase of lactate production from P10 to P17 or a general decrease of lactate production from P17 to P31, which may due to serious interruptions on the metabolic pathway by the HI injury.

Future Directions

Overall, this dissertation has discussed a few unexplored but important areas of MRI methodology and applications in pediatric brain development. First, while DTI has been extensively utilized in pediatric MRI studies, motion artifacts remain a common problem and the resulting effects of rejecting diffusion parameters remains rarely investigated. Few previous works on comparing various diffusion encoding schemes were based on simulated data or phantom scans. Our work evaluated uncertainty and bias of rejecting diffusion parameters based on simulations on complete clinical data. This provides an insight to researchers on making decisions and interpreting the results in their future DTI studies involving unsedated pediatric patients. With severe motion artifact and inevitable diffusion volume rejection, it is worthwhile noting the distribution of the rejected directions, to account for any bias generated in the final results.

Hyperpolarized ^{13}C MRI is an innovative and fast growing field with most of its applications in cancer metabolism research. We first applied this technique to early brain development in both normal and hypoxic ischemia model, where research was based on conventional T1-, T2-weighted, DTI and proton spectroscopy for over a decade. Our work introduces a new perspective of investigating metabolic related injuries or diseases during brain development, with the ability to quantify *in vivo* real-time metabolic conversion in a short time. The part of work on normal brain development will serve as a baseline for longitudinal studies of injury or disease models. The other part of work on hypoxic ischemia provides the feasibility of injury detection at a very early stage due to its short scan time to reveal dynamic metabolic exchange. It is also able to track injury progression of metabolic changes during brain development in a longer term. This

work can be continued to explore the response of metabolic changes after hypothermia treatment for hypoxic ischemia. It can potentially be an effective marker to recognize the responders and non-responders immediately after the treatment, which provides valuable information for clinicians to quickly pursue other types of treatment for the non-responders in order to achieve better chance of survival or outcome.

References

1. McRobbie DW, Moore EA, Graves MJ, Prince MR. MRI from Picture to Proton: Cambridge university press; 2017.
2. Oishi K, Faria AV, Mori S. Advanced neonatal neuroMRI. Magnetic Resonance Imaging Clinics. 2012;20(1):81-91.
3. Stejskal EO, Tanner JE. Spin diffusion measurements: spin echoes in the presence of a time-dependent field gradient. The journal of chemical physics. 1965;42(1):288-92.
4. Mugler JP. Improved three-dimensional GRASE imaging with the SORT phase-encoding strategy. Journal of Magnetic Resonance Imaging. 1999;9(4):604-12.
5. Calabrese E, Badea A, Watson C, Johnson GA. A quantitative magnetic resonance histology atlas of postnatal rat brain development with regional estimates of growth and variability. Neuroimage. 2013;71:196-206.
6. Chuang N, Mori S, Yamamoto A, Jiang H, Ye X, Xu X, et al. An MRI-based atlas and database of the developing mouse brain. Neuroimage. 2011;54(1):80-9.
7. Szulc KU, Lerch JP, Nieman BJ, Bartelle BB, Friedel M, Suero-Abreu GA, et al. 4D MEMRI atlas of neonatal FVB/N mouse brain development. Neuroimage. 2015;118:49-62.
8. Albensi BC, Schweizer MP, Rarick TM, Filloux F. Magnetic resonance imaging of hypoxic-ischemic brain injury in the neonatal rat. Investigative radiology. 1998;33(7):377-85.

9. Wang Y, Cheung P-T, Shen G, Wu E, Cao G, Bart I, et al. Hypoxic-ischemic brain injury in the neonatal rat model: relationship between lesion size at early MR imaging and irreversible infarction. American journal of neuroradiology. 2006;27(1):51-4.

10. Aden U, Dahlberg V, Fredholm BB, Lai LJ, Chen Z, Bjelke B. MRI evaluation and functional assessment of brain injury after hypoxic ischemia in neonatal mice. Stroke. 2002;33(5):1405-10. Epub 2002/05/04. PubMed PMID: 11988622.

11. Tuor UI, Kozlowski P, Del Bigio MR, Ramjiawan B, Su S, Malisza K, et al. Diffusion- and T2-weighted increases in magnetic resonance images of immature brain during hypoxia-ischemia: transient reversal posthypoxia. Experimental neurology. 1998;150(2):321-8. Epub 1998/05/30. doi: 10.1006/exnr.1997.6766. PubMed PMID: 9527902.

12. Qiao M, Meng S, Scobie K, Foniok T, Tuor UI. Magnetic resonance imaging of differential gray versus white matter injury following a mild or moderate hypoxic-ischemic insult in neonatal rats. Neuroscience letters. 2004;368(3):332-6.

13. Aggarwal M, Burnsed J, Martin LJ, Northington FJ, Zhang J. Imaging neurodegeneration in the mouse hippocampus after neonatal hypoxia–ischemia using oscillating gradient diffusion MRI. Magnetic resonance in medicine. 2014;72(3):829-40.

14. Tkac I, Henry PG, Andersen P, Keene CD, Low WC, Gruetter R. Highly resolved in vivo 1H NMR spectroscopy of the mouse brain at 9.4 T. Magnetic resonance in medicine : official journal of the Society of Magnetic Resonance in Medicine / Society of Magnetic Resonance in Medicine. 2004;52(3):478-84. Epub 2004/08/31. doi: 10.1002/mrm.20184. PubMed PMID: 15334565.

15. Larvaron P, Bielicki G, Boespflug-Tanguy O, Renou JP. Proton MRS of early post-natal mouse brain modifications in vivo. NMR in biomedicine. 2006;19(2):180-7. Epub 2006/02/14. doi: 10.1002/nbm.997. PubMed PMID: 16470692.

16. Bluml S, Wisnowski JL, Nelson MD, Jr., Paquette L, Gilles FH, Kinney HC, et al. Metabolic maturation of the human brain from birth through adolescence: insights from in vivo magnetic resonance spectroscopy. Cerebral cortex (New York, NY : 1991). 2013;23(12):2944-55. Epub 2012/09/07. doi: 10.1093/cercor/bhs283. PubMed PMID: 22952278; PubMed Central PMCID: PMCPMC3888212.

17. Kauppinen RA, Williams SR. Nuclear magnetic resonance spectroscopy studies of the brain. Prog Neurobiol. 1994;44(1):87-118. Epub 1994/09/01. PubMed PMID: 7831473.

18. Pfeuffer J, Tkac I, Provencher SW, Gruetter R. Toward an in vivo neurochemical profile: quantification of 18 metabolites in short-echo-time (1)H NMR spectra of the rat brain. Journal of magnetic resonance (San Diego, Calif : 1997). 1999;141(1):104-20. Epub 1999/10/21. doi: 10.1006/jmre.1999.1895. PubMed PMID: 10527748.

19. Kloiber O, Miyazawa T, Hoehn-Berlage M, Hossmann KA. Simultaneous 31P NMR spectroscopy and laser Doppler flowmetry of rat brain during global ischemia and reperfusion. NMR Biomed. 1993;6(2):144-52. Epub 1993/03/01. PubMed PMID: 8499245.

20. Morken TS, Brekke E, Håberg A, Widerøe M, Brubakk A-M, Sonnewald U. Neuron–astrocyte interactions, pyruvate carboxylation and the pentose phosphate pathway in the neonatal rat brain. Neurochemical research. 2014;39(3):556-69.

21. Chowdhury GM, Patel AB, Mason GF, Rothman DL, Behar KL. Glutamatergic and GABAergic neurotransmitter cycling and energy metabolism in rat cerebral cortex during

postnatal development. Journal of Cerebral Blood Flow & Metabolism. 2007;27(12):1895-907.

22. Novotny EJ, Ariyan C, Mason GF, O'Reilly J, Haddad GG, Behar KL. Differential increase in cerebral cortical glucose oxidative metabolism during rat postnatal development is greater in vivo than in vitro. Brain research. 2001;888(2):193-202.

23. Hassel B, Brathe A. Cerebral metabolism of lactate in vivo: evidence for neuronal pyruvate carboxylation. Journal of cerebral blood flow and metabolism : official journal of the International Society of Cerebral Blood Flow and Metabolism. 2000;20(2):327-36. Epub 2000/03/04. doi: 10.1097/00004647-200002000-00014. PubMed PMID: 10698070.

24. Waagepetersen HS, Bakken IJ, Larsson OM, Sonnewald U, Schousboe A. Comparison of lactate and glucose metabolism in cultured neocortical neurons and astrocytes using 13C-NMR spectroscopy. Developmental neuroscience. 1998;20(4-5):310-20. Epub 1998/10/21. PubMed PMID: 9778567.

25. Alves PM, McKenna MC, Sonnewald U. Lactate metabolism in mouse brain astrocytes studied by [13C]NMR spectroscopy. Neuroreport. 1995;6(16):2201-4. Epub 1995/11/13. PubMed PMID: 8595202.

26. Bouzier-Sore AK, Voisin P, Canioni P, Magistretti PJ, Pellerin L. Lactate is a preferential oxidative energy substrate over glucose for neurons in culture. Journal of cerebral blood flow and metabolism : official journal of the International Society of Cerebral Blood Flow and Metabolism. 2003;23(11):1298-306. Epub 2003/11/06. doi: 10.1097/01.wcb.0000091761.61714.25. PubMed PMID: 14600437.

27. Cerdan S, Künnecke B, Seelig J. Cerebral metabolism of [1, 2-13C2] acetate as detected by in vivo and in vitro 13C NMR. Journal of Biological Chemistry. 1990;265(22):12916-26.

28. Sibson N, Dhankhar A, Mason G, Behar K, Rothman D, Shulman R. In vivo 13C NMR measurements of cerebral glutamine synthesis as evidence for glutamate–glutamine cycling. Proceedings of the National Academy of Sciences. 1997;94(6):2699-704.

29. Ardenkjær-Larsen JH, Fridlund B, Gram A, Hansson G, Hansson L, Lerche MH, et al. Increase in signal-to-noise ratio of> 10,000 times in liquid-state NMR. Proceedings of the National Academy of Sciences. 2003;100(18):10158-63.

30. Ardenkjaer-Larsen JH, Fridlund B, Gram A, Hansson G, Hansson L, Lerche MH, et al. Increase in signal-to-noise ratio of > 10,000 times in liquid-state NMR. Proceedings of the National Academy of Sciences of the United States of America. 2003;100(18):10158-63. Epub 2003/08/22. doi: 10.1073/pnas.1733835100. PubMed PMID: 12930897; PubMed Central PMCID: PMCPMC193532.

31. Golman K, Ardenkjaer-Larsen JH, Petersson JS, Mansson S, Leunbach I. Molecular imaging with endogenous substances. Proceedings of the National Academy of Sciences of the United States of America. 2003;100(18):10435-9. Epub 2003/08/22. doi: 10.1073/pnas.1733836100. PubMed PMID: 12930896; PubMed Central PMCID: PMCPMC193579.

32. Golman K, Thaning M. Real-time metabolic imaging. Proceedings of the National Academy of Sciences. 2006;103(30):11270-5.

33. Park I, Bok R, Ozawa T, Phillips JJ, James CD, Vigneron DB, et al. Detection of early response to temozolomide treatment in brain tumors using hyperpolarized 13C MR

metabolic imaging. Journal of magnetic resonance imaging : JMRI. 2011;33(6):1284-90. Epub 2011/05/19. doi: 10.1002/jmri.22563. PubMed PMID: 21590996.

34. Park I, Larson PEZ, Gordon JW, Carvajal L, Chen HY, Bok R, et al. Development of methods and feasibility of using hyperpolarized carbon-13 imaging data for evaluating brain metabolism in patient studies. Magnetic resonance in medicine. 2018;80(3):864-73. Epub 2018/01/13. doi: 10.1002/mrm.27077. PubMed PMID: 29322616; PubMed Central PMCID: PMCPMC5980662.

35. Nelson SJ, Kurhanewicz J, Vigneron DB, Larson PE, Harzstark AL, Ferrone M, et al. Metabolic imaging of patients with prostate cancer using hyperpolarized [1-(1)(3)C]pyruvate. Science translational medicine. 2013;5(198):198ra08. Epub 2013/08/16. doi: 10.1126/scitranslmed.3006070. PubMed PMID: 23946197; PubMed Central PMCID: PMCPMC4201045.

36. Kraus MF, Susmaras T, Caughlin BP, Walker CJ, Sweeney JA, Little DM. White matter integrity and cognition in chronic traumatic brain injury: a diffusion tensor imaging study. Brain : a journal of neurology. 2007;130(Pt 10):2508-19. Epub 2007/09/18. doi: 10.1093/brain/awm216. PubMed PMID: 17872928.

37. Lipton ML, Gellella E, Lo C, Gold T, Ardekani BA, Shifteh K, et al. Multifocal white matter ultrastructural abnormalities in mild traumatic brain injury with cognitive disability: a voxel-wise analysis of diffusion tensor imaging. Journal of neurotrauma. 2008;25(11):1335-42. Epub 2008/12/09. doi: 10.1089/neu.2008.0547. PubMed PMID: 19061376.

38. Lu S, Ahn D, Johnson G, Cha S. Peritumoral diffusion tensor imaging of high-grade gliomas and metastatic brain tumors. AJNR American journal of neuroradiology. 2003;24(5):937-41. Epub 2003/05/16. PubMed PMID: 12748097.

39. Counsell SJ, Allsop JM, Harrison MC, Larkman DJ, Kennea NL, Kapellou O, et al. Diffusion-weighted imaging of the brain in preterm infants with focal and diffuse white matter abnormality. Pediatrics. 2003;112(1 Pt 1):1-7. Epub 2003/07/03. PubMed PMID: 12837859.

40. Rose SE, Chen F, Chalk JB, Zelaya FO, Strugnell WE, Benson M, et al. Loss of connectivity in Alzheimer's disease: an evaluation of white matter tract integrity with colour coded MR diffusion tensor imaging. Journal of neurology, neurosurgery, and psychiatry. 2000;69(4):528-30. Epub 2000/09/16. PubMed PMID: 10990518; PubMed Central PMCID: PMCPMC1737121.

41. Basser PJ, Pajevic S, Pierpaoli C, Duda J, Aldroubi A. In vivo fiber tractography using DT-MRI data. Magnetic resonance in medicine : official journal of the Society of Magnetic Resonance in Medicine / Society of Magnetic Resonance in Medicine. 2000;44(4):625-32. Epub 2000/10/12. PubMed PMID: 11025519.

42. Mori S, van Zijl PC. Fiber tracking: principles and strategies - a technical review. NMR in biomedicine. 2002;15(7-8):468-80. Epub 2002/12/19. doi: 10.1002/nbm.781. PubMed PMID: 12489096.

43. Jones DK, Horsfield MA, Simmons A. Optimal strategies for measuring diffusion in anisotropic systems by magnetic resonance imaging. Magnetic resonance in medicine : official journal of the Society of Magnetic Resonance in Medicine / Society of Magnetic

Resonance in Medicine. 1999;42(3):515-25. Epub 1999/09/01. PubMed PMID: 10467296.

44. Skare S, Hedehus M, Moseley ME, Li TQ. Condition number as a measure of noise performance of diffusion tensor data acquisition schemes with MRI. Journal of magnetic resonance (San Diego, Calif : 1997). 2000;147(2):340-52. Epub 2000/12/01. doi: 10.1006/jmre.2000.2209. PubMed PMID: 11097823.

45. Papadakis NG, Murrills CD, Hall LD, Huang CL, Adrian Carpenter T. Minimal gradient encoding for robust estimation of diffusion anisotropy. Magnetic resonance imaging. 2000;18(6):671-9. Epub 2000/08/10. PubMed PMID: 10930776.

46. Hasan KM, Parker DL, Alexander AL. Comparison of gradient encoding schemes for diffusion-tensor MRI. Journal of magnetic resonance imaging : JMRI. 2001;13(5):769-80. Epub 2001/05/01. PubMed PMID: 11329200.

47. Batchelor PG, Atkinson D, Hill DL, Calamante F, Connelly A. Anisotropic noise propagation in diffusion tensor MRI sampling schemes. Magnetic resonance in medicine : official journal of the Society of Magnetic Resonance in Medicine / Society of Magnetic Resonance in Medicine. 2003;49(6):1143-51. Epub 2003/05/28. doi: 10.1002/mrm.10491. PubMed PMID: 12768593.

48. Ordidge RJ, Helpern JA, Qing ZX, Knight RA, Nagesh V. Correction of motional artifacts in diffusion-weighted MR images using navigator echoes. Magnetic resonance imaging. 1994;12(3):455-60. Epub 1994/01/01. PubMed PMID: 8007775.

49. Skare S, Andersson JL. On the effects of gating in diffusion imaging of the brain using single shot EPI. Magnetic resonance imaging. 2001;19(8):1125-8. Epub 2001/11/17. PubMed PMID: 11711237.

50. Dietrich O, Heiland S, Benner T, Sartor K. Reducing motion artefacts in diffusion-weighted MRI of the brain: efficacy of navigator echo correction and pulse triggering. Neuroradiology. 2000;42(2):85-91. Epub 2000/02/09. PubMed PMID: 10663480.

51. Jiang S, Xue H, Counsell S, Anjari M, Allsop J, Rutherford M, et al. Diffusion tensor imaging (DTI) of the brain in moving subjects: application to in-utero fetal and ex-utero studies. Magnetic resonance in medicine : official journal of the Society of Magnetic Resonance in Medicine / Society of Magnetic Resonance in Medicine. 2009;62(3):645-55. Epub 2009/06/16. doi: 10.1002/mrm.22032. PubMed PMID: 19526505.

52. Tymofiyeva O, Hess CP, Ziv E, Lee PN, Glass HC, Ferriero DM, et al. A DTI-based template-free cortical connectome study of brain maturation. PloS one. 2013;8(5):e63310. Epub 2013/05/16. doi: 10.1371/journal.pone.0063310. PubMed PMID: 23675475; PubMed Central PMCID: PMCPMC3652871.

53. Chang LC, Jones DK, Pierpaoli C. RESTORE: robust estimation of tensors by outlier rejection. Magnetic resonance in medicine : official journal of the Society of Magnetic Resonance in Medicine / Society of Magnetic Resonance in Medicine. 2005;53(5):1088-95. Epub 2005/04/22. doi: 10.1002/mrm.20426. PubMed PMID: 15844157.

54. Smith SM, Jenkinson M, Woolrich MW, Beckmann CF, Behrens TE, Johansen-Berg H, et al. Advances in functional and structural MR image analysis and implementation as FSL. NeuroImage. 2004;23 Suppl 1:S208-19. Epub 2004/10/27. doi: 10.1016/j.neuroimage.2004.07.051. PubMed PMID: 15501092.

55. Smith SM. Fast robust automated brain extraction. Human brain mapping. 2002;17(3):143-55. Epub 2002/10/23. doi: 10.1002/hbm.10062. PubMed PMID: 12391568.

56. Jones DK. Determining and visualizing uncertainty in estimates of fiber orientation from diffusion tensor MRI. Magnetic resonance in medicine : official journal of the Society of Magnetic Resonance in Medicine / Society of Magnetic Resonance in Medicine. 2003;49(1):7-12. doi: 10.1002/mrm.10331. PubMed PMID: 12509814.

57. Landman BA, Farrell JA, Jones CK, Smith SA, Prince JL, Mori S. Effects of diffusion weighting schemes on the reproducibility of DTI-derived fractional anisotropy, mean diffusivity, and principal eigenvector measurements at 1.5T. NeuroImage. 2007;36(4):1123-38. Epub 2007/05/29. doi: 10.1016/j.neuroimage.2007.02.056. PubMed PMID: 17532649.

58. Basser PJ, Mattiello J, LeBihan D. MR diffusion tensor spectroscopy and imaging. Biophysical journal. 1994;66(1):259-67. Epub 1994/01/01. doi: 10.1016/s0006-3495(94)80775-1. PubMed PMID: 8130344; PubMed Central PMCID: PMCPMC1275686.

59. Hasan KM, Narayana PA. Computation of the fractional anisotropy and mean diffusivity maps without tensor decoding and diagonalization: Theoretical analysis and validation. Magnetic resonance in medicine : official journal of the Society of Magnetic Resonance in Medicine / Society of Magnetic Resonance in Medicine. 2003;50(3):589-98. Epub 2003/08/27. doi: 10.1002/mrm.10552. PubMed PMID: 12939767.

60. Hasan KM. A framework for quality control and parameter optimization in diffusion tensor imaging: theoretical analysis and validation. Magnetic resonance imaging. 2007;25(8):1196-202. Epub 2007/04/20. doi: 10.1016/j.mri.2007.02.011. PubMed PMID: 17442523; PubMed Central PMCID: PMCPMC2185542.

61. Tuch DS. Q-ball imaging. Magnetic resonance in medicine : official journal of the Society of Magnetic Resonance in Medicine / Society of Magnetic Resonance in Medicine. 2004;52(6):1358-72. Epub 2004/11/25. doi: 10.1002/mrm.20279. PubMed PMID: 15562495.

62. Tournier JD, Calamante F, Gadian DG, Connelly A. Direct estimation of the fiber orientation density function from diffusion-weighted MRI data using spherical deconvolution. NeuroImage. 2004;23(3):1176-85. Epub 2004/11/06. doi: 10.1016/j.neuroimage.2004.07.037. PubMed PMID: 15528117.

63. Liu C, Bammer R, Acar B, Moseley ME. Characterizing non-Gaussian diffusion by using generalized diffusion tensors. Magnetic resonance in medicine : official journal of the Society of Magnetic Resonance in Medicine / Society of Magnetic Resonance in Medicine. 2004;51(5):924-37. Epub 2004/05/04. doi: 10.1002/mrm.20071. PubMed PMID: 15122674.

64. Wedeen VJ, Hagmann P, Tseng WY, Reese TG, Weisskoff RM. Mapping complex tissue architecture with diffusion spectrum magnetic resonance imaging. Magnetic resonance in medicine : official journal of the Society of Magnetic Resonance in Medicine / Society of Magnetic Resonance in Medicine. 2005;54(6):1377-86. Epub 2005/10/26. doi: 10.1002/mrm.20642. PubMed PMID: 16247738.

65. Frank LR. Characterization of anisotropy in high angular resolution diffusion-weighted MRI. Magnetic resonance in medicine : official journal of the Society of Magnetic Resonance in Medicine / Society of Magnetic Resonance in Medicine. 2002;47(6):1083-99. Epub 2002/07/12. doi: 10.1002/mrm.10156. PubMed PMID: 12111955.

66. Tuch DS, Wisco JJ, Khachaturian MH, Ekstrom LB, Kotter R, Vanduffel W. Q-ball imaging of macaque white matter architecture. Philosophical transactions of the Royal Society of London Series B, Biological sciences. 2005;360(1457):869-79. Epub 2005/08/10. doi: 10.1098/rstb.2005.1651. PubMed PMID: 16087432; PubMed Central PMCID: PMCPMC1854934.

67. Hess CP, Mukherjee P, Han ET, Xu D, Vigneron DB. Q-ball reconstruction of multimodal fiber orientations using the spherical harmonic basis. Magnetic resonance in medicine : official journal of the Society of Magnetic Resonance in Medicine / Society of Magnetic Resonance in Medicine. 2006;56(1):104-17. Epub 2006/06/07. doi: 10.1002/mrm.20931. PubMed PMID: 16755539.

68. Dienel GA, Cruz NF. Imaging brain activation: simple pictures of complex biology. Annals of the New York Academy of Sciences. 2008;1147:139-70. Epub 2008/12/17. doi: 10.1196/annals.1427.011. PubMed PMID: 19076439; PubMed Central PMCID: PMCPMC2693893.

69. Zierhut ML, Yen YF, Chen AP, Bok R, Albers MJ, Zhang V, et al. Kinetic modeling of hyperpolarized 13C1-pyruvate metabolism in normal rats and TRAMP mice. Journal of magnetic resonance (San Diego, Calif : 1997). 2010;202(1):85-92. Epub 2009/11/04. doi: 10.1016/j.jmr.2009.10.003. PubMed PMID: 19884027; PubMed Central PMCID: PMCPMC2833325.

70. Worsley KJ, Taylor, J. E., Carbonell, F., Chung, M. K, Duerden, E., Bernhardt, B., Lyttelton, O., Boucher, M., Evans, A. C. SurfStat: A Matlab toolbox for the statistical analysis of univariate and multivariate surface and volumetric data using linear mixed effects models and random field theory. NeuroImage. 2009;47:S102.

71. Pellerin L, Pellegri G, Martin JL, Magistretti PJ. Expression of monocarboxylate transporter mRNAs in mouse brain: support for a distinct role of lactate as an energy substrate for the neonatal vs. adult brain. Proceedings of the National Academy of Sciences of the United States of America. 1998;95(7):3990-5. Epub 1998/05/09. PubMed PMID: 9520480; PubMed Central PMCID: PMCPMC19950.

72. Gladden LB. Lactate metabolism: a new paradigm for the third millennium. The Journal of physiology. 2004;558(Pt 1):5-30. Epub 2004/05/08. doi: 10.1113/jphysiol.2003.058701. PubMed PMID: 15131240; PubMed Central PMCID: PMCPMC1664920.

73. Medina JM, Tabernero A. Lactate utilization by brain cells and its role in CNS development. Journal of neuroscience research. 2005;79(1-2):2-10. Epub 2004/12/02. doi: 10.1002/jnr.20336. PubMed PMID: 15573408.

74. Dienel GA. Brain lactate metabolism: the discoveries and the controversies. Journal of cerebral blood flow and metabolism : official journal of the International Society of Cerebral Blood Flow and Metabolism. 2012;32(7):1107-38. Epub 2011/12/22. doi: 10.1038/jcbfm.2011.175. PubMed PMID: 22186669; PubMed Central PMCID: PMCPMC3390802.

75. Brooks GA. Mammalian fuel utilization during sustained exercise. Comparative biochemistry and physiology Part B, Biochemistry & molecular biology. 1998;120(1):89-107. Epub 1998/10/27. PubMed PMID: 9787780.

76. Medina J, Fernández E, Bolaños J, Vicario C, Arizmendi C. Fuel Supply to the Brain During the Early Postnatal Period. In: Cuezva J, Pascual-Leone A, Patel M, editors.

Endocrine and Biochemical Development of the Fetus and Neonate. Reproductive Biology: Springer US; 1990. p. 175-94.

77. Dringen R, Gebhardt R, Hamprecht B. Glycogen in astrocytes: possible function as lactate supply for neighboring cells. Brain research. 1993;623(2):208-14. Epub 1993/10/01. PubMed PMID: 8221102.

78. Vicario C, Arizmendi C, Malloch G, Clark JB, Medina JM. Lactate utilization by isolated cells from early neonatal rat brain. Journal of neurochemistry. 1991;57(5):1700-7. Epub 1991/11/01. PubMed PMID: 1919582.

79. Arizmendi C, Medina JM. Lactate as an oxidizable substrate for rat brain in vitro during the perinatal period. The Biochemical journal. 1983;214(2):633-5. Epub 1983/08/15. PubMed PMID: 6615484; PubMed Central PMCID: PMCPMC1152290.

80. Vicario C, Tabernero A, Medina JM. Regulation of lactate metabolism by albumin in rat neurons and astrocytes from primary culture. Pediatric research. 1993;34(6):709-15. Epub 1993/12/01. doi: 10.1203/00006450-199312000-00002. PubMed PMID: 8108180.

81. Sanchez-Abarca LI, Tabernero A, Medina JM. Oligodendrocytes use lactate as a source of energy and as a precursor of lipids. Glia. 2001;36(3):321-9. Epub 2001/12/18. PubMed PMID: 11746769.

82. Chuang N, Mori S, Yamamoto A, Jiang H, Ye X, Xu X, et al. An MRI-based atlas and database of the developing mouse brain. Neuroimage. 2011;54(1):80-9. Epub 2010/07/27. doi: 10.1016/j.neuroimage.2010.07.043. PubMed PMID: 20656042; PubMed Central PMCID: PMCPMC2962762.

83. Horrocks LA. Composition of mouse brain myelin during development. Journal of neurochemistry. 1968;15(6):483-8. Epub 1968/06/01. PubMed PMID: 5668048.

84. Morell P, Greenfield S, Costantino-Ceccarini E, Wisniewski H. Changes in the protein composition of mouse brain myelin during development. Journal of neurochemistry. 1972;19(11):2545-54. Epub 1972/11/01. PubMed PMID: 5086242.

85. Semple BD, Blomgren K, Gimlin K, Ferriero DM, Noble-Haeusslein LJ. Brain development in rodents and humans: identifying benchmarks of maturation and vulnerability to injury across species. Progress in neurobiology. 2013;106:1-16.

86. Vannucci RC, Vannucci SJ. Glucose metabolism in the developing brain. Seminars in perinatology. 2000;24(2):107-15. Epub 2000/05/11. PubMed PMID: 10805166.

87. Chen AP, Kurhanewicz J, Bok R, Xu D, Joun D, Zhang V, et al. Feasibility of using hyperpolarized [1-13C]lactate as a substrate for in vivo metabolic 13C MRSI studies. Magnetic resonance imaging. 2008;26(6):721-6. Epub 2008/05/16. doi: 10.1016/j.mri.2008.01.002. PubMed PMID: 18479878; PubMed Central PMCID: PMCPMC2577896.

88. Larson PE, Kerr AB, Swisher CL, Pauly JM, Vigneron DB. A rapid method for direct detection of metabolic conversion and magnetization exchange with application to hyperpolarized substrates. Journal of magnetic resonance (San Diego, Calif : 1997). 2012;225:71-80. Epub 2012/11/13. doi: 10.1016/j.jmr.2012.09.014. PubMed PMID: 23143011; PubMed Central PMCID: PMCPMC3531583.

89. Swisher CL, Larson PE, Kruttwig K, Kerr AB, Hu S, Bok RA, et al. Quantitative measurement of cancer metabolism using stimulated echo hyperpolarized carbon-13 MRS. Magnetic resonance in medicine. 2014;71(1):1-11. Epub 2013/02/16. doi: 10.1002/mrm.24634. PubMed PMID: 23412881; PubMed Central PMCID: PMCPMC3659200.

90. Burnsed JC, Chavez-Valdez R, Hossain MS, Kesavan K, Martin LJ, Zhang J, et al. Hypoxia-ischemia and therapeutic hypothermia in the neonatal mouse brain--a longitudinal study. PloS one. 2015;10(3):e0118889. Epub 2015/03/17. doi: 10.1371/journal.pone.0118889. PubMed PMID: 25774892; PubMed Central PMCID: PMCPMC4361713.

91. Rice JE, Vannucci RC, Brierley JB. The influence of immaturity on hypoxic-ischemic brain damage in the rat. Annals of neurology. 1981;9(2):131-41.

92. Chen Y, Kim H, Bok R, Sukumar S, Mu X, Sheldon RA, et al. Pyruvate to Lactate Metabolic Changes during Neurodevelopment Measured Dynamically Using Hyperpolarized 13C Imaging in Juvenile Murine Brain. Developmental neuroscience. 2016;38(1):34-40. Epub 2015/11/10. doi: 10.1159/000439271. PubMed PMID: 26550989; PubMed Central PMCID: PMCPMC4732911.

93. Hudome S, Palmer C, Roberts RL, Mauger D, Housman C, Towfighi J. The role of neutrophils in the production of hypoxic-ischemic brain injury in the neonatal rat. Pediatric research. 1997;41(5):607-16. Epub 1997/05/01. doi: 10.1203/00006450-199705000-00002. PubMed PMID: 9128280.

Publishing Agreement

It is the policy of the University to encourage the distribution of all theses, dissertations, and manuscripts. Copies of all UCSF theses, dissertations, and manuscripts will be routed to the library via the Graduate Division. The library will make all theses, dissertations, and manuscripts accessible to the public and will preserve these to the best of their abilities, in perpetuity.

Please sign the following statement:

I hereby grant permission to the Graduate Division of the University of California, San Francisco to release copies of my thesis, dissertation, or manuscript to the Campus Library to provide access and preservation, in whole or in part, in perpetuity.

Author Signature

12/19/2018

Date